# Installation and operation of a high-temperature surface ion source for the online coupling of TRIGA-SPEC to the TRIGA Mainz research reactor and high-precision mass measurements of transuranium nuclides at TRIGA-TRAP

Dissertation zur Erlangung des Grades

"Doktor der Naturwissenschaften"

im Promotionsfach Kernchemie

am Fachbereich Chemie, Pharmazie und Geowissenschaften

der Johannes Gutenberg-Universität

in Mainz

Dennis Renisch

geb. in Bad Soden

Mainz, den

09.05.2016

Date of oral examination: 23.06.2016

D77

# Contents

# List of Figures

# List of Tables

# Abstract

The TRIGA-SPEC setup is dedicated for high-precision measurements of ground-state properties of exotic nuclides, like fission products or transuranium nuclides. For the online coupling of TRIGA-SPEC to the TRIGA Mainz research reactor, fission products are transported from a target chamber close to the reactor core by a gas-jet system to an ion source, which provides the connected experiments with a radioactive ion beam for the actual measurements. The design, installation and operation of the online ion source was a major part of the work described in this thesis. In addition, investigations on the optimal conditions of the gas-jet system for a reliable ion source operation were performed and the coupling of the ion source part to the subsequent elements of the beamline was conducted.

The second part of this thesis deals with high-precision mass measurements on transuranium nuclides with the Penning-trap mass spectrometer TRIGA-TRAP, which is one branch of the TRIGA-SPEC setup. These measurements contribute to a mapping of the region of the chart of nuclides around the deformed shell closure at $N = 152$. The masses of some of the investigated nuclides are directly measured for the first time. Due to the appearance of systematic inconsistencies during the evaluation of the mass measurements, the focus of the final section of this thesis lies in the identification and correction of the sources of the observed inconsistencies.

# Überblick

Das TRIGA-SPEC Experiment ist für hochpräzise Messungen von Grundzustandseigenschaften exotischer Nuklide, wie Spaltprodukte oder Transurane, ausgelegt. Für die online-Anbindung von TRIGA-SPEC an den TRIGA Mainz Forschungsreaktor müssen die Spaltprodukte mittels eines Gas-Jet Systems aus einer Targetkammer nahe dem Reaktorkern zu einer Ionenquelle transportiert werden, welche die angebundenen Experimente mit einem radioaktiven Ionenstrahl für die eigentlichen Messungen versorgt. Design, Aufbau und Betrieb der online-Ionenquelle war ein Hauptteil der vorliegenden Arbeit. Zusätzlich wurden Untersuchungen bezüglich der optimalen Bedingungen des Gas-Jet Systems für einen zuverlässigen Ionenquellenbetrieb durchgeführt und die Ankopplung der Ionenquelle an die weiteren Elemente der Strahlstrecke vorgenommen.

Der zweite Teil dieser Arbeit beschäftigt sich mit hochpräzisen Massenmessungen von Transuranen mit dem Penningfallen-Massenspektrometer TRIGA-TRAP, das einen der beiden Zweige von TRIGA-SPEC bildet. Diese Messungen tragen zur Vermessung der Region der Nuklidkarte um den deformierten Schalenabschluss bei $N = 152$ bei. Die Massen einiger der untersuchten Nuklide wurden zum ersten Mal direkt gemessen. Aufgrund des Auftretens von systematischen Unstimmigkeiten während der Auswertung der Massenmessungen wurde der Fokus im abschließenden Teil dieser Arbeit auf die Identifizierung und Korrektur der Quellen der beobachteten Unstimmigkeiten gelegt.

# 1 Introduction

Gaining a better understanding of the fundamental forces between nucleons and the constitution of atomic nuclei is an ongoing challenge for theoretical and experimental physicists. While theorists develop even more precise nuclear models to make predictions about the stability of nuclides far from the line of $\beta$-stability, experimentalists aim for high-precision measurements of fundamental properties of more and more exotic nuclides, to test and support the theoretical predictions.

The production and preparation of exotic isotopes, either in very neutron-rich or neutron-poor regions or in the superheavy element (SHE) realm of the chart of nuclides is a major challenge. On the one hand, special facilities, like strong neutron sources or accelerators, are needed for the production. On the other hand, half-lives are becoming shorter and production rates lower when moving further towards more exotic nuclides. Specialized production, transfer and measurement procedures have to be established for those purposes.

## 1.1 Motivation of mass measurements

One important value to characterize the stability of a nucleus and hence the sum of all interacting forces between the nucleons is the binding energy (BE) [1, 2]. A common method for a model independent determination of the binding energy is a precise measurement of the mass excess

$$\Delta m = Z \cdot m_P + N \cdot m_N - m_{nucl} \tag{1.1}$$

with the number $Z$ and mass $m_P$ of protons, the number $N$ and mass $m_N$ of neutrons and the mass of the bound nucleus $m_{nucl}$. By applying Einstein's mass-energy-relation $E = mc^2$, the mass excess $\Delta m$ can be converted into the binding energy of a nucleus

$$BE_{nucl} = \Delta m c^2 = (Z \cdot m_P + N \cdot m_N - m_{nucl})c^2. \tag{1.2}$$

A good approach to calculate the binding energy of a nucleus is the Bethe-Weizsäcker mass formula [3], based on the liquid drop model. The major drawback of this model is that it is incapable to explain the increased stability of nuclei at the so-called magic numbers. These magic numbers represent closed neutron or proton shells in analogy to the electron shells of an atom. A shell closure can be identified experimentally by determination of the neutron or proton separation energy. The last nucleon of a shell is

bound stronger than an additional nucleon, so that a sudden decrease of the separation energy can be observed at the magic numbers. However, experimental data show an odd-even staggering in the binding energy, predominating other low-energy effects if the single nucleon separation energy is regarded. This effect can be canceled out, if the two-neutron and correspondingly the two-proton separation energy

$$S_{2N}(N,Z) = BE(Z,N) - BE(N-2,Z) \tag{1.3}$$

$$S_{2P}(N,Z) = BE(Z,N) - BE(N,Z-2) \tag{1.4}$$

are regarded instead.

### 1.1.1 Nucleosynthesis

Unravelling the processes which lead to the natural abundance of the elements and isotopes in the solar-system is an ongoing field of research in astrophysics [4, 5]. While the lightest elements, like hydrogen and helium, were created in the big bang, heavier elements were produced later via different paths. Fusion processes inside stars can create all elements up to $Z = 26$, Iron. Heavier elements are supposed to be produced by neutron-capture processes followed by $\beta^-$-decay [6–8]. The number of neutrons which are captured before a $\beta^-$-decay occurs depends on the neutron flux and the $\beta^-$-decay half-life. If the flux is low, so that the capture rate is smaller than the decay rate, a neutron-capture is followed by a $\beta^-$-decay before the next neutron can be captured. This is the so-called s-process. This path can go up to Bi-209, but a further neutron capture leads to an alpha emitter, so the s-process cannot explain the abundance of heavier radionuclides.

If the flux is high enough, the capture rate is so high that several neutrons can be captured before a $\beta^-$-decay happens. In this case nuclides far away form the valley of stability are reached. The exact path of this so-called r-process [8, 9] is still unknown, because many of these very exotic nuclides could not have been sufficiently investigated yet, due to low production rates and/or short half-lives. The exact path of the r-process depends on the binding energy of the additional neutron. If this binding energy becomes too small, the process reaches a waiting point until the next $\beta^-$-decay occurs. Afterward, further neutron captures can happen. The path of the r-process is best known around the magic neutron number $N = 82$. Because of the high stability of the closed neutron shell the binding of an additional neutron is reduced, so that in this region the r-process approaches known nuclides. The r-process ends when nuclides are reached which are so

unstable that spontaneous fission becomes the primary decay mode. This is estimated to happen around mass number $A = 260$ [10], but the exact end point of the r-process is still unknown.

Obviously, the path of the r-process depends on ground-state properties like mass and half-life of the nuclides in the neutron-rich region of the chart of nuclides. Thus, high-precision measurements of these properties are important for astrophysical calculations and predictions [2, 11–13]. Fission products are of particular interest because they are in a region of the chart of nuclides close to the expected r-process path (see fig. 1.1) and because they can easily be produced. More neutron-rich nuclides would be even more interesting, but special accelerator facilities, like FAIR [14], are necessary for the production.

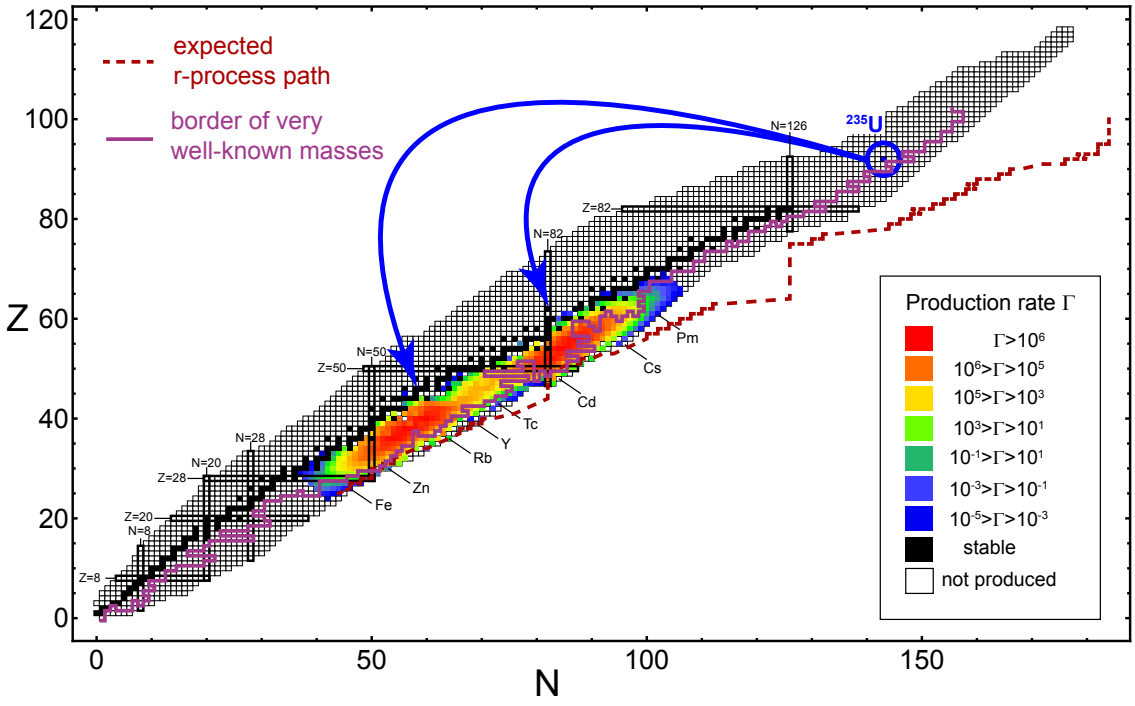


**Figure 1.1:** Chart of nuclides with calculated productions rates of fission products [15] yielded from a 300 $\mu$g $^{235}$U target in the TRIGA Mainz reactor. The possible contribution of TRIGA-TRAP is illustrated by the border of well-known masses, beyond which the mass uncertainty gets larger than 10 keV [16]. The expected r-process path is shown as well. The graph is taken from [17].

### 1.1.2 Direct mass measurements in the heavy and superheavy element region

As pointed out above, shell effects have significant influence on the stability of nuclei [18, 19]. In fact, elements with $Z > \approx 103$ are unstable against spontaneous fission (sf),

if the liquid drop model is applied. Only by taking shell effects into account, the fission barrier is increased, so that for many nuclides in this superheavy element (SHE) region an $\alpha$-decay becomes the dominant decay mode or the half-life for sf is significantly increased. So, the identification and characterization of closed nucleon shells beyond the known magic numbers is of special interest for SHE research. At $Z = 100$, $N = 152$ [20, 21] and at $Z = 108$, $N = 162$ [22] regions of enhanced stability could be identified, which could be related to deformed shell closures. But most of the experimental data concerning nuclear binding energies in this region rely on measurements of the decay products. The energy release of all nuclides belonging to a decay chain is traced until a well-known nuclide is reached, whose mass is experimentally determined. The extraction of information about binding energies from these decay data results in large statistical uncertainties created by error propagation, depending on the length of the decay chain. Additional uncertainties are introduced by the population of nuclear states, whose ordering and transition energies are often unclear. Therefore, direct high-precision mass measurements are very important, to check and improve the accuracy and consistency of the existing values [20]. By pinning down certain nuclear masses by direct measurements, it is also possible to use these nuclides as well-known anchor points for interconnected decay chains.

So far, direct mass measurements beyond uranium have been performed only on some No and Lr isotopes at SHIPTRAP [21, 23] and on $^{249}$Cf, $^{241,243}$Am and $^{244}$Pu at TRIGA-TRAP [24]. Additional nuclides in the vicinity of the deformed shell closure at $N = 152$ have been investigated at TRIGA-TRAP in the frame of this work (see fig. 1.2).

## 1.2 TRIGA-SPEC outline

The TRIGA-SPEC collaboration, centered at the research reactor TRIGA Mainz at the Johannes Gutenberg-University, aims for the detection of ground-state properties of exotic nuclides, particularly of long-lived actinides and neutron-rich fission products. TRIGA-SPEC contains two experimental branches: the collinear laser spectroscopy setup TRIGA-LASER and the double Penning-trap mass spectrometry setup TRIGA-TRAP [25, 26].

Regarding the online coupling of TRIGA-SPEC to the TRIGA Mainz, the production, extraction and transport of fission products out of the TRIGA reactor and the subsequent ionization inside a high-temperature surface ion source are discussed in the framework of this thesis. The produced ion beam is guided through the so-called common beamline, including i.a. a 90° dipole magnet mass separator and a radiofrequency cooler/buncher,

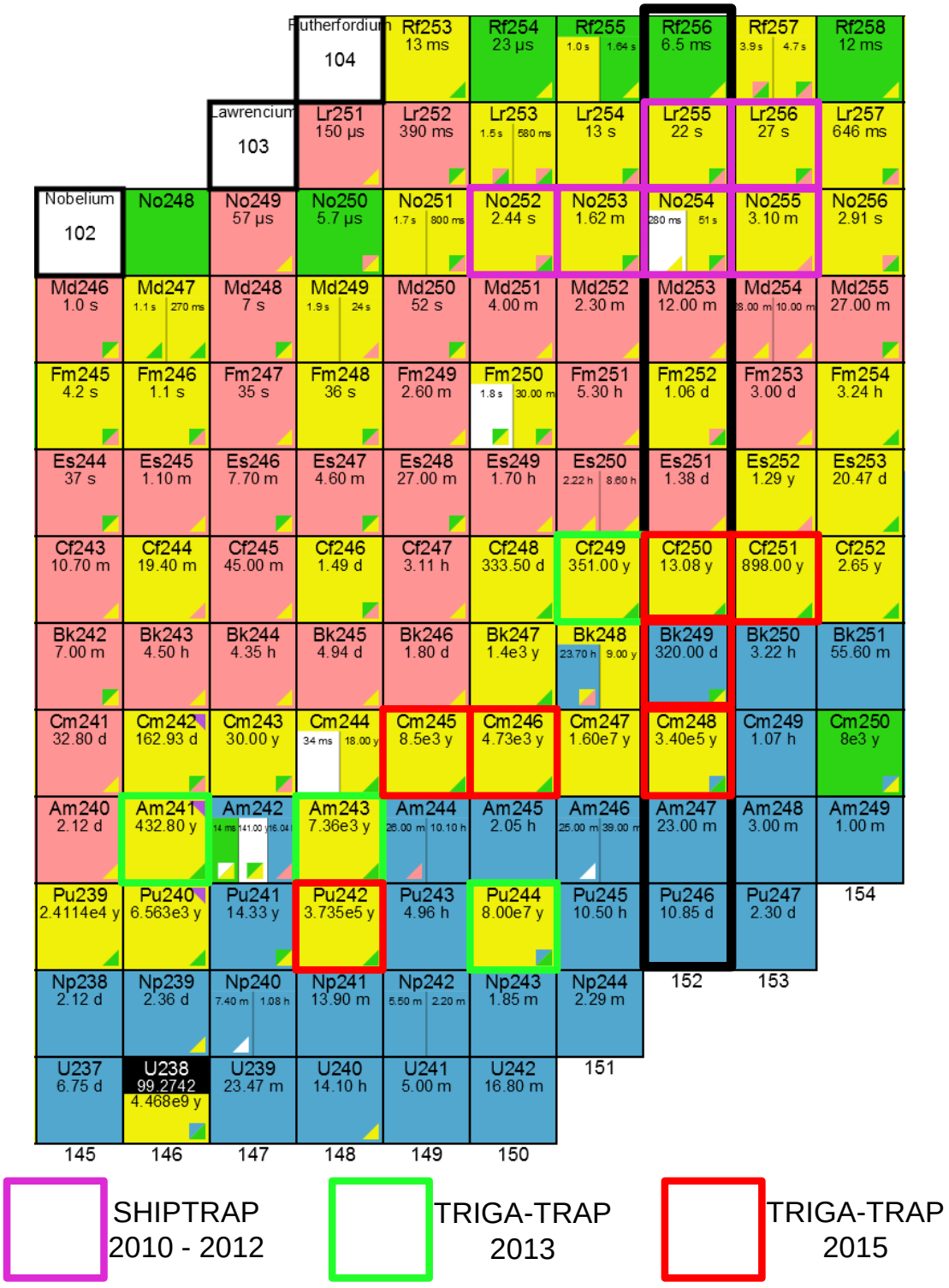


**Figure 1.2:** Detail view of the chart of nuclides around the deformed shell closure at $N = 152$ (bold black line). Direct mass measurements of heavy nuclides have been performed at SHIPTRAP [21, 23] and TRIGA-TRAP [24]. The results of the measurements of TRIGA-TRAP in 2015 are presented in this thesis.

in order to provide the experimental sections of TRIGA-SPEC with (radioactive) ions. The necessary theoretical background and the experimental setup of the different stages of the beamline are presented in sections 2 and 3. The efficiencies of the transport and ionization of several fission products, the ion beam characterization along the beamline and a conclusion about the overall performance of the online coupling are presented in section 4.

The second main topic of this thesis will be the presentation and discussion of the latest high-precision mass measurements of transuranium nuclides, performed with the Penning-trap mass spectrometer TRIGA-TRAP. The Penning trap fundamentals (sec. 2.4), the TRIGA-TRAP setup (sec. 3.4), the results of the mass measurements and a discussion of the encountered problems during the measurements (sec. 5) will be presented.

# 2 Theoretical fundamentals

This section shall give an overview about the most important theories which are necessary to understand the experimental procedures and measurements presented in the following sections of this thesis. For more detailed information see the corresponding references.

## 2.1 Neutron-induced fission

At the TRIGA-SPEC facility the thermal neutron-induced fission of actinide targets is used for the production of fission products. The TRIGA Mainz research reactor acts as a strong neutron source, which initiates neutron-induced fission processes. Technical details about the TRIGA Mainz are presented in sec. 3.1.

In principle, every nucleus is fissionable, as long as sufficient excitation energy is transferred so that the so-called fission barrier $E_f$ can be overcome. The needed excitation energy can be delivered by the kinetic energy or the binding energy $E_B$ of the incoming neutron. The height of the fission barrier and accordingly the amount of energy which has to be transferred depends on the constitution of the nucleus. For even-even nuclides, like U-238 or Pu-244, the binding energy of the additional neutron is not high enough to ignite the fission process ($E_B < E_f$). In order to fission these nuclides, the necessary energy must come from the kinetic energy of the projectile, so fast neutrons with energies in the order of a few MeV are needed.

In nuclear reactors the fission induced by thermal neutrons, with a kinetic energy of only about 0.0025 eV, is the common process. Only even-odd nuclides, like U-235, Pu-239 or Cf-249, can be fissioned this way. In the case of even-odd nuclides the additional neutron creates an even-even compound nucleus. Even-even nuclei are in general more stable than even-odd nuclei, so the last neutron is bound strongly in order to reach this energetically favored state. This is the reason why $E_B > E_f$ for these nuclides, which means that the binding energy of the neutron is already sufficient to start the fission process [27, 28].

Beside the fission products also 2-3 neutrons are released during the fission process. These free neutrons can be used to keep alive a chain reaction of neutron-induced fission, as it is done in nuclear reactors. In a research reactor, some of the spare neutrons, which are not needed to maintain a fission chain reaction, can be used for physics and chemistry experiments. At the TRIGA-SPEC facility, an additional amount of fissionable material inside a target chamber can be placed close to the reactor core for this. The fission products, which are produced inside this chamber can be transported to TRIGA-SPEC

by a gas-jet system (sec. 2.2).

In general, the neutron-induced fission occurs asymmetric, so that the distribution of fission products per mass number has two maxima, as shown in fig. 2.1. For U-235, the light branch of the fission products has its maximum around mass number $A = 100$ and the heavy branch around $A = 140$. For heavier fissionable material the light branch shifts to larger masses, whereas the heavy branch remains in the vicinity of $A = 140$, because it is stabilized during the fission process due to shell effects around the magic numbers $Z = 50$ and $N = 82$ [27].

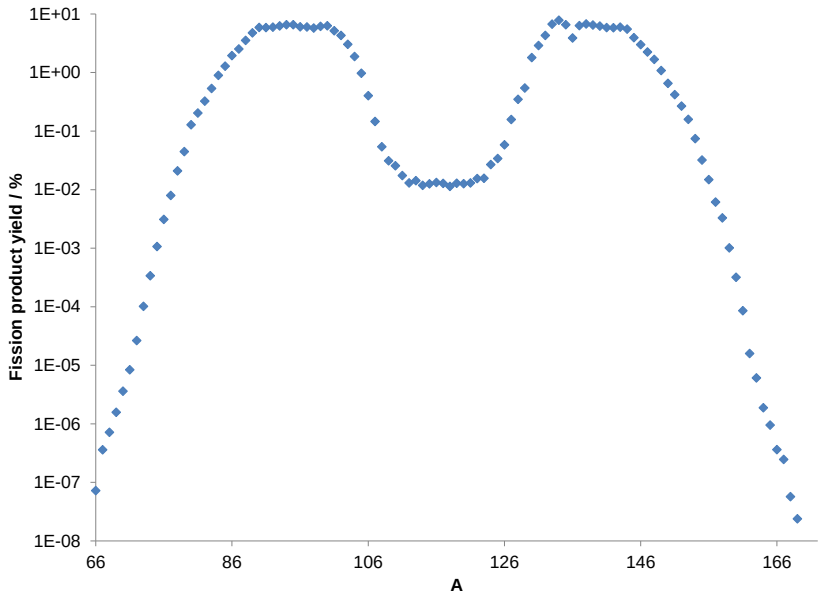


**Figure 2.1:** Distribution of fission products from the thermal neutron-induced fission of U-235 as a function of the mass number $A$.

With the known fission product distribution, the total amount of fissionable target material n($^{235}$U), the thermal neutron flux $\Phi_{n,therm}$ at the position of the target and the fission cross section of the target material $\sigma_f$, the absolute production rate $\Gamma(Z, N)$ of the different fission products can be calculated:

$$\Gamma(Z, N) = n(^{235}U)\sigma_f \Phi_{n,therm} \cdot P(Z, N) \tag{2.1}$$

$P(Z, N)$ is the independent fission yield of a certain nuclide, which are listed in literature [15].

Figure 2.2 shows the binding energy per nucleon BE/$A$ over the mass number $A$. The maximum of the distribution is reached around mass number A = 60, corresponding to $^{62}$Ni and $^{56,58}$Fe as the nuclides with the highest binding energy per nucleon of about

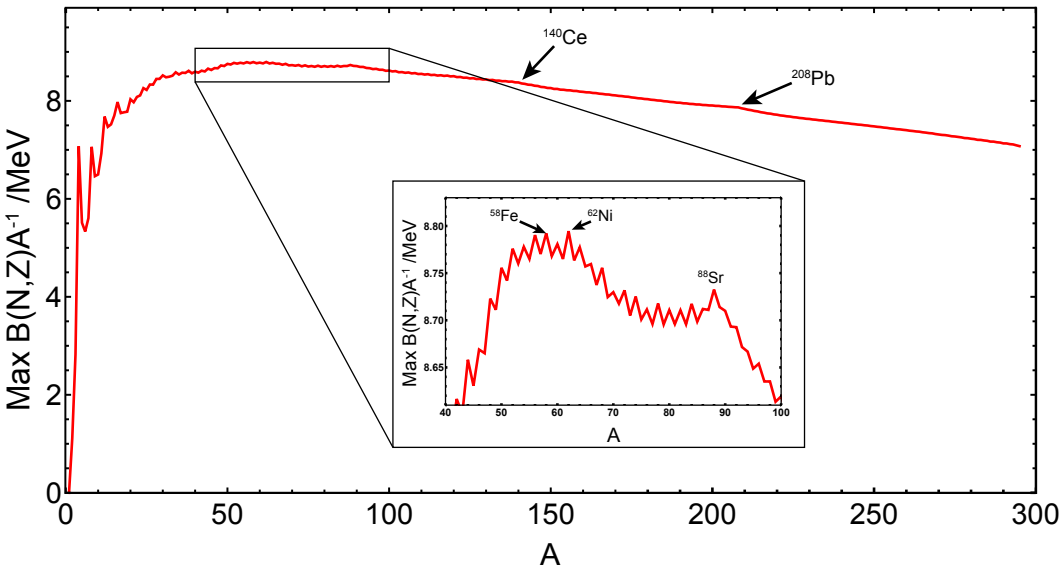


**Figure 2.2:** Binding energy per nucleon as a function of the mass number [16].

8.8 MeV [29]. $^{235}$U has a significantly lower binding energy per nucleon of only about 7.6 MeV. After the fission process two fission fragments with higher binding energy per nucleon are obtained. The total energy gain is 0.8 - 0.9 MeV/$A$, which corresponds to about 200 MeV per fission [27, 30]. This total energy is split among all particles released during the fission process, like the two main fission products, emitted neutrons and $\gamma$-rays. The two fission products gain in sum about 170 MeV of total kinetic energy. Due to momentum conservation the heavier fission product has an energy of about 70 MeV, whereas the lighter fission product ends up with about 100 MeV [31].

## 2.2 Gas-jet and aerosol basics

Radioactive nuclei are of special interest for a wide range of experimental physics setups. Nowadays, modern isotope production facilities, like accelerators or research reactors, can provide a wide range of neutron-rich, neutron-poor or even superheavy nuclides. By getting to more and more exotic regions of the chart of nuclides, the handling of these nuclides becomes more difficult, because, in general, production rates get lower and half-lives get shorter. Hence, it is necessary to use efficient and fast transport systems to bring the radioactive isotopes from the production site to the connected experiments. Usually, an ion beam is needed for physics experiments, in order to manipulate and investigate the produced isotopes by interaction with electric and/or magnetic fields. After the formation of the ion beam, a separation of specific isotopes is a common process, in

order to remove unwanted species and to reduce background. During the past decades several applicable ISOL (Isotope Separator On-Line) techniques have been developed [32–34], e.g. ISOLDE at CERN [35], IGISOL (Ion Guide Isotope Separator On-Line) at the University of Jyväskylä [36, 37] or chemical reactions of refractory elements and subsequent ionization of the formed compounds [38, 39].

TRIGA-SPEC uses an aerosol supported gas-jet system for the extraction and transport of fission products from the TRIGA Mainz research reactor to an online ion source. Some major properties of such a gas-jet system will be discussed, in order to identify crucial parameters which contribute to the transport efficiency.

The technique was introduced in the late 1960's [40] and became very popular in the following decades by coupling gas-jet based transport systems to a wide range of radioactive ion beam facilities, like accelerators [41–43], spontaneous fission sources [44] or research reactors [45–47].

Intense studies on gas-jet systems have been performed in order to understand the fundamental parameters and limitations of this new technique and to optimize the systems with respect to transport efficiency and speed [48–50]. The importance of the presence of aerosol particles within the carrier gas has become clear during these studies and different combinations of carrier gas and aerosol material have been developed. The nature and size of the aerosol particles thereby play an important role for the overall efficiency of the gas-jet transport. Nowadays, aerosol systems based on inorganic salts, like NaCl, KCl or $PbCl_2$, ensure high transport rates over distances of several meters [45, 51–53]. Although these systems are known for more than 40 years now, further investigations on known materials, like carbon cluster [54], or development of new aerosol materials, like $CdI_2$ [55], are still going on to optimize the transport under specific conditions.

The basic idea of the gas-jet technique is to thermalize the produced radionuclides in a gas filled stopping chamber after they recoil from the target. Depending on the production process, the recoil products can have kinetic energies of several MeV. Fission products from neutron-induced fission of $^{235}$U have energies of about 70-100 MeV (see sec. 2.1). This high kinetic energy gives the radionuclides a range of several centimeters in air at atmospheric pressure. In order to avoid a loss of the fission products by attaching to the wall of the chamber it is necessary to ensure a reduction of the initial kinetic energy on a range smaller than the distance between the target and the nearest wall. This can be achieved by enlarging the target chamber (which is in general only possible up to a certain limit due to space limitations at the production site) or by increasing the stopping power of the gas inside the chamber. The stopping power is a function of

the density of the material. So, for a given gas system an increase of the pressure inside the chamber is the best way to raise the stopping power so far that most of the recoiling products are thermalized before they can make contact to a wall. A continuous gas stream through the target chamber is established, so that the radionuclides are flushed with the gas-jet through a capillary system to the experimental site.

The ranges of fission products within different gases at different pressures were determined experimentally[56], see tab. 1. $^{4}$He is a widely-used carrier gas, because its inert properties prevent unwanted reactions between the gas and the radionuclides, like charge exchange reactions. The disadvantage of He is the low mass, which results in a low stopping power that has to be compensated by a significant pressure increase. A good alternative for $^{4}$He is $^{40}$Ar. It is also a noble gas, so chemically nearly as non-reactive as He, but the higher atomic mass results in a stronger stopping power. But for the usage at a research reactor Ar has another disadvantage: because of the high flux of thermal neutrons inside the target chamber a significant amount of $^{40}$Ar (cross section for thermal neutrons $\sigma = 0.64$ b) will be activated by a neutron capture reaction to $^{41}$Ar ($t_{1/2} = 1.8$ h). Therefore, the usage of Ar is undesirable from a radiation safety point of view. An alternative to $^{40}$Ar is $N_2$. Although the molecular mass of $N_2$ (28 amu) is smaller than the mass of $^{40}$Ar atoms, the stopping power and the range of fission products respectively, are almost equal. The reason for this behavior is that additional energy is needed to break the molecular bond between the two nitrogen atoms, leading to a higher loss of energy per collision [56, 57].

**Table 1:** Ranges of $^{102}$Mo produced by thermal neutron induced fission at an energy of 100 MeV in different gases at different pressures [56]. For details see text.

| Pressure / bar | Range in $^{4}$He / mm | Range in $^{40}$Ar / mm | Range in $^{14}N_2$ / mm |
|---|---|---|---|
| 1.0 | 144 | 26.7 | 26.0 |
| 1.5 | 96 | 17.8 | 17.3 |
| 2.0 | 72 | 13.4 | 13.0 |
| 2.5 | 58 | 10.7 | 10.4 |
| 3.0 | 48 | 8.9 | 8.7 |

As mentioned before, the presence of an aerosol is very important to achieve stable transport conditions. For an explanation we have to look at the different forces acting on a particle inside a small gas volume passing through a capillary. Every particle experiences some kind of random walk within the gas volume due to diffusion (see fig. 2.3 left). If the particle gets in contact with the capillary wall, it usually attaches to

the surface and is lost. Assuming a particle with mass $m$ starting exactly in the center of the capillary, the distance from the center after a certain time $t$ is given by

$$d = tNl = tv_D = t\sqrt{2E/m} \tag{2.2}$$

with the mean free path $l$, the number of collisions per second $N = v_D/l$, the diffusion velocity $v_D$ and the particle's energy $E$. The diffusion velocity depends on the mass and the energy of the particle, whereas the energy itself is a function of the temperature $T$. This leads to expression 2.3, showing that the distance from the capillary center is proportional to the temperature and the mass of the particle,

$$d \propto \sqrt{T/m}. \tag{2.3}$$

To keep $d$ smaller than the radius $r_{tube}$ of the capillary, so that the particle is not lost due to diffusion, either the temperature has to be lowered or the mass of the particle has to be increased. Lowering the temperature is technically complex for capillary length of several meters and usually the lower limit is the temperature of liquid nitrogen.

The actual mass of the fission products themselves cannot be affected but the effective mass can be increased by attaching the radionuclide to a larger particle. This is realized by the addition of aerosol particles of a specific size distribution to the carrier gas. Before entering the target chamber, the gas-jet passes an aerosol generator in which the particles are produced. The aerosol is transported into the target chamber, where the radionuclides can adsorb to the particles after thermalization.

While the losses by diffusion can be suppressed by such large particles, the sedimentation due to gravity cannot be neglected any more. The sedimentation velocity $v_{sed}$ is determined by Stoke's law and the distance $d$ a particle has moved away from the center of the capillary in time $t$ is given by

$$d = v_{sed}t \propto m \tag{2.4}$$

While eq. 2.3 is inversely proportional to $m$, eq. 2.4 is directly proportional to $m$. Thus, the aerosol particles have an upper and a lower mass limit. Typical particle sizes which provide good transport conditions are in the range of 10 - 1000 nm and masses of $10^6$ - $10^{10}$ amu.

Beside forces which drive the particles towards the wall of the capillary, there is also a force which pushes them back towards the center. Gas particles close to the capillary wall

are slower than particles closer to the center of the tube due to higher friction. This leads to a parabolic velocity distribution with the maximum in the center. Corresponding to Bernoulli's law, a force $F_B$ directed to the center of the tube acts on particles within the gas (see fig. 2.3 right).

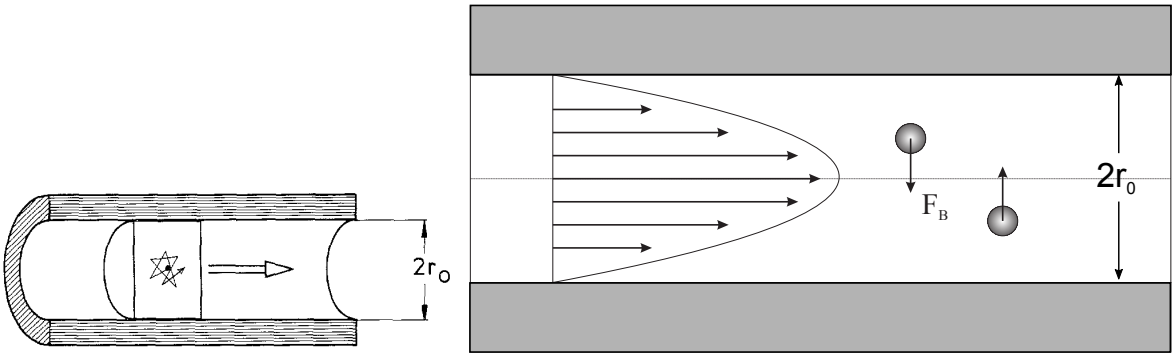


**Figure 2.3:** Left: A particle starting in the center of a capillary moves on a random path due to diffusion while it is transported with the gas. Right: The velocity distribution of a laminar gas flow inside a capillary. The different gas velocities on the two sides of a particle causes a force $F_B$, which is always directed to the center axis of the capillary [52, 57].

All effects which were discussed so far assume a laminar gas flow. An important parameter to distinguish between a laminar and a turbulent flow is the Reynolds number $Re$. It is a dimensionless parameter which can either describe the flow around an obstacle or through a tube. For a cylindrical tube the Reynolds number is given as

$$Re = \frac{\rho_g v_m 2r_{tube}}{\eta} \tag{2.5}$$

with the density of the gas $\rho_g$, the mean velocity $v_m$ and the dynamic viscosity of the gas $\eta$. A gas flow is expected to be laminar up to $Re \approx 2300$. For $Re > 4000$ the gas flow gets usually turbulent. In the range from 2300 to 4000 the behavior of the gas flow can either be laminar or turbulent, which depends mainly on the initial conditions. If the gas flow starts laminar and $Re$ exceeds 2300 there is a good chance that it stays laminar but already a minor disturbance can bring the system to a turbulent state.

An important parameter for the calculation of $Re$ is the mean velocity $v_m$ of the gas flow. In thin capillaries it is possible to achieve gas velocities near the velocity of sound. But the shock wave built up at supersonic gas velocities causes also turbulences which prevent a laminar flow. Therefore it is important to keep the gas velocity below a certain value to ensure a good transport efficiency [52, 57–59].

The formation of aerosol particles occurs like that of rain drops in nature: the vapor of some liquid or of some sublimated solid condenses around present condensation nuclei.

Typical conditions for inorganic salt-based aerosols are oven temperatures around 100 - 150 °C below the melting point of the salt. The total amount, the width and the center of the mass distribution of the formed clusters depend on the growth conditions and can be affected by the temperature and gas flow rate through the aerosol generator. In general, a higher temperature leads to more aerosol particles because more atoms of the solid gain sufficient energy for sublimation. The size of the particles can be controlled by the gas flow rate. Using lower rates, it takes more time to transport the generated particles out of the high temperature zone of the oven, so that a high concentration of particles in the carrier gas is achieved. When reaching a low temperature zone, the coagulation of the particles leads to bigger clusters with a broad mass distribution [52, 59].

### 2.2.1 Skimmer and aerodynamic lens

The gas-jet system transports the radionuclide-loaded aerosol to a high-temperature surface ion source (see sec. 2.3). The capillary ends in front of a skimmer, which connects the gas-jet section and the ion source. The skimmer is a cone-shaped aperture, whose function is to reduce the amount of gas entering the ion source and to reduce the pressure inside and behind the source. On the other hand, as many aerosol particles carrying fission products as possible should pass the skimmer to reach the ion source. The separation between carrier gas and aerosol particles is achieved by the different opening angles of the two species when leaving the capillary. The carrier gas atoms/molecules have only a mass of a few amu, whereas the aerosol particles are several orders of magnitude heavier (see sec. 2.2). Due to their inertia and low diffusion velocity, the opening angle $\alpha_{aerosol}$ is relatively small compared to the angle of the carrier gas $\alpha_{gas}$, which expands much more intensively after leaving the capillary (see fig. 2.4). The carrier gas spreads across the volume in front of the skimmer and can be pumped away.

So, the opening angle depends on the mass of the particles. To narrow the angle, either larger particles or a material with higher molar mass has to be chosen. Another way to increase the amount of aerosol particles reaching the ion source is either to enlarge the aperture of the skimmer, with the drawback of an increased pressure inside the ion source, or by variation of the distance $d$ between the end of the capillary and the entrance of the skimmer.

The influence of different aerosol materials, e.g., KCl, $MgCl_2$, $ZnBr_2$ and $PbCl_2$, and the optimal distance $d$ has been studied at the helium-jet on-line isotope separation facility (HELIOS) at the TRIGA Mainz research reactor [60–63]. The gas-jet and skimmer system used at TRIGA-SPEC is in many technical details similar to that of HELIOS.

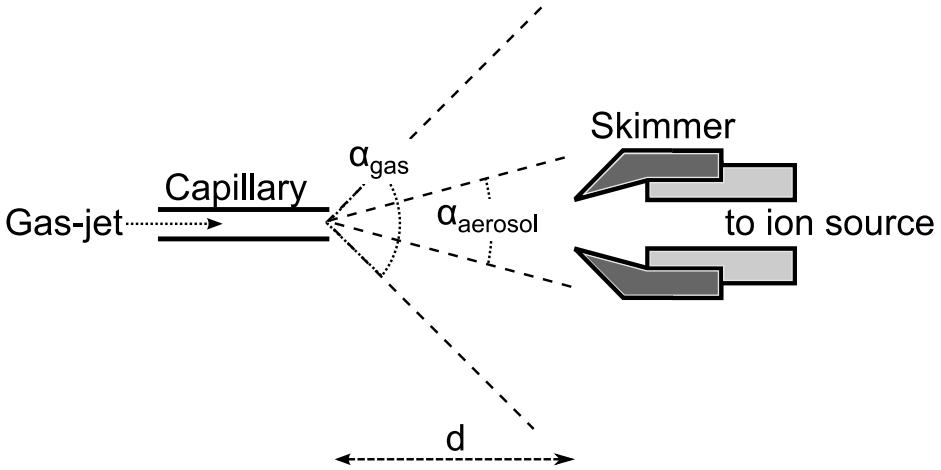


**Figure 2.4:** Sketch of the opening angles $\alpha$ of the carrier gas and the heavier aerosol particles at the exit of the capillary.

The former investigations showed that KCl shows in general the best overall transport efficiency, although its opening angle is bigger, and according to this the skimmer efficiency is lower than for the heavier cluster materials. The optimal distance $d$ is in the range of 4 - 6 mm. For smaller distances the jet divergence increases because of a local gas back pressure in front of the skimmer, which decreases the amount of aerosol that passes through the aperture.

Although the opening angle for the aerosol clusters is much narrower than for the carrier gas, they still have a measurable divergence, so that only a certain fraction (for KCl typically not more than 20 % [62]) of the clusters and the attached radionuclides enter the ion source. A method to collimate the particles has the potential to increase the amount of radionuclides which can be ionized up to a factor of 5. One way to achieve such a collimation is the installation of an aerodynamic lens in front of the skimmer.

An aerodynamic lens consists of one or more focusing orifices separated by spacers (see fig. 2.5). The principle of an aerodynamic lens is based on the alternating contraction and expansion of the gas-jet, when passing the orifices. Particles inside the gas follow the motion of gas depending on their inertia. When the gas is contracted in front of an orifice the particles are pushed towards the center axis. During the subsequent expansion of the carrier gas only small particles can follow the gas flow, while particles with a larger mass remain closer to the center axis than in front of the orifice (see fig. 2.6A). By placing multiple orifices one after another, aerosol particles of a specific mass distribution can be separated from the carrier gas and collimated as a narrow beam on the center axis

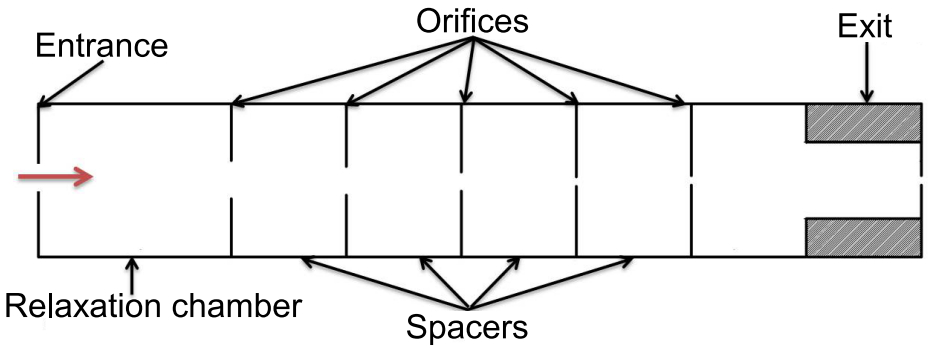


**Figure 2.5:** Sketch of an aerodynamic lens, adapted from [59].

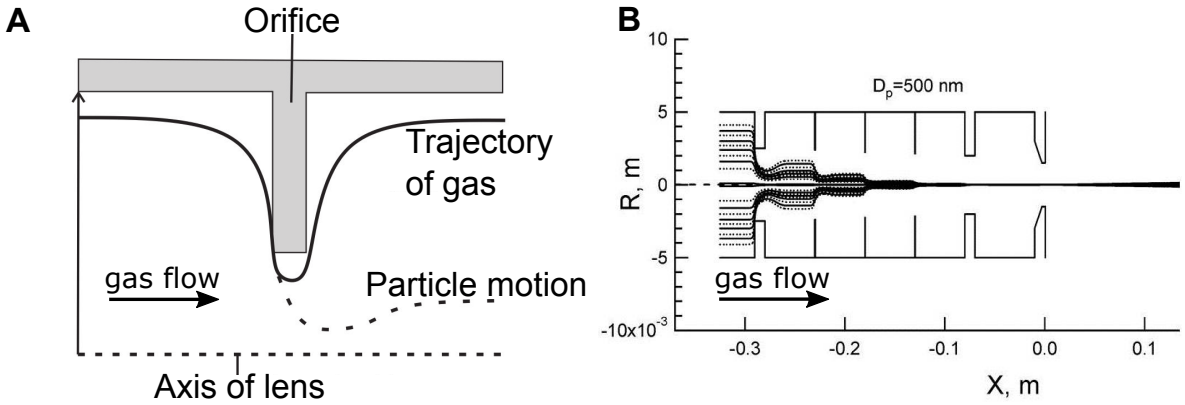


**Figure 2.6:** Left: Trajectories of the carrier gas and aerosol particles inside an aerodynamic lens by encountering an orifice. The particles are separated from the carrier gas due to their larger inertia [64]. Right: Calculated trajectories of particles with a size of 500 nm inside an aerodynamic lens at a flow rate of 97.3 ml/min. Multiple stages result in a focused particle beam [65].

(see fig. 2.6B).

The spacers between the orifices give the gas flow time for relaxation after each stage, because an important condition is that over the whole distance of the lens a laminar and subsonic flow is achieved. Any turbulence would make the flow unstable, destroy any focusing effect and lead to a loss of aerosol particles by impaction.

The specifications of an aerodynamic lens depend on several parameters, like gas flow, pressure in front of and behind the lens, the used carrier gas and aerosol material. Every lens can just handle a certain mass distribution. Particles which are too small (usually $< 25$ nm) are hard to separate from the carrier gas and strong diffusion forces prevent a good collimation. Particles which are too heavy (usually $> 2500$ nm) cannot follow the gas motion due to their inertia and impact on the orifices [59, 64–67].

So, for a given system an aerodynamic lens gives the opportunity to achieve skimmer efficiencies close to 100 % but with the drawback that the system looses some flexibility, because certain parameters have to be kept within rather strict ranges.

## 2.3 Surface ionization

The formation of a radioactive ion beam with an appropriate energy distribution and sufficient ionization efficiency for the connected experiments is a crucial stage for each ISOL facility. Over the past decades a lot of different types of ion sources have been developed, each with individual advantages and disadvantages. Even a description of only the most common techniques would be beyond the scope of this work. See [32, 68, 69] for an overview about different ion sources. The ion source developed and commissioned in the frame of this thesis is a type of high-temperature surface ion source of which the fundamentals will be explained in this section.

Ionization due to contact with hot surfaces, so-called contact or surface ionization, was describe first by Langmuir and Kingdon [70, 71]. As long as the surface temperature is sufficiently high and the contact time between the atom and the surface is long enough to come to thermal equilibrium (typically $10^{-5}$ to $10^{-3}$ s), surface ionization can occur. The ionization efficiency $\beta$ depends on the temperature, the surface material and the element to be ionized. $\beta$ can be described by a form of the Langmuir-Saha equation

$$\beta = \frac{\alpha}{1+\alpha} \tag{2.6}$$

$$\alpha = \frac{n_i}{n_0} = \frac{g_i}{g_0} exp(\frac{\Phi - W_i}{kT}) \tag{2.7}$$

with the degree of ionization $\alpha$, the concentration of ions $n_i$ and neutral atoms $n_0$, the statistical weights of the ionic $g_i$ and atomic $g_0$ states, the work function of the surface $\Phi$, the ionization potential of the atom $W_i$, the Boltzmann constant $k$ and the temperature of the surface $T$ [72]. Table 2 shows calculated ionization efficiencies $\beta$ for K, Ca, Rb, Sr and Y on a hot tungsten surface of different temperatures. For systems with $W_i < \Phi$ (mainly alkali metals on hot surfaces of refractory metals [73]) the ionization efficiency reaches high values, so most atoms are ionized. For alkaline earths the efficiency can still reach a few percent, but for most other elements it is very low.

**Table 2:** Calculated ionization efficiency $\beta$ x 100% according to eq. 2.6 for K, Ca, Rb, Sr and Y on a hot W surface ($\Phi$ = 4.54 eV) for three different temperatures. Literature values from [74].

| Element | $W_i$ / eV | $\beta$ (T = 1500 K) | $\beta$ (T = 2000 K) | $\beta$ (T = 2500 K) |
|---|---|---|---|---|
| K | 4.34 | 70.1 | 61.5 | 55.9 |
| Ca | 6.11 | 0.001 | 0.022 | 0.137 |
| Rb | 4.18 | 89.2 | 80.4 | 72.9 |
| Sr | 5.70 | 0.026 | 0.245 | 0.930 |
| Y | 6.22 | 0.00001 | 0.00038 | 0.00325 |

The counter-intuitive behavior of alkali metals, whose ionization efficiencies degrade slightly with higher temperatures, is caused by shorter contact times with the hot surface. The fraction of neutral vaporized atoms $n_0$ rises accordingly.

Usually only singly positive charged ions are produced by thermoionization, because the second ionization potential is in general significantly higher than the first one. For all further evaluations discussed in this thesis, it will be assumed that higher charge states can be neglected.

Surface ion sources are widely used at ISOL facilities. The advantages are an intrinsic elemental selectivity, simplicity of the construction and the fact that the experimentally observed ionization efficiencies are, in general, significantly higher than expected from eq. 2.6. The reason is that the Langmuir-Saha equation treats only a single contact between an atom and the surface. But one has to distinguish between surface ionization in general and thermoionization inside a hot-cavity ion source. For the latter case additional processes, like the formation of a thermal plasma inside the cavity and multiple wall collisions, make the calculation and prediction of the ionization efficiency more complex. But typically, the chance for a successful ionization is boosted by these effects compared to a single surface contact [75–79].

Surface ion sources cannot only be used to provide an ion beam of radionuclides, but they can also be used as tools for measurements of fundamental atomic properties, like the first ionization potential. This was done recently for element 103, lawrencium, at the one atom at a time scale [80].

## 2.4 Penning trap fundamentals

Penning-trap mass spectrometers are nowadays the most common devices for high-precision measurements of absolute atomic masses and mass differences with a relative precision of $10^{-8}$ or better. The conversion of the mass measurement into a frequency measurement is the main reason why Penning traps can achieve this high level of accuracy. The Penning trap fundamentals, which are needed to comprehend the mass measurements of the transuranium nuclides discussed in sec. 5, will be presented in this section. See the review articles of Brown and Gabrielse [81] or Blaum [2, 12] for a detailed description of the physics of Penning traps.

Different detection techniques are established for Penning-trap mass spectrometry. The time-of-flight ion cyclotron resonance (TOF-ICR) is the method which was used for the measurements performed in the frame of this thesis and will be discussed in detail. Other detection techniques, like Fourier-transform ion cyclotron resonance (FT-ICR) and phase-imaging ion cyclotron resonance (PI-ICR), are under development at TRIGA-TRAP and will be discussed briefly.

### 2.4.1 Motion of charged particles inside Penning traps

A Penning trap confines charged particles in a certain volume. The storage time, in the case of stable nuclides, depends mainly on the pressure that can be reached inside the trap, because a collision with a residual gas particle usually leads to the loss of the stored ion. The radial confinement is achieved by a strong homogeneous magnetic field $\vec{B} = \vec{B}_z$ (z axis is defined to be parallel to the magnetic field). An ion with a charge-to-mass ratio $q/m$ and an initial velocity component $\vec{v}$ perpendicular to the magnetic field lines experiences the Lorentz force

$$\vec{F}_L = q\vec{v} \times \vec{B} \tag{2.8}$$

$\vec{F}_L$ guides the ion on a circular trajectory around the magnetic field lines with the free

cyclotron frequency

$$\nu_c = \frac{\omega_c}{2\pi} = \frac{1}{2\pi}\frac{q}{m}B. \tag{2.9}$$

Equation 2.9 gives already the fundamental relation between the mass $m$ of the ion and $\nu_c$, if the strength of the magnetic field $B$ and the charge state of the ion $q$ are known. Details about the determination of $\nu_c$ will be given in sec. 2.4.3, the calibration of the magnetic field with reference ions is explained in sec. 2.4.4.

In order to confine the ion in all 3 dimensions, an electric quadrupole potential has to be superimposed with the magnetic field. Two fundamental Penning trap designs exist, the cylindrical and the hyperbolic trap (see fig. 2.7). Both types are axially symmetric, so the electric potential $\Phi$ can be expressed in cylindrical coordinates:

$$\Phi(z, r) = U_0 \frac{z^2 - r^2/2}{2d^2} \tag{2.10}$$

$U_0$ gives the applied DC voltage between the central ring electrode and the endcaps of the trap. To achieve a stable, harmonic oscillation the condition $qU_0 > 0$ has to be fulfilled. The characteristic trap dimension $d$ is given by

$$d^2 = \frac{1}{2}(z_0^2 + r_0^2/2), \tag{2.11}$$

with the minimum distance $z_0$ of the endcaps and $r_0$ of the ring electrode to the center of the trap assembly.

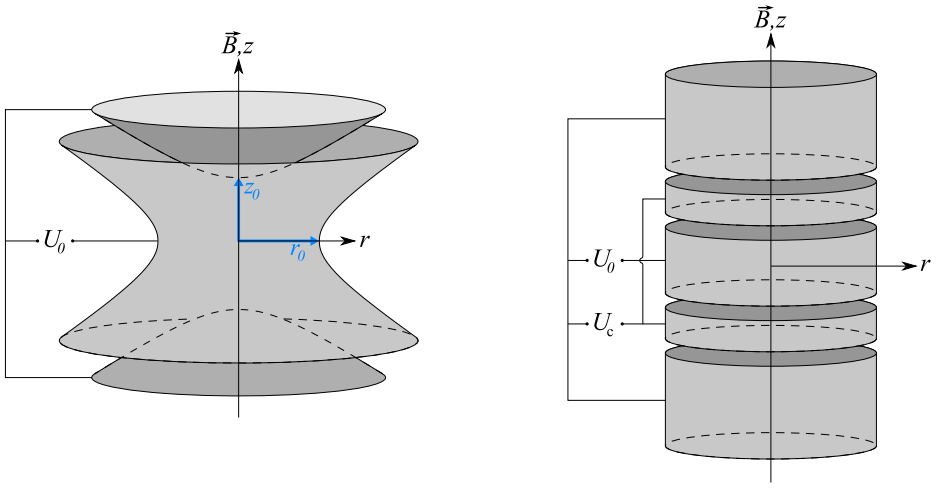


**Figure 2.7:** Hyperbolic (left) and cylindrical (right) electrode geometry for Penning traps [82]. See text for details.

The main advantage of a hyperbolic trap is that the electrodes are formed in a way which matches perfectly the desired ideal quadrupole potential. Compared to a cylindrical trap, a hyperbolic trap provides a larger inner volume without field inhomogeneities. The main drawback is that it is difficult to manufacture the hyperbolic electrodes with the necessary precision. Cylindrical electrodes are much easier to produce with high precision. The drawback is that the electrostatic properties are more difficult to predict, but it is nowadays possible to calculate this analytically.

The axial motion of the ion between the endcaps is decoupled from the magnetic field and can be described as a classical harmonic motion

$$\ddot{z} + \omega_z^2 z = 0, \text{with frequency } \omega_z^2 = \frac{eU_0}{md^2} \tag{2.12}$$

The electric quadrupole potential is usually treated as a relatively weak addition to the magnetic field, because $\omega_z << \omega_c$.

The radial motion of the ion is disturbed by the addition of the electrostatic potential, so it cannot be described by eq. 2.9 anymore. The radial motion is then described by

$$m\ddot{\vec{r}} = q(\vec{E}_r + \dot{\vec{r}} \times \vec{B}), \text{with } \vec{E}_r = \frac{U_0}{2d^2}\vec{r}. \tag{2.13}$$

$\vec{E}_r$ originates from the electric quadrupole field. For $\vec{E}_r \to 0$, eq. 2.13 is reduced to the simple Lorentz force eq. 2.8. But the presence of the repulsive radial potential $\vec{E}_r$ has two effects on the free cyclotron motion: 1) The decrease of the centripetal force results in a reduced cyclotron frequency $\omega_+ < \omega_c$. 2) The cyclotron orbit is superimposed by a circular magnetron orbit, with frequency $\omega_-$ (see fig. 2.8 left).

The magnetron motion has two special properties which are important for the mass-selective buffer-gas cooling technique explained in sec. 2.4.2. 1) The magnetron motion does not depend on the charge or mass of the particle. 2) The magnetron motion is an unbound motion and can be understood as an orbit around the top of a radial potential hill. So any process which drains energy from the motion results in an *increase* of the magnetron radius. In contrast to that, the cyclotron and axial motion are stable, a reduction of their energy results in a *decrease* of their amplitude.

To summarize the trajectory of a trapped ion in an ideal Penning trap (see fig. 2.8 right), the three individual eigenfrequencies of the axial, the reduced cyclotron and the magnetron motion are given as

$$\omega_z = \sqrt{\frac{qU_0}{md^2}} \tag{2.14}$$

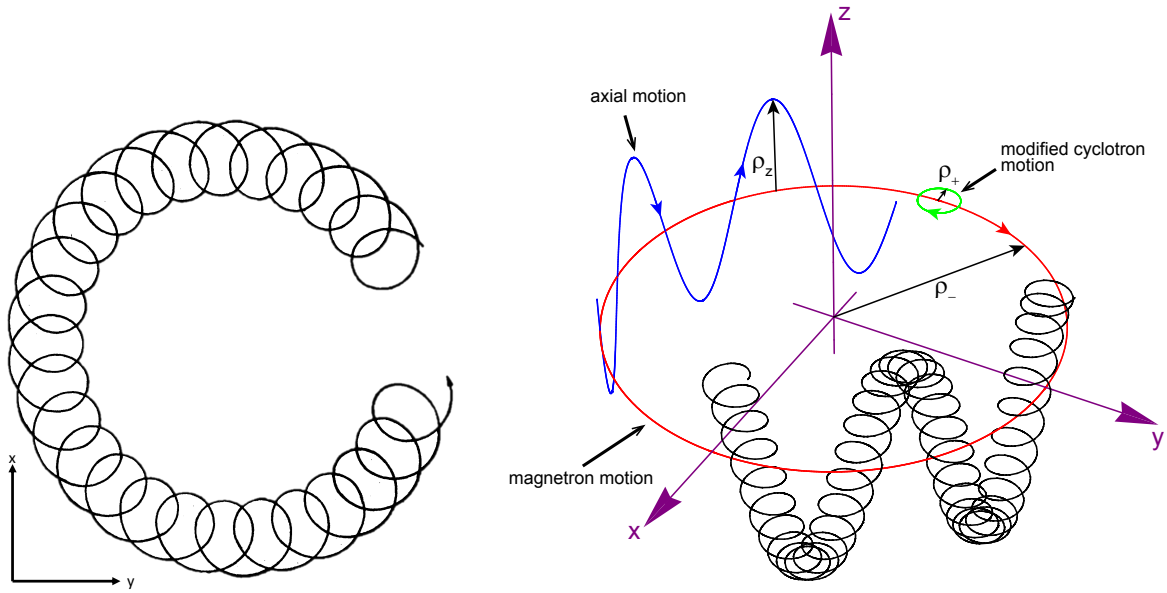


**Figure 2.8:** Sketch of the motion of a charged particle in a Penning trap. The magnetic field is aligned to the z-axis. Left: Projection of the motion onto the xy plane. The motion is the superposition of a modified cyclotron motion and a circular magnetron motion [81]. Right: In addition to the two radial motions, an axial motion between the endcaps of the Penning trap is the third independent eigenmotion. The superposition of all three eigenmotions is displayed by the black line [17].

$$\omega_+ = \tfrac{1}{2}(\omega_c + \sqrt{\omega_c^2 - 2\omega_z}) \approx \omega_c - \tfrac{U_0}{2d^2B} \tag{2.15}$$

$$\omega_- = \tfrac{1}{2}(\omega_c - \sqrt{\omega_c^2 - 2\omega_z}) \approx \tfrac{U_0}{2d^2B} \tag{2.16}$$

The regarded frequencies can be ordered in the following hierarchy

$$\omega_c > \omega_+ >> \omega_z >> \omega_-. \tag{2.17}$$

In addition, certain relations between the different eigenfrequencies hold:

$$\omega_c = \omega_+ + \omega_- \tag{2.18}$$

$$\omega_z^2 = 2\omega_+\omega_- \tag{2.19}$$

Both relations are only valid in an ideal Penning trap. But from eq. 2.18 and 2.19 the so-called invariance theorem [81] can be derived:

$$\omega_c^2 = (\omega_+ + \omega_-)^2 = (\omega_+^2 + 2\omega_+\omega_- + \omega_-^2) = \omega_+^2 + \omega_z^2 + \omega_-^2. \tag{2.20}$$

Eq. 2.20 can be applied even under non-ideal conditions. Nevertheless, for the measurements discussed in this thesis, eq. 2.18 is most important for the determination of $\omega_c$ of the ions under investigation.

In a real Penning trap several deviations from the ideal trapping potential can occur due to electric and magnetic field imperfections or misalignment of the trap [83]. One possibility to treat the trap anyway as an "ideal" trap is the addition of several correction electrodes around the actual trap, which have to be tuned in a way that the existing disturbances are compensated.

### 2.4.2 Manipulation of ion motions inside Penning traps

#### Dipolar and quadrupolar excitation

In order to perform measurements on ions trapped inside a Penning trap, it is necessary to interact with the different eigenmotions. This can be done by applying appropriate AC potentials to the trap electrodes. A certain eigenmotion can be excited by applying a resonant AC dipole field. Such a dipole excitation can be created with an AC potential at two opposite electrodes with amplitude $U_d$, frequency $\omega_d$ and a phase shift of $\Phi_d = 180°$ between the electrodes. To excite the radial motions the ring electrode of the Penning trap has to be segmented, so that the required voltages can be applied (see fig. 2.9).

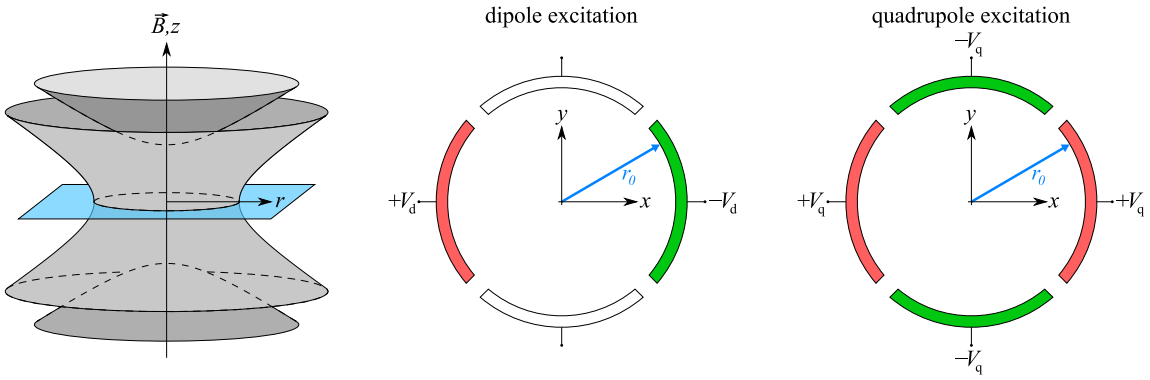


**Figure 2.9:** The segmented center electrode of a Penning trap allows two different excitation schemes. An AC voltage $U_d$ or $U_q$ is applied to the colored segments for a dipole or quadrupole excitation. The colors red and green indicate a 180° phase shift of the applied voltage [82].

Another form is a quadrupole excitation, by applying an AC quadrupole potential to all four segments of the ring electrode (see fig. 2.9 right). The opposing electrodes are phase-synchronous, while the neighboring electrodes have a phase shift of $\Phi_q = 180°$.

If the excitation frequency $\omega_q$ fits to the sum of two individual eigenfrequencies, both motions are coupled, leading to an energy transfer between them. In the case $\omega_q = \omega_c = \omega_+ + \omega_-$ (see eq. 2.18), a full periodic conversion between the magnetron and the reduced cyclotron motion is obtained. This behavior can be used to determine the free cyclotron frequency $\omega_c$. Fig. 2.10 depicts the conversion of a pure magnetron to a pure cyclotron motion, within the conversion period $T_{conv}$.

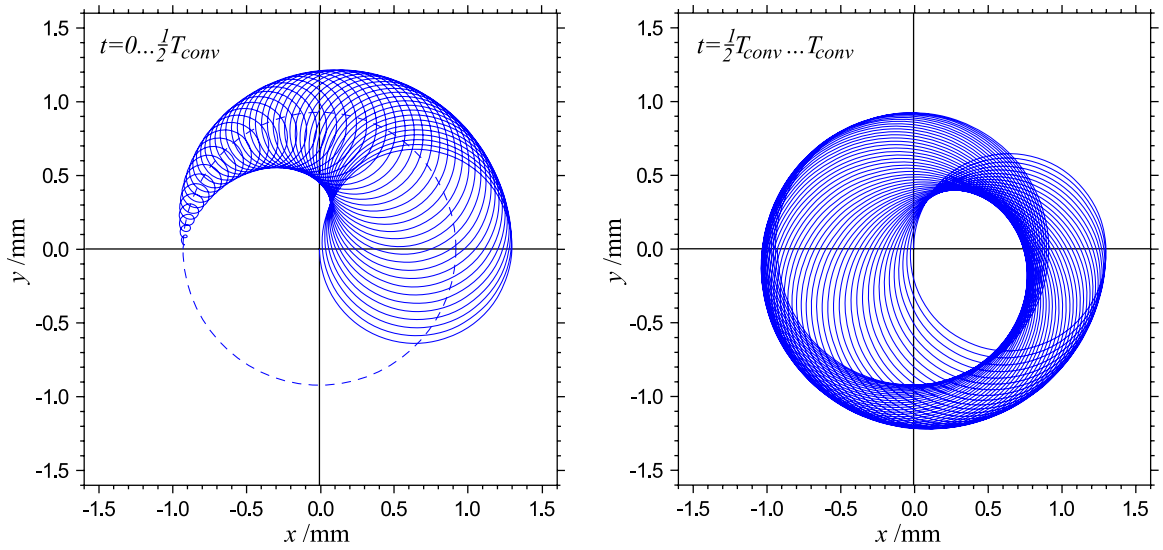


**Figure 2.10:** Calculated conversion of a pure magnetron motion (dashed line on the left) into a pure cyclotron motion, caused by a quadrupole excitation with frequency $\omega_q = \omega_c$. For better clarity, the total conversion is split into to halves (left and right graph) [2].

If at the beginning of the excitation (t = 0) a pure magnetron motion is present, after t = $T_{conv}$ a pure reduced cyclotron motion is received. With respect to the frequency hierarchy (eq. 2.17), $\omega_+ >> \omega_-$, it becomes clear that the ion has gained energy during this process.

### Mass-selective buffer gas cooling

To get rid of unwanted ion species which may disturb the measurement of the cyclotron frequency and to minimize the energy distribution of the captured ions, the so-called buffer gas cooling technique [84] is applied in the purification trap prior to the actual measurement in the precision trap. The cooling technique is based on collisions of the ions with a low temperature buffer gas, so that energy is transferred from the ions to the buffer gas. Helium is usually chosen as buffer gas to avoid unwanted chemical or charge

exchange reactions. An additional advantage of He is the low atomic mass, because in most cases the colliding ion species has a significantly higher mass, so that the trajectory of the trapped ion is unaffected by the collision.

The loss of energy affects all three eigenmotions of the trapped ion. As mentioned above, the axial and the cyclotron motion are stable, so a loss of energy results in a reduced amplitude. In contrast to that, the magnetron motion is unbound, so the radius increases while energy is removed. This can be used to get rid of unwanted ion species. After an initial magnetron excitation, which effects all captured species because the magnetron motion is mass independent, the ions are prepared on a certain magnetron radius. Because of the dampening by the buffer gas, the radius increases further. The second step is an quadrupolar excitation at the cyclotron frequency of the ion species of interest (eq. 2.18). This excitation converts the magnetron motion of the selected ions into the reduced cyclotron motion. The cyclotron frequency is much higher than the magnetron frequency (eq. 2.17), so the cooling of the cyclotron motion occurs very quickly and the ions of interest are centered in the purification trap. The purification trap can then be opened and all trapped ions released towards the second trap. While the ions which were centered prior to the release are guided into the precision trap, the other ion species which are still on a large magnetron radius are lost due to collisions with the trap electrodes. This way a mass-selective cleaning of the initial bunch of ions is achieved.

### 2.4.3 Ion cyclotron frequency measurement techniques

#### TOF-ICR

The time-of-flight ion cyclotron resonance (TOF-ICR) technique is based on the acceleration which an oscillating charged particle experiences by passing a magnetic field gradient. The field gradient is encountered when the ion is released out of the Penning trap, as illustrated in fig. 2.11.

The gradient force

$$\vec{F}_{grad} = -\vec{\nu}(\vec{\nabla}\vec{B}) = -\frac{E_r}{B}\frac{\partial B}{\partial z}\hat{z} \tag{2.21}$$

is proportional to the magnetic moment $\vec{\nu} = \frac{q}{2}r^2\vec{\omega}$ and accordingly to the radial energy $E_r$. The ion is accelerated towards a detector outside the magnetic field and the time of flight, which depends on the initial angular frequency $\omega$ inside the trap, is recorded.

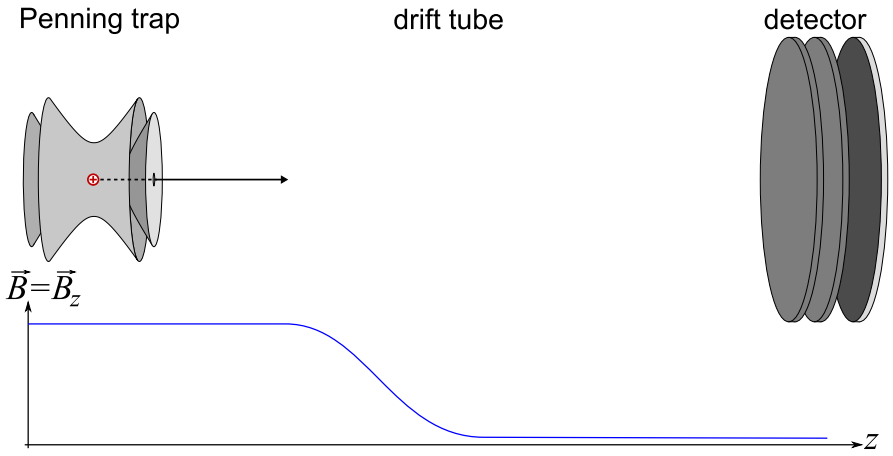


**Figure 2.11:** Principle of the TOF-ICR technique for the measurement of the cyclotron frequency $\omega_c$. The trapped ion is excited with a quadrupolar rf field at a tunable frequency around $\omega_c$ and subsequently ejected through the magnetic field gradient to the detector. The time of flight depends on the degree of conversion and shows a minimum for $\omega_q = \omega_c$ [82].

To achieve a determination of the cyclotron frequency $\omega_c$ the ion has to be prepared at a certain magnetron orbit by applying a dipole excitation at $\omega_d = \omega_-$. Afterward, the magnetron motion is converted into a reduced cyclotron motion by applying a quadrupolar excitation with amplitude $U_q$ for a period $T_q$ around the expected cyclotron frequency $\omega_c = \omega_+ + \omega_- \approx \omega_q$. Finally, the ion is ejected and the time of flight is measured as a function of $\omega_q$. If $\omega_q \neq \omega_c$, the conversion could not or only partly be accomplished. In this case $\omega$ is relatively low, resulting in a longer time of flight to the detector. In the resonant case $\omega_q = \omega_c$ a complete conversion occurs, so that a pure reduced cyclotron motion is achieved. In this case, the time of flight to the detector is significantly shorter, because of the higher frequency $\omega_+$. If the scan of $\omega_q$ around $\omega_c$ is repeated several times, a time-of-flight spectrum as shown in fig. 2.12b can be recorded. The theoretical line shape is determined by the Fourier transformation of the excitation pulse. The sinc(x) function[1] describes the line profile and can be fitted to the experimental data, so that the minimum of the time-of-flight spectrum can be determined, which corresponds to the cyclotron frequency $\omega_c$[2, 83].

As already mentioned, a certain number of ions and scans are needed to get sufficient data points to obtain the cyclotron frequency from an appropriate fit. The statistical

[1] $sinc(x) = \frac{sin(\pi x)}{\pi x}$

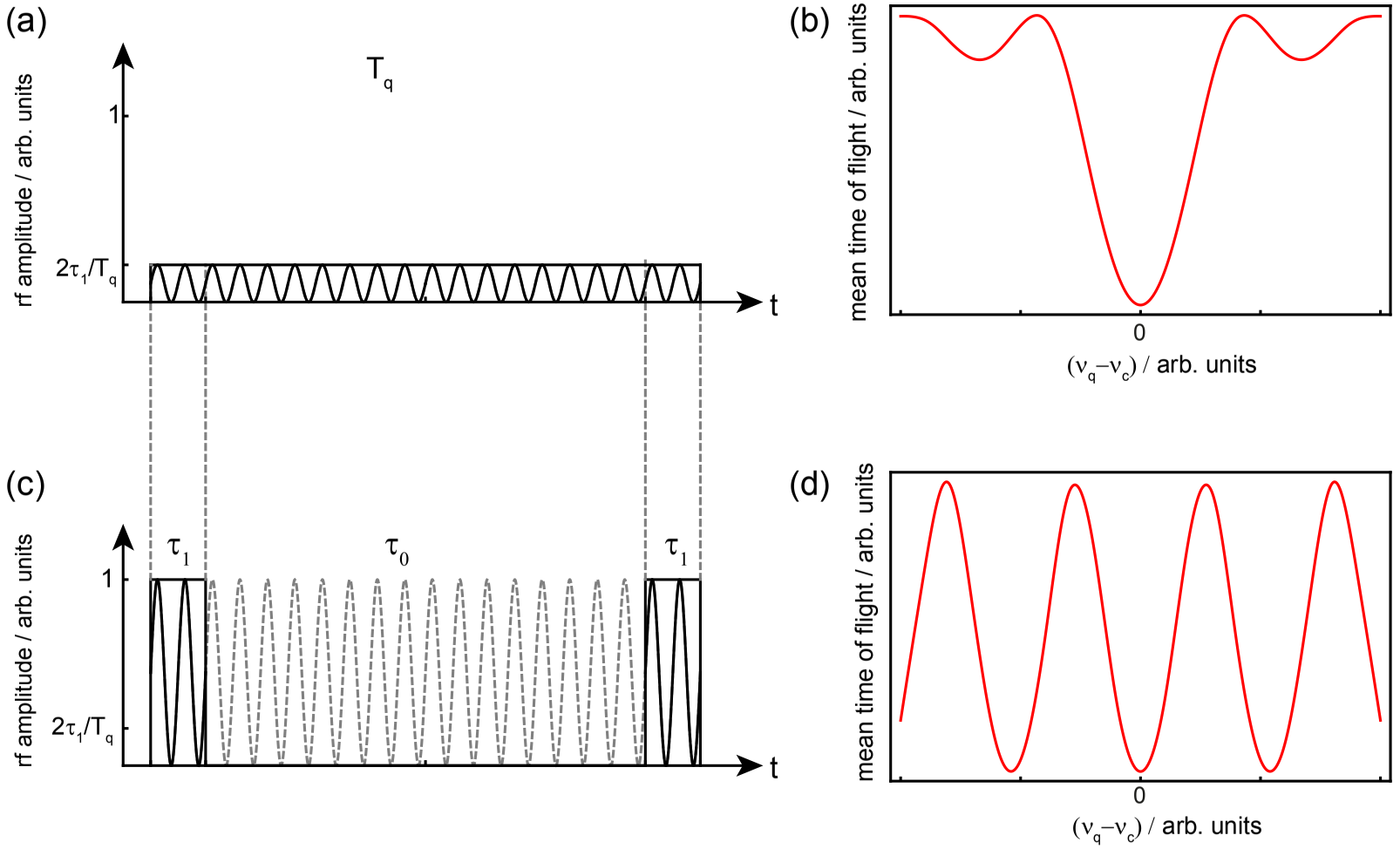


**Figure 2.12:** A continuous excitation (a) results in a time-of-flight spectrum with a minimum at $\omega_q = \omega_c$ (b). For a Ramsey scheme, the excitation is split into two pulses (c), whereas the integral and the total excitation time are kept constant compared to the continuous excitation. The Ramsey scheme pronounces the sidebands and decreases the linewidth [17]. See text for details.

uncertainty [85] of the fit

$$s(\omega_c) \propto \frac{1}{\sqrt{N_{ion}}} \frac{1}{T_q} \tag{2.22}$$

depends on the number of detected ions $N_{ion}$ and the conversion time $T_q$. So, a longer excitation time is favored. But despite the reduction of the statistical uncertainty there are also some drawbacks of a long storage and excitation time. The more time the ion spends in the trap, the higher the risk of a collision with residual gas atoms. Such a collision can either lead to a loss of the particle or it can damp the reduced cyclotron motion, just as it happens in the buffer gas cooling process. A dampening of the cyclotron motion would lead to an increased time of flight of the excited ions, so that the minimum in the time-of-flight spectrum is less pronounced, leading to an increased uncertainty. So, the pressure inside the trap is one limiting factor for the storage time.

In the case of radioactive ions also the half-life $T_{1/2}$ limits the available time for investigations.

Additionally, magnetic field fluctuations over a longer time period [86] lead to an uncertainty in the determined mass. So, a compromise between the gain in precision of the cyclotron frequency by applying a long conversion time and the necessity to keep the overall measurement cycle as short as possible is necessary.

The quadrupolar excitation is not limited to a continuous excitation scheme. Alternatively, the excitation time can be split up into two pulses, separated by a defined waiting time. The overall time as well as the integral of the excitation pulses is kept constant compared to the continuous excitation (see fig. 2.12a/c). So, in the resonant case a full conversion can still occur. This method is called a Ramsey excitation [87–90]. It leads to a pronouncement of the sidebands, but also to a decreased linewidth, which results in a gain in precision up to a factor of three (see fig. 2.12d).

The TOF-ICR technique is a destructive detection method, because the measured ions are lost after the detection. For every single data point, a new bunch of ions has to be captured, excited and ejected, so a continuous supply of ions is needed to acquire the necessary amount of data points.

### FT-ICR

An alternative approach for the determination of the cyclotron frequency is the detection of image charges, induced in the segmented ring electrodes of the trap by the oscillating charge of the trapped ion. The Fourier-transform ion cyclotron resonance

(FT-ICR) technique is a non-destructive method, because the ion is kept stored in the trap during the whole measurement process. Depending on the pressure inside the trap and the half-life of the trapped ion, the storage time can be long enough that a full measurement cycle can be obtained with a single particle. The main challenge of this method is to get a sufficiently high signal-to-noise ratio, despite the magnitude of the image charge only being in the order of a few fA [91].

FT-ICR will be implemented in the future at TRIGA-TRAP. Details about the development and the results of the first test measurements are reported in the thesis of Eibach [17].

### PI-ICR

A third possible detection technique, the phase-imaging ion cyclotron resonance (PI-ICR), is based on the projection of the radial motion of a trapped particle onto a position-sensitive detector [92]. In principle, three different positions are necessary to get information about a certain radial frequency. First, a non-excited ion is ejected from the center of the trap, defining the center position of the radial motion on the detector. Second, an ion is prepared on a well defined magnetron radius and ejected towards the detector, giving a certain spot. In the third step, another ion is prepared on the same magnetron radius, but a certain waiting time before the ejection is added. During this time the radial motion evolves freely in the trap and the ion will be detected at another position. By measuring the phase shift between the ions (see fig. 2.13) the magnetron frequency $\omega_-$ can be determined.

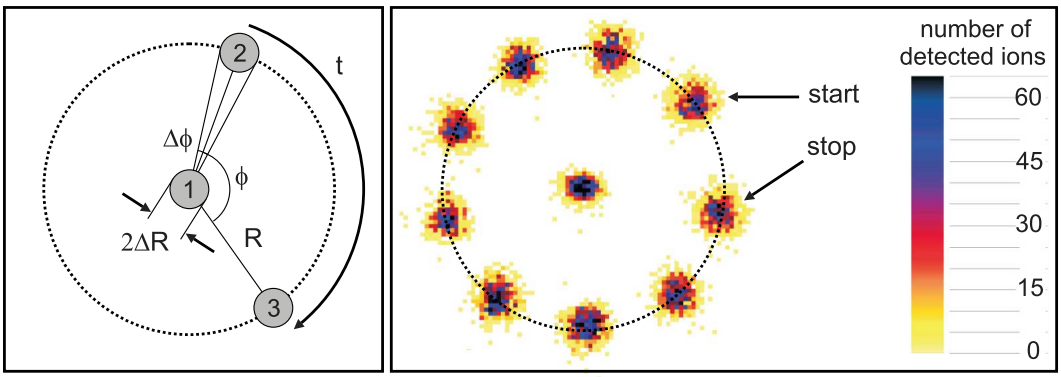


**Figure 2.13:** Left: Principle of the PI-ICR measurement technique. See text for details. Right: Experimentally recorded projection of the position of $^{130}Xe^{+}$ ions for several phases of the magnetron motion. The data was recorded at SHIPTRAP [93].

This method does not work directly for the reduced cyclotron frequency $\omega_+$, because the much higher radial frequency would result in a blurred and diffuse image on the detector. So, after the preparation on a certain reduced cyclotron radius, it is converted to the much slower magnetron motion by a quadrupolar excitation with $\omega_c = \omega_+ + \omega_-$, which can be used to determine $\omega_c$. Compared to TOF-ICR, the PI-ICR technique offers a 40-fold increase in resolving power and a 5-fold gain in precision of the cyclotron frequency determination [93].

The existing time-of-flight section of TRIGA-TRAP will be modified in the future to make PI-ICR measurements possible. First test measurements with a recently installed position-sensitive detector are reported in the diploma thesis of van de Laar [94].

### 2.4.4 Calibration of the magnetic field with reference ions

After the determination of $\omega_c$, eq. 2.9 can be applied to get the mass $m$ of the measured ion species. The main problem is that the magnetic field $\vec{B}$ is not known on a level which is necessary for the aimed precision. Fluctuations of the magnetic field on time scales of the measurement cycles, caused by the flux creep effect [86, 95], makes it necessary to determine $\vec{B}$ periodically. NMR probes are too imprecise, so the magnetic field is determined by a measurement of the cyclotron frequency $\omega_{c,ref}$ of a reference ion with well-known mass $m_{ref}$. This way, the atomic mass of a certain nuclide is given as a function of the cyclotron frequency ratio of the (singly charged) reference ion and the ion of interest:

$$m = \frac{\omega_{c,ref}}{\omega_c}(m_{ref} - m_e) + m_e = r(m_{ref} - m_e) + m_e \tag{2.23}$$

$m_e$ denotes the mass of an electron. Ions of alkali metals are often chosen as reference ions, because their mass is determined with high precision and they are easy to ionize.

Due to imperfections in the electric and magnetic field, a small frequency shift $\Delta\omega_c$ can be added into eq. 2.23. This leads to a relative mass shift

$$\frac{\Delta m}{m} \propto (m_{ref} - m) \tag{2.24}$$

which is proportional to the mass difference between the reference and the ion of interest [17, 96]. This relative mass shift can be avoided by measuring frequency ratios of mass doublets. Since there is not always an adequate reference with the same mass as the investigated nuclides available, it is favorable to keep the mass difference as small as possible. The heaviest alkali ion with well-known mass is $^{133}$Cs, which is more than

100 atomic mass units away from nuclides in the transuranium realm.

A good alternative is the usage of carbon cluster ions $^{12}C_n^+$, n $\in \mathbb{N}$, as reference ions. They provide several advantages [97–100]:

1. One atomic mass unit is defined as 1/12 of the mass of $^{12}C$, so the mass of the carbon clusters is provided without any error by definition.

2. Clusters with different constitution from $C_2$ up to $C_{24}$ or even more can be produced by laser ablation processes, providing a mass reference every 12 amu up to the transuranium mass area $\geq$ 240 amu.

3. Existing systematic errors, like the mentioned relative mass shift, can be studied by carbon cluster cross-checks prior to the actual measurement campaign.

Beside the linking to a known reference for an absolute mass measurement, also the direct comparison of two unknown nuclides can be performed, e.g. for the determination of the Q-value of a mother-daughter-pair of radionuclides [101–103].

# 3 Experimental setup

Figure 3.1 shows a technical drawing of the complete TRIGA-SPEC setup. Important parts, which are explained in detail in the corresponding sections, are labeled in the sketch.

## 3.1 The research reactor TRIGA Mainz

The research reactor TRIGA Mainz [104] is a light-water reactor whose fuel elements consist of an uranium-zirconium-hydride (UZrH) alloy. The uranium is enriched to 20 % $^{235}$U, acting as nuclear fuel. The ZrH moderator matrix is a special feature of TRIGA type reactors. It opens the opportunity to operate the reactor in a pulsed mode, providing a peak power of up to 250 MW for about 25 ms. But for TRIGA-SPEC a continuous production and extraction of fission products is preferred. The TRIGA is thereby operated at a maximum steady-state power of 100 kW.

The TRIGA offers different sample inlets on the top of the reactor platform as well as four large beam ports which penetrate the biological shield and reach close to the reactor core. These beam ports are accessible from the ground floor of the reactor hall. TRIGA-SPEC uses usually beam port A, with a thermal neutron flux of $\Phi_{n,therm} = 9.7 \cdot 10^{10}$ n/(cm$^2$s). When the commissioning phase of the on-line coupling to the reactor is finished, also beam port B is available for TRIGA-SPEC, where the thermal neutron flux is estimated to be about a factor of 2 higher.

### 3.1.1 U-235 target chamber at beam port A

The fissionable target material which is used as fission product source for TRIGA-SPEC is placed inside a target chamber which is mounted at the top of a beam tube which can be inserted into one of the TRIGA beam ports. A sketch of the target chamber is shown in fig. 3.2. The chamber itself has three ports to which capillaries and tubes can be attached. One of the ports is the inlet for the gas-jet. The gas streams through holes in the back-plate of the chamber around the target material and fills the inner volume. Fission products recoiling out of the target are thermalized by the gas and can adsorb to aerosol particles carried with the gas-jet (see sec. 2.2). The central port is the outlet for the gas-jet. The capillary attached here leaves the reactor and guides the gas-jet to the TRIGA-SPEC setup. The third port is connected with a pressure gauge outside of the reactor. The pressure inside of the chamber is a crucial parameter. If it is too low, the stopping power of the gas is too low and fission products are lost due to impact onto the

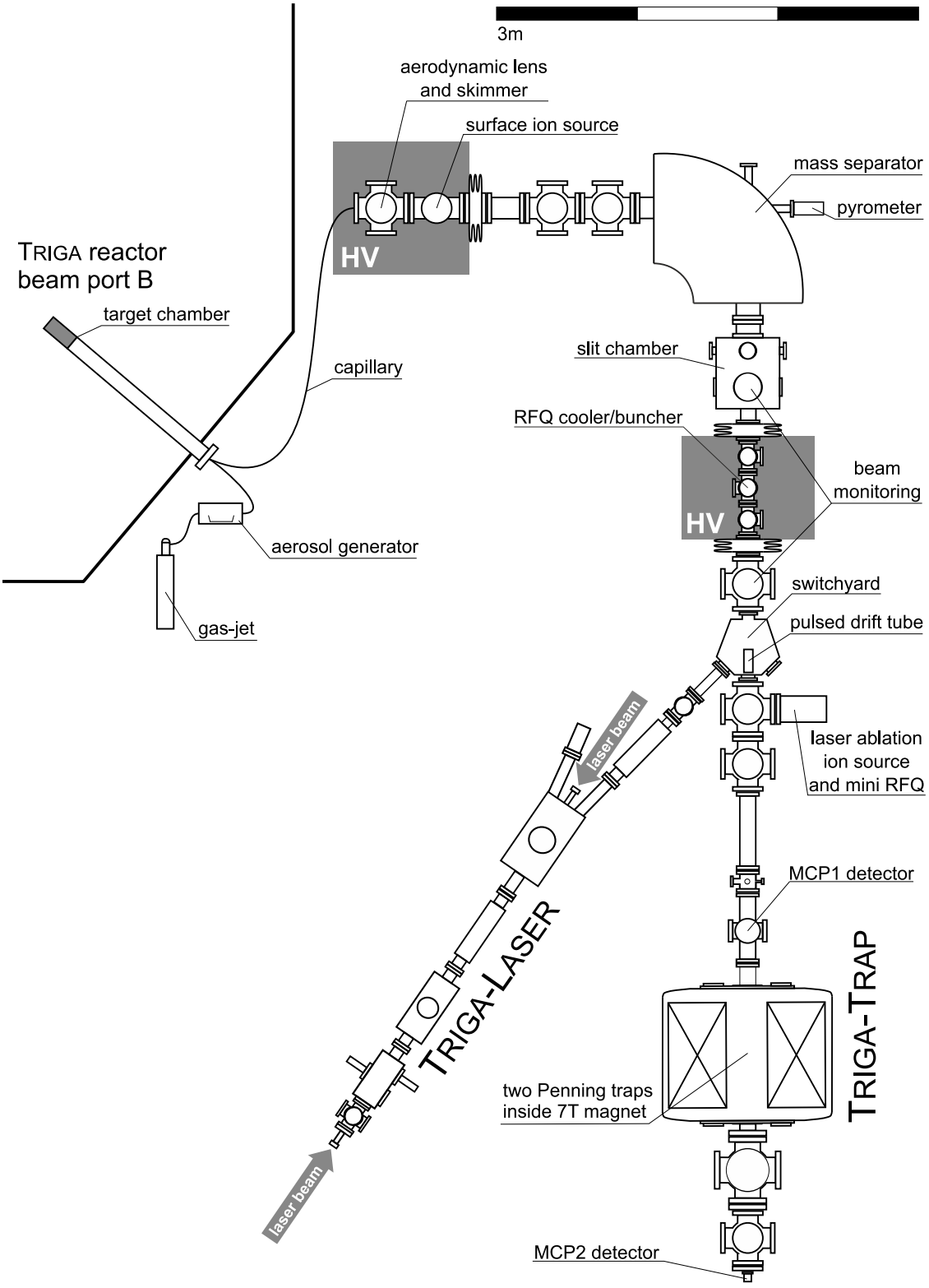


**Figure 3.1:** Ground plan of the TRIGA-SPEC setup. A detailed description of the labeled elements will be given in the following sections.

target chamber walls. A too high pressure should be also avoided to lower the risk of a leakage of the chamber. The pressure can be controlled by the amount of gas entering the chamber and the inner diameter and length of the outlet capillary.

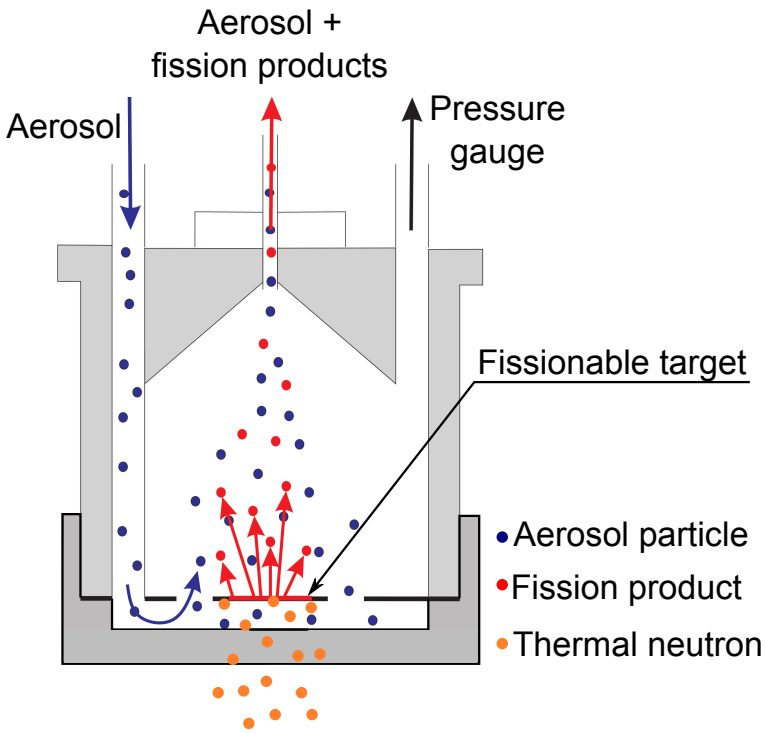


**Figure 3.2:** Sketch of the target chamber at beam port A of the TRIGA Mainz reactor. The gas-jet, carrying aerosol particles, is flushed with a constant flow rate through the chamber, creating a certain pressure. Thermal neutrons from the reactor core enter the chamber through the thin back plate and reach the fissionable target. Recoiling fission products are stopped in the gas volume and attach to available aerosol particles, which transport them out of the chamber. Adapted from [59].

For the first online tests at TRIGA-TRAP a 310 $\mu$g $^{235}$U target, covered with 13 $\mu$m Al, was used. The Al cover holds back the heavy branch of fission products which populates several long-lived nuclei, in order to avoid a contamination of the experimental setup on a long-time scale during the commissioning phase. While the 13 $\mu$m Al layer is sufficient to stop all of the heavy fission products, a small fraction (about 3-8 %, depending on the mass number A) of the lighter branch of fission products passes through the Al layer [105]. The radionuclides which reach the gas-filled volume are already slowed down by interaction with the Al layer, so that an $N_2$ pressure of about 1 bar is more than sufficient to thermalize all fission products within the given volume (see fig. 3.3 top).

In early 2015 a new $^{235}$U target was used for the first time. It consists of a 612 $\mu$g/cm$^2$

$^{235}$U layer with a diameter of 15 mm, which gives a total amount of about 1100 $\mu$g. So, a factor of about 3.5 more fission products was expected to be produced with this target. In addition, the thickness of the Al cover was reduced to 10 $\mu$m. According to Finkle [105], the reduced thickness of the Al layer should be still sufficient to thermalize all fission products without an increase of the pressure inside the chamber. This was also checked by simulations with SRIM2013 [106] (see fig. 3.3). The mean range of the simulated $^{91}$Rb ions increases from 6.5 mm to 11.9 mm due to the thinner Al cover. The closest wall of the target chamber is about 16 mm away from the target area, so all fission products should be stopped within the gas volume. The thinner Al cover should increase the amount of light fission products which reach the gas-filled volume by a factor of 4. So, in total an increase of usable fission products in the order of a factor of 14 was expected with the new target.

For both targets a 100%-catch was performed, in order to get experimental data on the amount of available fission products. The catch was performed by placing a 500 $\mu$m Teflon foil directly on top of the uranium layer, while the TRIGA reactor was operated at 10 kW. After a certain decay time, which is necessary for radiation safety reasons, a $\gamma$-measurement of the Teflon foil was performed. The results of the measurements are discussed in sec. 4. All other fission product catches discussed later were done at 100 kW reactor power. So, for a direct comparison the detected events of the 100%-catches have to be multiplied with 10 to correct for the different neutron flux.

To validate the estimated thermal neutron flux at beam port A, two measurements with wires of an Au-Al-alloy were performed. One wire was placed at the bottom outside of the target chamber, the other wire was placed inside the chamber in front of the uranium layer. The TRIGA was operated at 10 kW for 10 min. Afterward, $\gamma$-measurements of the wires were performed. The 411.8 keV line (95.56 % intensity) of Au-198 was used to determine the activity $A_{Au}$, produced during the irradiation. The thermal neutron flux $\Phi_{n,therm}$ can be calculated by

$$\Phi_{n,therm} = A_{Au}/(\sigma_{Au} N_{Au}(1 - exp(-\lambda_{Au} t))) \tag{3.1}$$

with the cross section of $^{197}$Au $\sigma_{Au}$, the amount of $^{197}$Au $N_{Au}$, the decay constant of $^{198}$Au $\lambda_{Au}$ and the irradiation time $t$. The neutron flux scales linearly with the reactor power, so the calculated number for 10 kW can be extrapolated to the neutron flux at 100 kW (see tab. 3). The measured neutron flux inside the target chamber was used for the calculation of the yield of fission products presented in sec. 2.1.

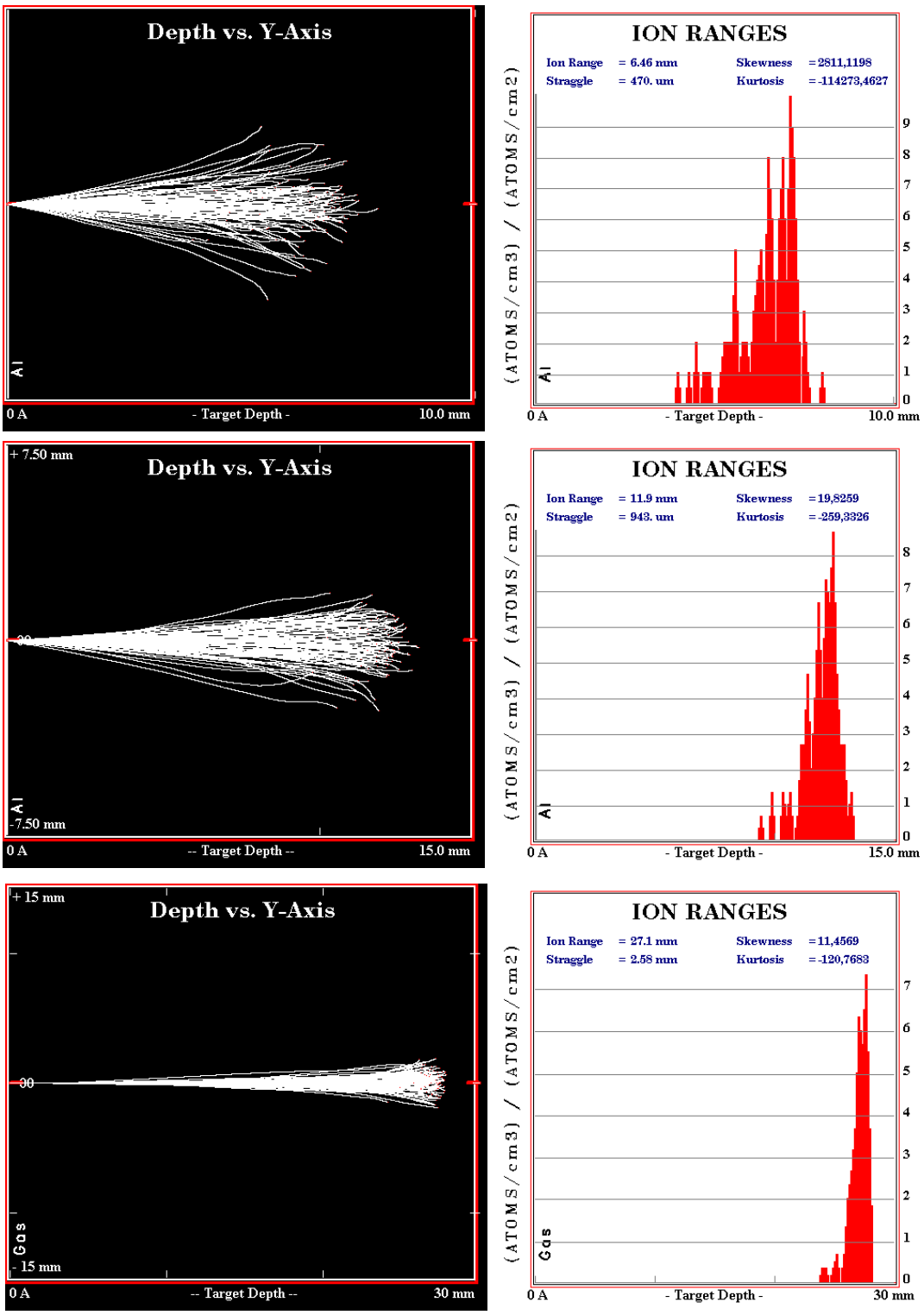


**Figure 3.3:** Simulations of the range of fission products, performed with SRIM2013 [106]. For all simulations 100 $^{91}$Rb ions with an initial kinetic energy of 100 MeV were used. Effects of self-absorption in the $^{235}$U target itself were not taken into account. Top: The ions pass a 13 $\mu$m Al foil before they enter the gas filled volume ($N_2$ at 1 bar). Middle: The ions pass a 10 $\mu$m Al foil. Bottom: The ions are stopped in pure $N_2$ (1 bar), without any Al cover. The result of the simulation in pure nitrogen is in good agreement with the experimental data from Finkle [105].

**Table 3:** Determination of the neutron flux outside and inside the target chamber at beam port A of the TRIGA Mainz research reactor. Wires of an Au-Al-alloy were placed at the two positions and irradiated for 10 min at a reactor power of 10 kW. Afterward, $\gamma$-measurements of the wires were performed and the produced activity $A$ was evaluated. The neutron flux was calculated by eq. 3.1 and multiplied with 10 to get the flux for 100 kW reactor power.

| Position | $m$(Au) / $\mu$g | $A$ / Bq | $\Phi_{n,therm}$ / $\frac{1}{s \cdot cm^2}$ |
|---|---|---|---|
| inside | 6.29 | 35.47 | 9.69E+10 |
| outside | 7.08 | 43.12 | 1.05E+11 |

As soon as the first fission products are caught in the Penning traps and the commissioning phase of the on-line coupling is finished, a scientific measurement campaign can be started. Because a lot of scientifically interesting nuclides are produced in the heavy fission branch, a target without Al cover will be used for this task. Without the additional stopping power of the Al layer, a higher pressure inside the target chamber is needed. The experimental conditions for this purpose have to be determined in future studies.

## 3.2 Gas-jet system

The transport of the fission products from the target chamber through the biological shield of the TRIGA reactor to the ion source is carried out by an aerosol based gas-jet as discussed in sec. 2.2. The two major gas-jet systems used in the frame of this thesis are $N_2$/KCl and $N_2$/$CdI_2$. Figure 3.4 shows a sketch of the gas-jet system. The flow rate of the carrier gas $N_2$ is usually set to 400-1000 ml/min using a flow controller (MKS Instruments Mass-Flo® Controller). The carrier gas passes a tube furnace, containing a ceramic crucible filled with the aerosol material KCl or $CdI_2$. Typical furnace temperatures were 640°C for KCl and 290°C for $CdI_2$.

KCl was mainly used for most test purposes because it provides a high transport efficiency combined with a sufficient skimmer efficiency [62, 107]. But especially in the later beam times $CdI_2$ was used more often because it promises some advantages [55]. The boiling point of $CdI_2$ is only 796°C, which is far below the usual temperatures reached inside the high-temperature surface ion source. This guarantees that most of the $CdI_2$ clusters entering the ion source are evaporated; it also reduces the chance that the skimmer entrance is blocked by macroscopic amounts of aerosol material. The $CdI_2$ molecules are broken up under the conditions inside the ion source and elemental Cd is released. Cd has a boiling point of 765°C, which is also low enough to prevent an

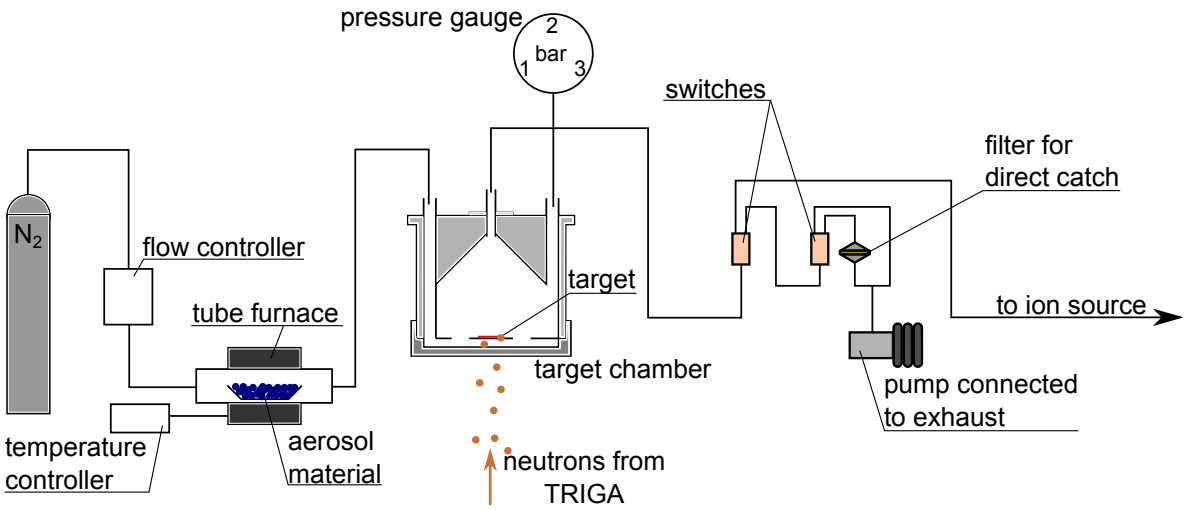


**Figure 3.4:** Sketch of the gas-jet system at TRIGA-SPEC. See text for details.

obstruction of either the entrance or exit of the ion source. On the other hand, the ionization potential of Cd is so high (9.0 eV) that only traces can be ionized by surface ionization processes. This results in a significantly reduced ion background behind the ion source compared to the usage of KCl as aerosol material, which leads to large amounts of $K^+$ ions due to the low ionization potential of K.

The gas-jet enters the target chamber through a capillary with an inner diameter of 4 mm. The capillary of the outlet has an inner diameter of 0.86 mm. All used capillaries are made of PTFE[2]. The capillary guides the gas-jet not directly to the ion source, but passes first two switches. The gas-jet can be directed either to the ion source (through a capillary with an inner diameter of 1.2 mm) or to a direct catch (DC) station, using glass fiber filters (Whatman GF6). The second switch can be used to direct the gas-jet to an exhaust, if it is temporarily not needed for the experiments. The switches and the filter station are installed inside a fume hood (not shown) for safety reasons. To keep the capillary distances as short as possible and to provide the possibility to switch the setup between beam port A and B a mobile fume hood was designed and constructed.

If the gas-jet is directed towards the ion source, it leaves the capillary in front of the skimmer inside a vacuum chamber connected to a roots pump (Edwards EH2600; effective pumping speed 1900 $m^3/h$). Based on the former reports [63], it was verified that the optimal distance between the end of the capillary and the skimmer entrance is 4 mm. In the frame of the diploma thesis of Grund [59], the optimum conditions for the gas-jet with respect to the installation of an aerodynamic lens were investigated. A special

[2]Polytetrafluoroethylene

challenge was the strict space limitation, because only about 400 mm were available for the installation of the lens in front of the skimmer. Anyway, an aerodynamic lens with the required specifications could be constructed and was installed in early 2014 [108].

## 3.3 Common beamline

The common beamline of TRIGA-SPEC contains the online ion source, a dipole magnet mass separator, a radiofrequency quadrupole (RFQ) cooler/buncher and a switchyard which guides the beam to one of the connected experimental branches, TRIGA-LASER or TRIGA-TRAP. For TRIGA-TRAP the ion beam has to be slowed down by a pulsed drift tube (PDT), which is installed inside of the switchyard. Along the beamline a series of detection units for beam characterization are installed. The technical details of the individual stages are briefly presented in the next subsections, the discussion of the beamline characterization, including efficiencies and absolute ion rates of the different stages, is carried out in section 4.

### 3.3.1 High-temperature surface ion source

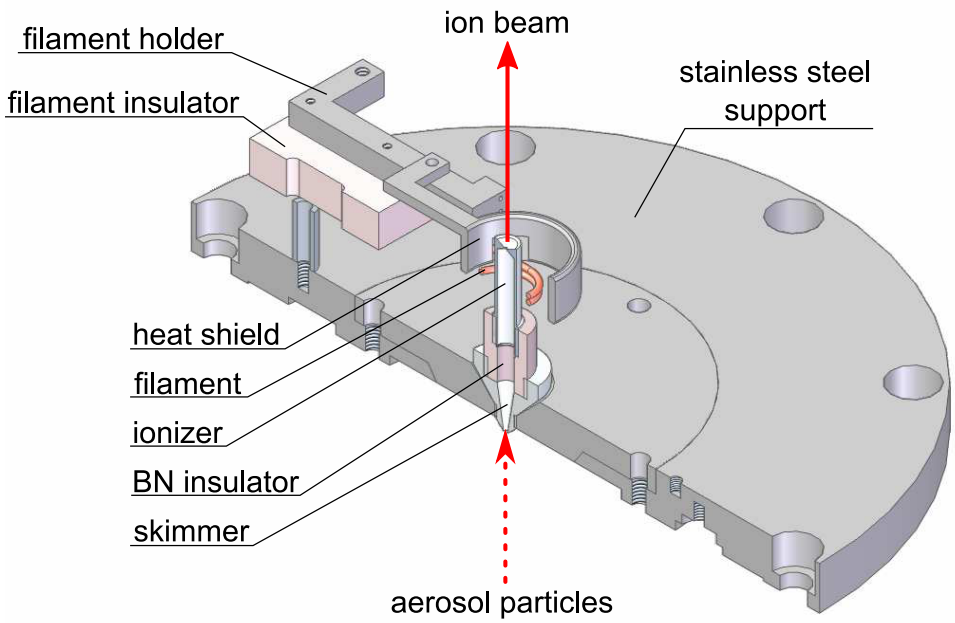


**Figure 3.5:** Cut through a 3D model of the surface ion source. The model of the tungsten filament (red) is simplified.

The high-temperature surface ion source (SIS), designed and commissioned in the frame of this thesis, replaced the former online ion source of TRIGA-SPEC, an electron-

cyclotron-resonance (ECR) ion source [109]. The ECR worked efficiently for the ionization of gaseous species, but it was found that it was not suitable to handle an aerosol based gas-jet. The aerosol particles passed straight through the plasma inside the ECR, but the plasma density was too low to break up the particles and to release the attached fission products. Therefore, another type of ion source was searched for TRIGA-SPEC. The ion source used at the HELIOS setup about 30 years ago fulfilled the desired specifications [62, 63, 107]. The new TRIGA-SPEC SIS is based on this former design. Figure 3.5 shows a 3D model of the ion source and figure 3.6 shows a draft of the ion source region, including the aerodynamic lens and skimmer system, discussed in the previous section.

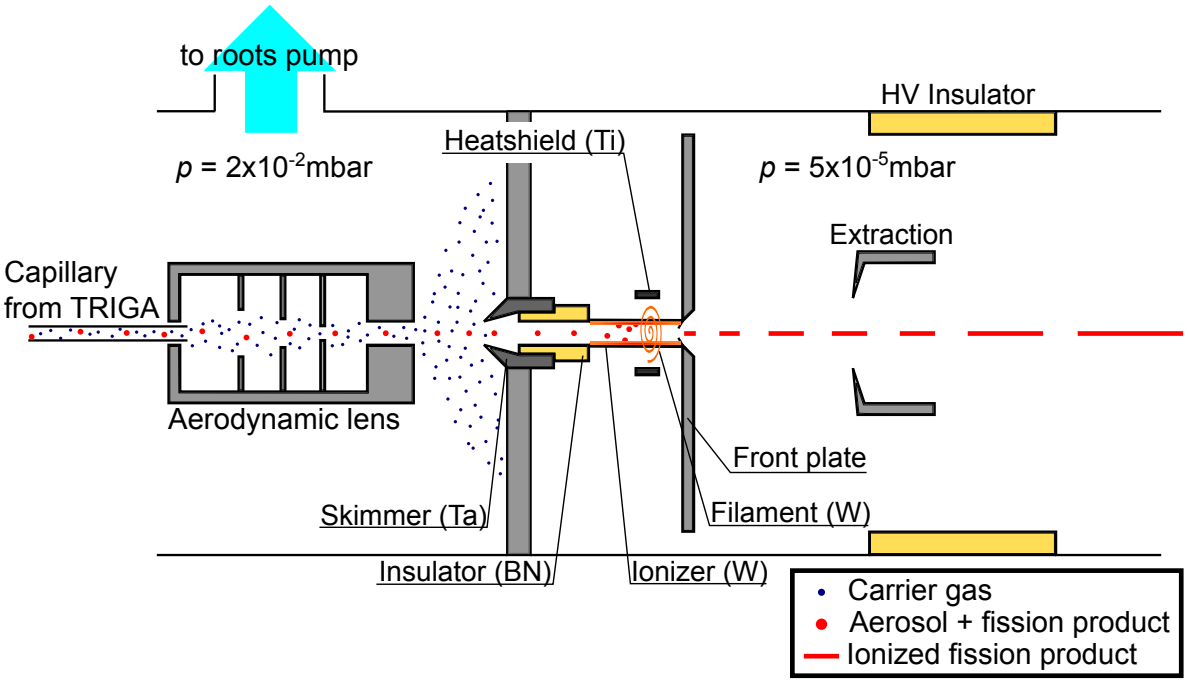


**Figure 3.6:** Sketch of the online ion source region (not to scale). The capillary of the gas-jet system ends inside the aerodynamic lens, which focuses the aerosol particles to a narrow particle beam which enters the ion source through the skimmer. The carrier gas spreads across the volume in front of the skimmer and is pumped away by a roots pump. The tungsten ionizer is heated from a filament by electron bombardment. Aerosol particles are evaporated by contact with the hot surface of the ionizer, releasing the attached fission products, which are subsequently ionized by thermoionization. The ionized material is extracted through the electric field created by an extraction electrode installed behind the ion source. Finally, the ions are accelerated by a high voltage (28 kV) applied to the whole ion source section.

One important advantage of the SIS is the relatively simple construction of the main parts compared to other types of ion sources. The core of the SIS consists of three parts: the conically shaped skimmer made of tantalum, an insulator made of boron nitride

(BN) and the hot cavity made of tungsten. Aerosol particles, loaded with radioactive fission products, enter the SIS through the opening bore (ø 1 mm) of the skimmer, which is the connecting piece between the ion source and the gas-jet section. Its function is explained in detail in sec. 2.2.1.

The BN insulator serves as a thermal shield between the hot tungsten tube and the skimmer to prevent it from getting so hot that the aerosol clusters already break up when they pass the ion source entrance. A direct contact between the two metallic parts would lead to a too high thermal conductivity. In the past, the ion source was also operated in a plasma mode [45, 61, 110] by applying a certain voltage between the skimmer and the tungsten tube. In this case the BN piece was additionally necessary as electric insulator. A future upgrade of the SIS to a similar plasma ion source is optional.

The main part of the SIS is the tungsten tube with an inner diameter of 4 mm and an extraction bore of 0.6 mm. The tube is surrounded by a tungsten filament (ø 0.75 mm). It is resistively heated to high temperatures (typical heating power 30 A @ 12 V), to emit electrons. By applying a voltage between the filament and the tungsten tube (typically 500-600 V), the emitted electrons are accelerated onto the tube, which is thereby heated up to temperatures of about 2000°C. This technique is known as electron bombardment (EB) [111]. The applied EB power and the final temperature of the ion source can be controlled by the electron current, depending on the heating power of the filament, or by the applied EB voltage.

The number of loops of the filament around the tube influences the distribution of the applied power across the tube. A single loop heats the tube very locally and causes a large temperature gradient. Additional loops lead to a more uniform distribution of the heating power, so that the tube is heated more homogeneously. The latter case is in general favored, because the surface area on the inside of the ion source which provides sufficient high temperatures for surface ionization processes is larger. But the number of loops is limited by the space between the filament and the surrounding elements, like the front plate and the heat shield. If the filament gets too close to another part of the ion source, the risk of a short circuit gets higher. Especially when a new filament is built in, the risk of touching a grounded part is high. Due to the bending of the wire, the filament is mechanically stressed. When a new filament is heated up for the first time, the wire becomes softer and the stress can move the filament. It is therefore recommended to heat up a new filament in a separate vacuum chamber prior to the final installation in the ion source, if possible.

The filament is enclosed by a heat shield made of titanium. On the one hand, the

heat shield blocks direct thermal radiation from the ion source. On the other hand, the heat shield is placed on the same potential as the filament and accordingly reduces the attracting electric field which the emitted electrons can sense from the rest of the setup. This way, the amount of heating power dissipated to the vacuum chamber can be reduced. The exit of the ion source is mounted in the bore of the front plate, which has similar functions as the heat shield. It also blocks direct thermal radiation and holds back ions which are produced outside of the hot cavity, like residual gas atoms which can be ionized by the electron bombardment. Without the front plate, these ions could also be accelerated by the high voltage potential and would enter the beamline, causing an unwanted background.

The temperature is the most important parameter which determines the ionization efficiency. Temperature measurements with devices which are in direct contact with the hot surface, e.g. thermocouples, are difficult to realize, because there are not many appropriate materials which can withstand temperatures of more than 2000°C. Fortunately, contactless temperature measurements are possible through a window which is mounted at a free port of the dipole magnet behind the ion source (see sec. 3.3.3) which allows a direct sight on the ion source exit. Temperature measurements were performed first with a disappearing-filament pyrometer, providing a calibration between electron bombardment power and the corresponding ion source temperature. The disadvantage of this type of pyrometer is that it is not suited for an online monitoring of the temperature, because it is located inside a HV cage and has to be read out manually. A more modern IR radiation pyrometer (Sensortherm Metis MI13) has been installed recently, which provides a digital readout, which allows a monitoring of the actual ion source temperature even when the setup is not accessible due to high voltage safety regulations. Results of the temperature measurements are shown in sec. 4.2.

### 3.3.2 Ion optics behind the SIS

The whole SIS arrangement is mounted on a high voltage platform, proven for up to 30 kV. The ion source vacuum chamber is electrically separated from the rest of the beamline, which is biased on ground potential, by a ceramic insulator. Inside of the insulator an extraction electrode is mounted. This is the first focusing element of the beamline and important to reduce the divergence of the ion beam leaving the ion source. The extraction electrode has an entering bore of 8 mm, an inner diameter of 40 mm and is constructed in Pierce geometry [69]. The design of the extraction, especially the way the electrode is mounted inside the insulator, was changed a few times in the course of an

optimization procedure, until the final assembly, shown in fig. 3.7, was constructed. The major challenge was to find a design, which can handle the high temperatures caused by direct irradiation from the source and at the same time to prevent the surface of the insulator to get covered with evaporation residuals from the ion source.

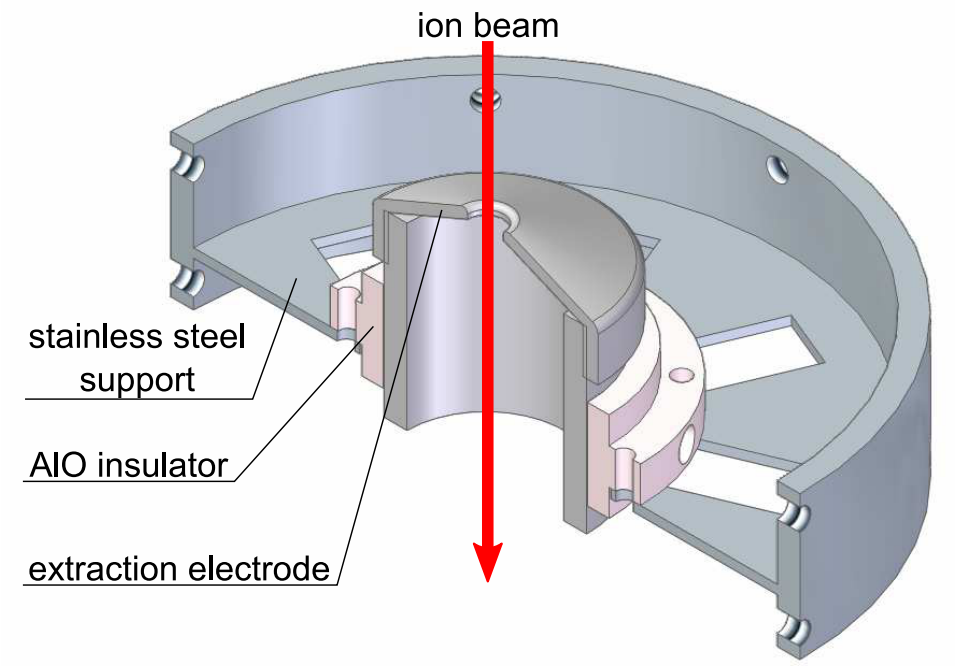


**Figure 3.7:** Cut through a 3D model of the latest version of the extraction electrode behind the surface ion source. The central electrode can be biased to several kV relative to the high voltage potential of the ion source. It is mounted in an AlO insulator. The surrounding metal part for mounting inside the vacuum chamber is equipped with multiple cutaways to increase the pumping cross section.

Fig. 3.8 shows two simulations of the ion beam performed with SIMION 8.0 [112]. The upper figure shows the beam divergence over a distance of 1 m without any focusing electrode inside the insulator. The lower figure shows the influence of an electrode in Pierce geometry at -3 kV (relative to the high voltage) in a distance of 3 cm from the end of the ion source. The accelerating high voltage is set in both cases to 28 kV, as it is usually applied during the experiments. For the simulation, singly positive charged ions with a mass of 91 amu were created in the exit bore of the ion source. As starting conditions a kinetic energy of 0.3 eV (corresponding to a thermal energy of 2000°C) and an opening angle of 90° was assumed.

After the acceleration stage a few ion optical elements are installed (not implemented in the simulation) to control and adjust a possible offset or tilting angle of the ion beam. The first element is a set of three times four electrodes, used as beam deflectors. It is

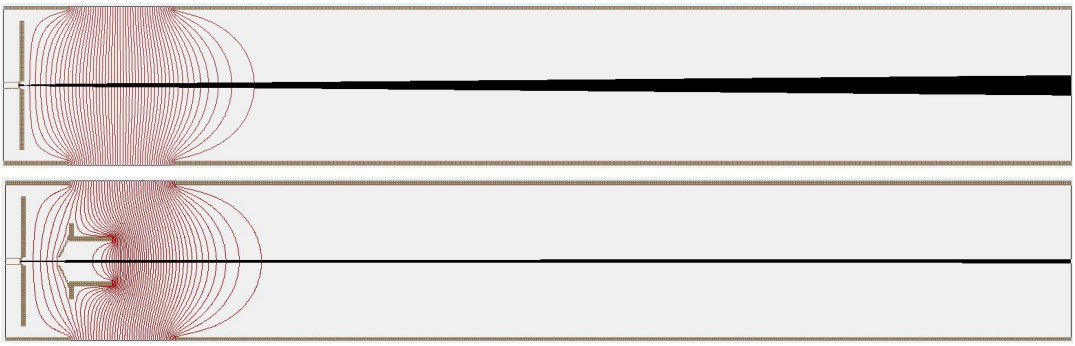

**Figure 3.8:** Simulations with SIMION [112] of the divergence of the ion beam ($^{91}Rb^{+}$) over a distance of 1 m behind the surface ion source. The lines of equal potential are shown in red. In the upper figure the ions are accelerated by a high voltage of 28 kV without an additional electrode. The diameter of the beam is about 20 mm after a distance of 1 m. In the lower figure an extraction electrode in Pierce geometry is added 3 cm behind the ion source and biased to 25 kV. In this case a more parallel ion beam is obtained and the diameter after 1 m is less than 4 mm.

followed by another set of three times four electrodes with alternating polarity, which can be used as focusing quadrupole.

### 3.3.3 Dipole magnet mass separator

After production, deflection and focusing of the ion beam, it is necessary to separate the ion species of interest from other unwanted ions. All ion species, created in the surface ion source, are accelerated by the high voltage potential of $U_{HV} = 28$ kV so that they end up with a certain kinetic energy $E_{kin} = \frac{1}{2}mv^2$. The different ions can be separated depending on their individual mass-to-charge ratio $m/q$ by passing a dipole magnet with a magnetic field $\vec{B}$ and a bending radius $r_0$. Charged particles passing a magnetic field $\vec{B}$ experience the Lorentz force

$$\vec{F}_L = q\vec{v} \times \vec{B} \tag{3.2}$$

By guiding the ion beam through a curved dipole magnet, only ions with the mass-to-charge ratio

$$\frac{m}{q} = \frac{B^2 r_0^2}{2U_{HV}} \tag{3.3}$$

can leave the magnet on a centered trajectory. Particles with a lower $m/q$ are deflected stronger and hit the inner radius of the dipole magnet, while particles with a bigger $m/q$

experience less drag and hit the outer radius.

Assuming that most ions produced by surface ionization are singly positive charged ($q = 1$), the dipole magnet can be interpreted as a pure mass separator. The mass $m$ which is allowed to pass the magnet can be chosen by altering the magnetic field strength $\vec{B}$. By feeding the mass separator continuously with ions, while scanning $\vec{B}$ over a certain range in defined steps, a mass spectrum of the produced ion beam can be recorded behind the separator.

The TRIGA-SPEC dipole magnet is a 90° magnet with a bending radius $r_0 = 500$ mm and a maximum magnetic field strength of $B_0 = 1.12$ T. The highest $m/q$ value for 30 keV ions which can be handled by the separator is 500 u/e.

An important property of a mass separator is the mass resolving power

$$R = \frac{m}{\Delta m} \tag{3.4}$$

with the full-width-at-half-maximum (FWHM) of an observed mass peak $\Delta m$. $R$ characterizes the ability of a mass separator to distinguish two neighboring mass peaks. It depends on the magnet specifications, especially the magnetic field homogeneity, as well as on the shape of the ion beam which enters the separator. The TRIGA-SPEC mass separator has a $R \approx 165$ [113].

In order to improve the mass resolution and to cut off neighboring peaks in the mass spectra, a vertical slit system has been installed directly behind the mass separator. Ions with a $m/q$ close to the selected ratio, which were not separated completely from the central trajectory, can be blocked by these slits [82] (see fig. 3.9).

### 3.3.4 Radiofrequency quadrupole (RFQ) cooler and buncher

Prior to the injection into the two experimental branches of TRIGA-SPEC, the mass separated ion beam is captured in a radiofrequency quadrupole (RFQ) device. The RFQ has two tasks: the emittance of the incoming continuous ion beam shall be reduced, which is called cooling, and the ions from the continuous beam shall be accumulated over a certain period and released as an ion bunch.

The RFQ structure consists of four parallel, segmented rods (see fig. 3.10 left). To each rod, a radiofrequency voltage with amplitude $V_{RF}$, with an alternating phase of $\pi$ between neighboring rods, is applied. Additionally, an electrostatic field gradient is applied along the different segments of the rods. Furthermore, the whole RFQ structure can be filled with buffer gas (He) with typical pressures from $10^{-5}$ to $10^{-2}$ mbar. Ions

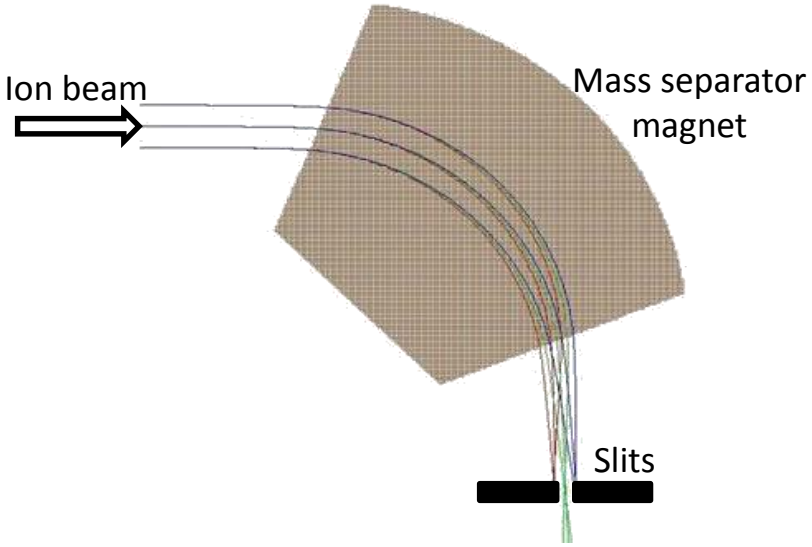


**Figure 3.9:** Simulation of the mass separator magnet used at TRIGA-SPEC [82]. Incoming ions are separated according to their mass-to-charge ratio $m/q$. Only the ions drawn in green leave the magnet on a central trajectory. The other ions are blocked by the slits installed behind the magnet.

which enter the RFQ with a certain kinetic energy lose transversal and longitudinal energy by collisions with the buffer gas. The cooled ions are confined radially by the RF field and are guided towards the end of the RFQ structure by the electrostatic field gradient.

To achieve also accumulation and bunching of the ions, the electrostatic potential of the last segment can be switched fast from a high potential, which forms a potential well where the ions are trapped, to a low potential, which forms a steep slope that ejects the accumulated ions after a certain trapping time. Optionally, the third to last segment can be switched also to a high potential when the ions are ejected, to create an even stronger field gradient (see fig. 3.10 right), so that the length of the released ion bunch can be reduced.

The RFQ is not necessarily operated in the bunching mode, it can still be operated in a continuous mode, to provide a continuous ion beam, which was an useful feature especially in the commissioning phase.

See references [82, 113] for more technical details and first commissioning experiments of the RFQ cooler and buncher.

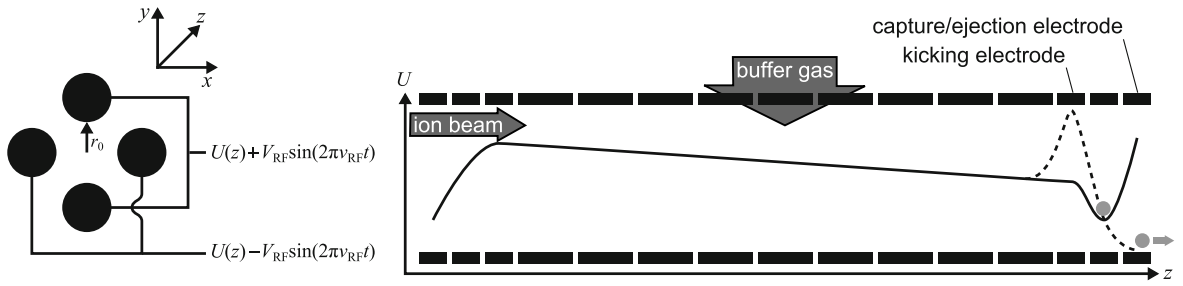


**Figure 3.10:** Sketch of the RFQ cooler/buncher. Left: view of the four rods and their supply voltages along the symmetry axis. Right: side view of the segmented rods of the RFQ structure. The continuous line presents the DC potential along the z-axis during the ion accumulation. For the ejection of the ion bunch, the potential of the last and the third to last segment can be switched, creating the ejection potential represented by the dashed line. Picture taken from [113].

### 3.3.5 Switchyard and pulsed drift tube

The last part of the TRIGA-SPEC common beamline is the switchyard, which directs the ion bunches from the RFQ to one of the three experimental branches. Figure 3.11 shows a 3D model of the switchyard. A pair of vertical electrodes acts as a "pre-kicker", which deflects the ions to one of the three possible switchyard paths. The ions can either go straight towards TRIGA-TRAP or can be deflected towards TRIGA-LASER. The third available port is currently not in use. The respective trajectories are also shown in fig. 3.11.

The electrode assembly inside the switchyard on the flight path towards TRIGA-TRAP forms the pulsed drift tube (PDT). It provides an electrostatic deceleration stage, which is necessary to reduce the kinetic energy of the ion bunch so far that it is possible to catch ions in the Penning traps. The ion bunches leave the RFQ structure with the transport energy of up to 30 keV. In order to achieve stable trapping conditions in the purification trap, it is necessary to reduce this energy to a few tens of eV. Beside some electrodes for pre-focusing and deflection, the main part of the PDT is a 200 mm long electrode which is biased to 1.1 kV below the RFQ-HV potential (e.g. 26.9 kV for a 28 keV ion bunch). While the ion bunch passes the electrode with only 1.1 keV, the electrode's potential is switched fast (in less than 200 ns; corresponding to a flight path of less than 10 mm) by a high-voltage switch (Behlke HTS 301-03-GSM) from the high potential to -1.1 kV, which matches the ground potential of the remaining transport section towards the purification trap. This way the potential energy of the ion bunch is reduced without re-acceleration when leaving the electrode.

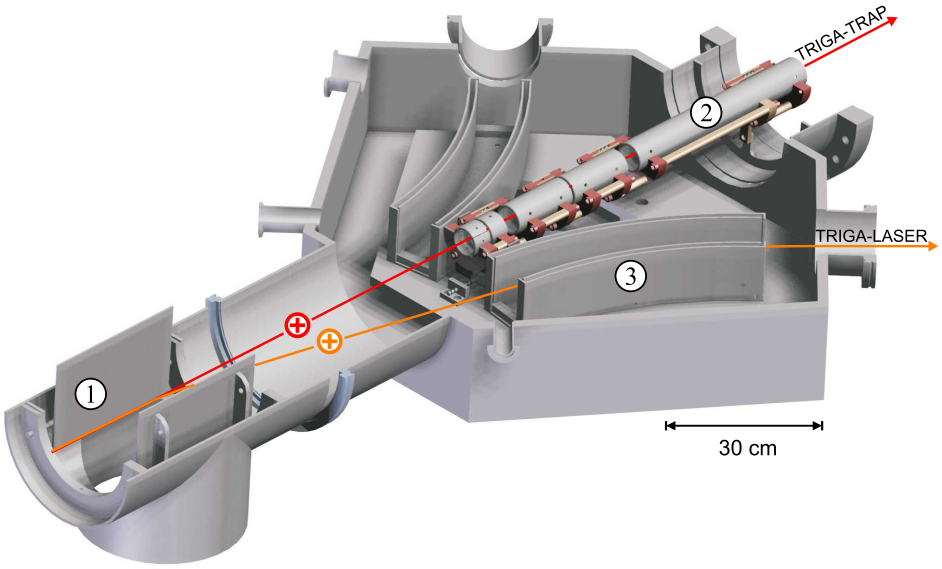


**Figure 3.11:** 3D model of the TRIGA-SPEC switchyard, adapted from [109]. The pre-kicker (1) can let the ion beam go straight into the pulsed drift tube (PDT) and the TRIGA-TRAP beamline (2) or it can deflect the ions to the main deflector (3), which guides the beam to TRIGA-LASER.

Design and commissioning of the PDT was done in the frame of the theses of Smorra [109] and Beyer [82]. First tests with ion bunches of stable nuclides confirmed the fundamental operability of the device. But it was also found that the overall efficiency of the PDT has to be improved in the future. The deceleration process itself generates some experimental problems. The transverse emittance of the ion bunch increases during the deceleration, so that the slowed down ion bunch can be cut off at orifices along the beamline more easily than a 30 keV ion bunch. In addition, the low energy bunch is much more susceptible to electrostatic stray fields and deflectors. Thereby, it is much harder to guide a decelerated ion bunch without significant losses towards the purification trap than a high energy bunch.

### 3.3.6 Detection units and beam characterization

At different positions of the common beamline certain detection units have been installed for beam characterization. The most important positions are between the dipole magnet and the RFQ and directly behind the RFQ (see fig. 3.1). At these positions two detector assemblies, each equipped with a Faraday cup (FC) and a MCP with phosphor screen, are installed and used for ion beam optimization. The detectors are mounted on motorized feedthroughs, so that the desired detector can be moved remotely in or out of the ion beam. Beam characterization in front of the dipole magnet is difficult because

all incoming ions from the ion source are detected equally without any separation, so that no discrimination between the ions of interest and unwanted species is possible.

Important beam parameters which can be investigated are the ion current for continuous ion beams, the number of ions/bunch for ion bunches, the beam size and shape and the amount of ionized fission products from the TRIGA reactor.

The ion beam current is the most fundamental property of an ion beam and can be measured with an amperemeter connected to a Faraday cup. Especially behind the separator magnet the ion current provides important information to identify the present ion species and to calibrate the recorded mass spectrum with known signals. A Faraday cup consists of an electrically insulated metal cup connected to ground potential through a calibrated resistor. An amperemeter measures the charge draining through the resistor. It can be assumed that most of the ions produced by surface ionization processes are singly positive charged, carrying one elementary charge $e = 1.602 \cdot 10^{-19}$ C, so that a detected current of 1 A corresponds to

$$1A = 1\frac{C}{s} = 6.242 \cdot 10^{18}\frac{e}{s} = 6.242 \cdot 10^{18}\text{ions/s}. \tag{3.5}$$

Ions with 28 keV kinetic energy can release electrons from the metal cup when they hit the surface. These "missing" negative charges on the cup would increase the amount of measured positive charges. But these secondary electrons can be eliminated by a negative-biased "suppressor" electrode, which pushes all emitted electrons back to the cup, so that the influence of this effect can be neglected. A Faraday cup is an insensitive device, so there is no problem to detect even high intensity ion beams of several hundred nA or higher. The lower detection limit is mainly given by the connected read-out device and is typically in the range of a few pA.

A Faraday Cup can be also used to determine the number of ions within a bunch of ions ejected from the RFQ. The signal of a calibrated charge amplifier, connected to the readout electronics of the FC, can be displayed with an oscilloscope. The peak voltage $U_{max}$ of the observed signal scales linearly with the size of an ion bunch.

For low intensity ion beams with 1 pA or lower, microchannel plate (MCP) detectors are suited. The MCP consists of a highly resistive plate with a thickness of about 2 mm which is penetrated by channels with a typical diameter of about 10 $\mu$m, spaced apart by approximately 15 $\mu$m. The channels are ordered parallel to each other and are slightly tilted against the surface normal at a typical angle of 8°. Each microchannel serves as an electron multiplier. The surfaces are metal coated and act as front and

rear electrodes. An incoming particle which hits the wall of one micro-channel produces secondary electrons. These electrons are accelerated along the channel by an applied voltage, typically in the range of 1000-1800 V. Because of the small tilting angle the electrons hit the wall of the channel multiple times, producing additional electrons and causing a cascade. The amplification of the original signal can reach several orders of magnitude. This way, a MCP can even reach single ion sensitivity. After each electron cascade, the microchannel needs some time to recover, the so-called dead time, before the next signal can be detected. A too high current of more than a few pA on the MCP has to be avoided, because a continuous discharge between the electrodes can damage the device [114].

Beside the possibility to detect even low ion currents, a MCP detector combined with an additional phosphor screen provides the option to visualize the shape of the beam. The phosphor screen is attached behind the rear electrode of the MCP. By applying a positive potential to the phosphor screen, typically about 1200 V, the electron cascade leaving a channel of the MCP is accelerated further onto the phosphor screen. Every electron hitting the surface stimulates the phosphor layer to emit several fluorescence photons. This way, a picture of the ion beam's intensity distribution is generated which can be observed by a CCD camera outside the vacuum chamber via a mirror positioned behind the phosphor screen.

A typical beam optimization procedure includes the adjustment of the extraction electrode, the 12 deflectors and the 12 quadrupole electrodes behind the ion source for a maximum signal intensity on the FC and simultaneously a small, in the best case point-shaped, beam profile. Especially when the ion source was removed and reinstalled, a readjustment of the different settings is usually necessary.

The detection and confirmation of radioactive ions is a special challenge, because neither a Faraday cup nor a MCP detector can distinguish between radioactive and stable species. The absolute amount of produced fission products is in the range of about $10^7$ atoms/s per isobar. Even if a 100% transport and ionization efficiency would be assumed, this amount would only result in an ion current of about 1 pA. Taking the typical efficiencies of the different stages into account, the ion current can be expected to be in the range of only a few fA or less per isobar. So, there is no chance to see a signal originating from ionized fission products with a FC. A MCP detector has in principle the necessary sensitivity to detect those small ion currents. In practice it is not so easy, because by scanning for ion currents in the range of a few fA also traces of different ionized contamination, e.g. ionized surface elements of the ion source itself or

molecular species originating from impurities of the carrier gas, get measured. A good way to ensure only the detection of radioactive ions is a $\gamma$-measurement, which is not disturbed by contamination of stable nuclides. Therefore, Al catcher foils were mounted on the movable detector feedthroughs. After checking the beam parameters with stable ion species observed with the FC and the MCP detector, the separator magnet was set to a mass number where fission products with convenient half-lives, production rates and of elements suitable for surface ionization were expected and the Al foil was moved into the beam. After a certain accumulation time, the collection was stopped and the Al foil was removed from the vacuum chamber. Stopping of the pumps, breaking of the vacuum and transport of the catcher foil to the $\gamma$-detector results in an unavoidable delay of 15-20 minutes between end of collection and beginning of measurement, which makes it impossible to measure nuclides with half-lives of a few minutes or less. But by choosing an appropriate measuring time, long-lived nuclides implanted into the Al foil or related daughter nuclides can be measured. With the known detector efficiency, $\gamma$-intensities, half-lives and timings it is possible to calculate the amount of radioactive nuclides which have been implanted during the collection. The main disadvantage of this method is that it is an offline detection technique. After each collection it is necessary to cut off the ion beam and to open the vacuum chamber somewhere, which makes the whole procedure very time consuming.

All $\gamma$-measurements mentioned in this thesis were recorded with p-type coaxial Ge-detectors and the software "Genie2000" [115]. Calibration of the individual detector efficiencies were performed with a QCY48-$\gamma$-standard[3].

## 3.4 TRIGA-TRAP

This section presents the experimental setup of TRIGA-TRAP as shown schematically in fig. 3.12. The decelerated online ion beam from the PDT would enter the TRIGA-TRAP branch from the left side in the drawing.

Beside the connection to the online surface ion source, TRIGA-TRAP is additionally equipped with an offline laser ablation ion source. The ion beam of one of the ion sources is guided to the double Penning-trap mass spectrometer, located inside the 7 T superconducting magnet. The stage behind the magnet is the time-of-flight section, which is used for the cyclotron frequency measurements using the TOF-ICR technique.

[3]contains certified amounts of $^{241}$Am, $^{109}$Cd, $^{57}$Co, $^{139}$Ce, $^{203}$Hg, $^{113}$Sn, $^{85}$Sr, $^{137}$Cs, $^{88}$Y and $^{60}$Co

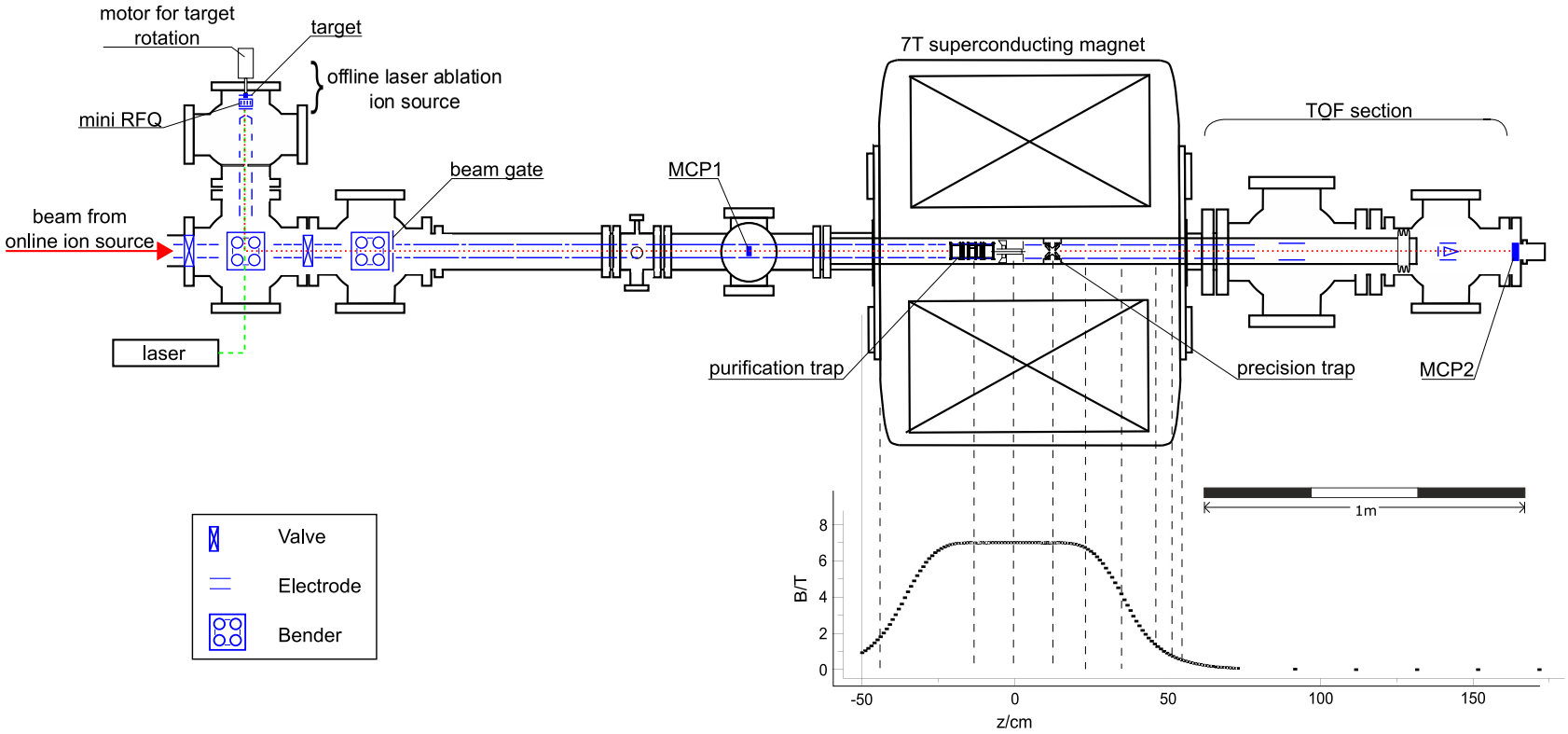


**Figure 3.12:** Sketch of the experimental setup of TRIGA-TRAP. In the case of online operation, the ion beam from the surface ion source enters the setup from the left. For offline operation, the laser ablation ion source is used. The dashed, green line shows the path of the laser beam. The rotatable target is part of a mini-RFQ structure. The produced ions (red dotted line) are guided towards the Penning trap, located inside a 7 T superconducting magnet, by an electrostatic 90° bender. Two MCP detectors are available: MCP1 directly in front of the superconducting magnet and MCP2 at the end of the TOF section, used for the TOF-ICR measurement technique. The graph below the magnet shows the strength of the magnetic field along the relevant parts of the beam line.

### 3.4.1 Laser ablation ion source and mini-RFQ

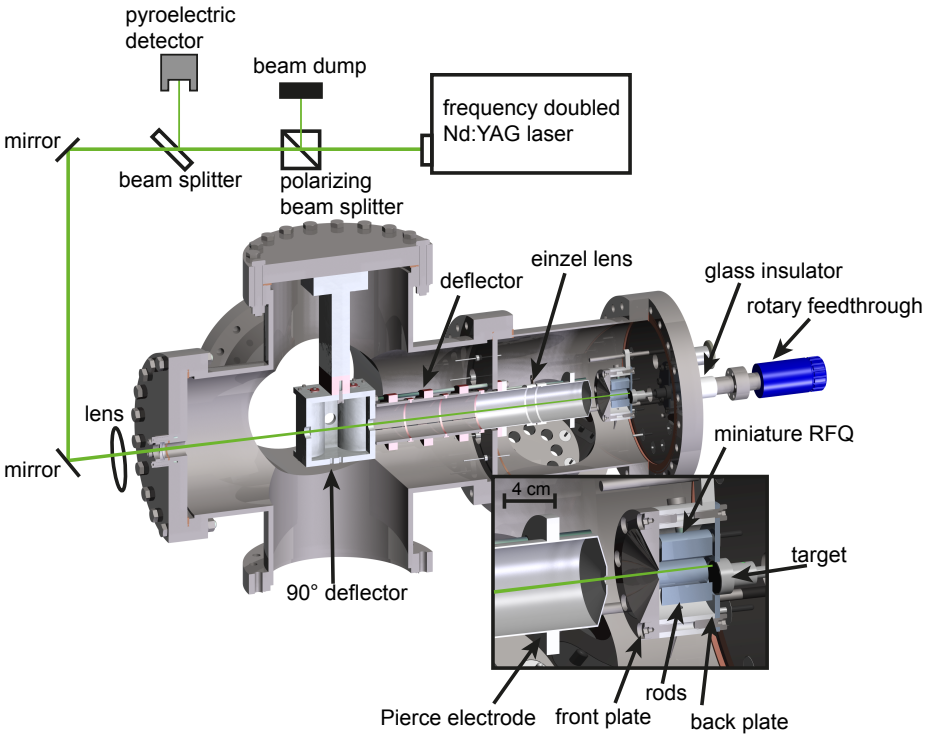


**Figure 3.13:** 3D model of the laser ablation ion source, including the mini-RFQ structure. Picture taken from [17].

The offline laser ablation ion source is used for two purposes: the production of carbon cluster ions for the magnetic field calibration and to provide TRIGA-TRAP with ions of stable or long-living nuclides. The laser ablation source is operational since 2008 [99] and has been upgraded in the meanwhile with a miniature radiofrequency quadrupole (mini-RFQ) [103], to improve the ion yield and to reduce the energy distribution of the produced ions. A 3D sketch of the source is shown in fig. 3.13.

Core piece of the ion source is a frequency-doubled Nd:YAG laser, working with a wavelength of 532 nm, a pulse length of 5 ns and a maximum energy of 12 mJ per pulse. The laser energy can be weakened by a tunable attenuator, so that the final energy deposited on the target is typically in the range between 0.05 mJ and 0.5 mJ.

The target consists of a circular shaped plate of a glass-like carbon modification (Sigradur®[4], 14 mm diameter, 2 mm thickness). This material is well suited to produce the necessary carbon cluster ions by the laser ablation process. In the case that other stable or long-living material has to be ionized (like the transuranium nuclides

[4]Sigradur is a trade name of HTW Hochtemperatur-Werkstoffe GmbH.

discussed in sec. 5), drops (5-10 $\mu$L) of a solution (typically diluted nitric acid) of the desired material are evaporated on top of the Sigradur target. The laser is hitting the Sigradur disk off-center, so that it is possible by rotation of the disk to select whether carbon or the nuclide of interest shall be ionized.

The evaporation of the drops on the surface lead usually to a ring-shaped distribution on the Sigradur. The laser is fixed to a certain radius from which material on the target can be ionized, so that often more than 90 % of the deposited material remains unused (measured by $\alpha$-spectroscopy of Am-241 and Cf-249). It was tried to find an improved target preparation technique, so that a larger fraction of the material can be used or rather the total amount of necessary material can be reduced. A promising method is the application of superhydrophobic surfaces on the Sigradur targets prior to the placement of the aqueous drops, which results in significantly smaller spots of the deposited material [116]. The main disadvantage up to now is that it is technically impossible to move either the laser spot nor the target holder, so that it is not guaranteed that the small spots are hit at all, because the reproducibility of the target placement is limited. An upgrade of the target holder to solve this problem is planned for the near future.

Another idea to reduce the necessary amount of target material was the installation of a mini-RFQ structure. The fundamental working principle is the same as for the RFQ cooler/buncher of the common beamline (see sec. 3.3.4). The ions produced by the laser ablation are confined by appropriate DC- and RF-potentials in a small volume, flushed with a certain amount of helium buffer gas ($2 \cdot 10^{-5}$ mbar l/s). By interactions with the buffer gas, the geometric and energetic distribution of the ions can be reduced, so that the subsequent ejection and the transport towards the Penning traps proceeds with higher efficiency [103].

The ion bunch, leaving the mini-RFQ with an ion energy of 1 keV, passes a 90° electrostatic quadrupole bender, which guides the ions towards the traps. In the case of online measurements, the bender is switched off, so that the ion bunch from the PDT can get straight through.

Fig. 3.14 shows a time-of-flight spectrum of produced carbon cluster ions at the MCP detector in front of the Penning traps (MCP1 in fig. 3.12). Without the mini-RFQ it was not possible to resolve the individual signals, which is, however, necessary to distinguish between the different clusters. By applying different DC- and RF-potentials, it is additionally possible to select the carbon cluster size distribution which is accepted by the mini-RFQ, so that a pre-selection of the desired ion species is achieved [24].

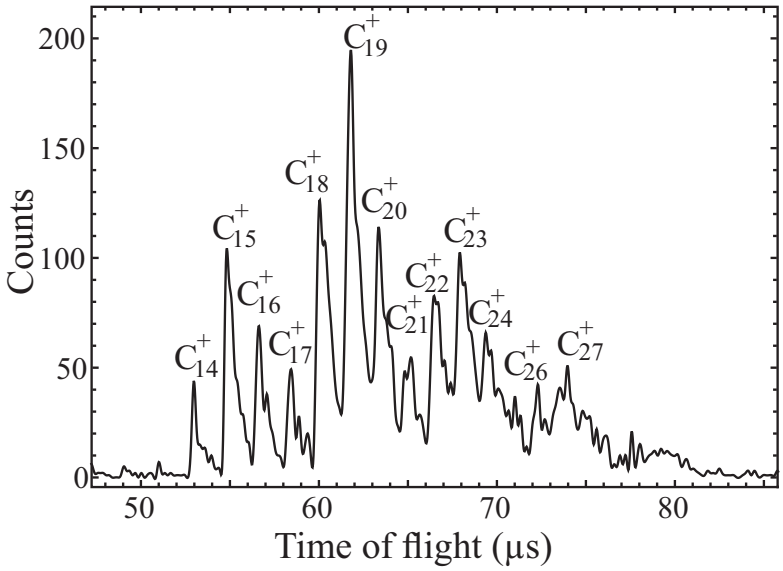


**Figure 3.14:** TOF spectrum of carbon cluster ions recorded at MCP1. The settings of the mini-RFQ have been optimized for the production of heavier clusters around $C_{20}^+$ [24].

Anyway, if the whole bunch of carbon clusters, as shown in fig. 3.14, would reach the Penning traps, an overload of the purification trap with too many unwanted ions would be unavoidable, so that a specific selection of the ions of interest would be difficult. For this purpose a beamgate is installed behind the 90° bender. For the time being, the beamgate consists only of a fine wire mesh, which is biased on a high voltage potential that blocks all incoming ions. The beamgate is only opened for a few microseconds after a certain waiting time, corresponding to the time of flight of the desired mass range, so that a certain bunch of ions can pass. This simple beamgate will be upgraded in the near future to a Bradbury-Nielsen gate.

### 3.4.2 Double Penning-trap setup TRIGA-TRAP

TRIGA-TRAP contains two Penning traps, referred to as "purification trap" and "precision trap", located inside a 7 T superconducting magnet. The cylindrical purification trap is used for mass-selective buffer-gas cooling (see sec. 2.4.2), while the hyperbolic precision trap serves as tool for the precise measurement of the cyclotron frequency (see sec. 2.4.3). Both traps are equipped with correction electrodes, adjusted prior to the actual measurement campaign, to achieve harmonic trapping potentials. A 3D sketch of the Penning traps is shown in fig. 3.15.

Both traps are separated by a pumping barrier with an inner diameter of 1.5 mm

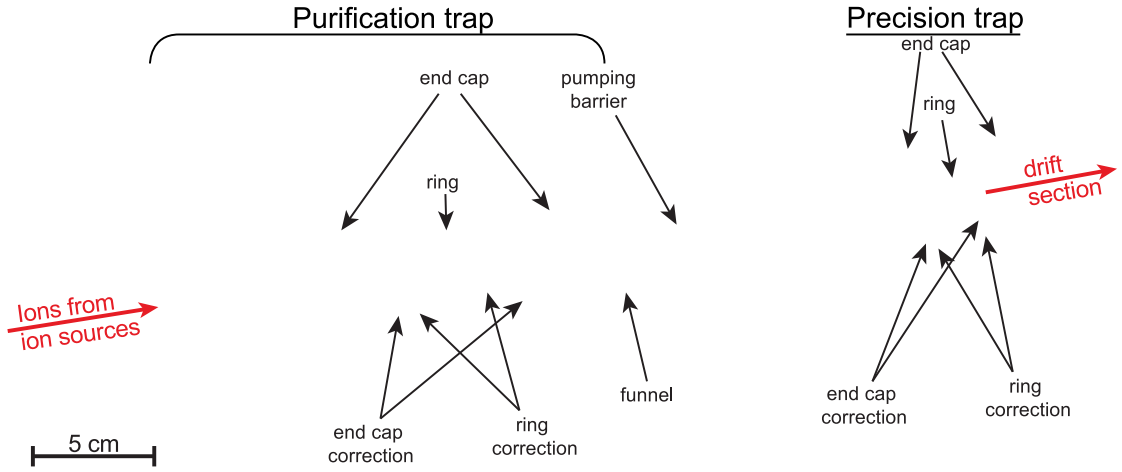


**Figure 3.15:** 3D model of the double Penning trap system of TRIGA-TRAP, adapted from [17]. The cylindrical structure on the left is the purification trap, the hyperbolic assembly on the right is the precision trap. Both traps are connected by the pumping barrier, which has an inner diameter of only 1.5 mm. Only ions which are centered in the purification trap can reach the precision trap.

and a length of 50 mm. It serves two purposes: only cooled and centered ions from the purification trap can pass the narrow tube, and the barrier ensures a low pressure in the precision trap, although the purification trap is loaded with a helium gas flow of $2 \cdot 10^{-5}$ mbar l/s.

### 3.4.3 Time-of-flight section and ion detection

The time-of-flight section behind the superconducting magnet is needed for the TOF-ICR detection technique and ends at an MCP detector, which was recently replaced by a position-sensitive delay line detector. The position-sensitive detector is needed for the future development of the PI-ICR technique, but it was used as a pure ion counter during the measurements presented in this thesis, just as a conventional MCP detector. The detection efficiency is assumed to be 35 %.

The time-of-flight section contains several electrodes, acting as ion optical elements, to ensure that the ions ejected from the precision trap reach the active zone of the detector. A special challenge for the ion optics is the fact that slow (non-excited) ions shall be guided with the same efficiency as fast (excited) ions. Usually, faster ions are easier to transport than slower ions, which react more sensitively to electromagnetic disturbances along the drift section. If this is the case, one can observe some kind of count-rate resonance, meaning that the number of detected ions depends on the excitation frequency. This results in lower statistics for the non-excited ions, reducing

the overall accuracy of the fit to the data points. It has been investigated that a crucial parameter to avoid this behavior is the ejection phase. By adding a certain waiting time in the range of a few hundred microseconds between the excitation and the ejection, the non-excited ions can be ejected from a specific point of their radial motion, where the transport efficiency to the detector is significantly higher than from other positions. The waiting time was scanned routinely, so that in general count-rate effects could be avoided during the presented measurements. For the implementation of the PI-ICR technique, the reason of this phase dependency of the count rate has to be identified and removed, because otherwise it will not be possible to monitor the magnetron motion with the position-sensitive detector [94].

### 3.4.4 Measurement and evaluation procedure

The determination of the mass of an atom is carried out by the alternating measurement of its cyclotron frequency and the cyclotron frequency of a carbon cluster reference ion (see sec. 2.4.3 and 2.4.4) [24, 85, 100]. From these frequencies a mean frequency ratio $r$ can be obtained, which is used to calculate the atomic mass $m$ of the ion of interest by applying eq. 2.23. The mass excess $ME$, defined as the difference between a nuclide's mass and the mass number in atomic mass units, in units of energy is a more common way to present mass data in literature. It has the advantage, that the relative stability of a nucleus can be seen more easily, because a negative (positive) value corresponds to a nucleus which has more (less) binding energy than $^{12}$C.

$$ME = (m - A) \cdot 931.4940023 \text{ MeV/u} \tag{3.6}$$

In eq. 3.6, $A$ denotes the mass number of the measured species. In the case that the frequency ratio of the oxide ion was determined, the mass excess $ME(^{16}\text{O})$ of $^{16}$O has to be subtracted to get the final $ME$ value of the elemental atom of interest. $ME(^{16}\text{O})$ is known in literature [16] with high precision[5], so that no additional uncertainty is introduced by the measurement of the oxide species.

The time frame of a complete measurement cycle for ions produced by the laser ablation ion source, like the transuranium nuclides discussed in sec. 5, is depicted in fig. 3.16 and will be explained briefly.

The cycle starts with the ion production by a 5 ns laser pulse (1). The generated ions are confined in the mini-RFQ structure for 7 ms (2). After the cooling process in

[5] -4737.00137(16) keV

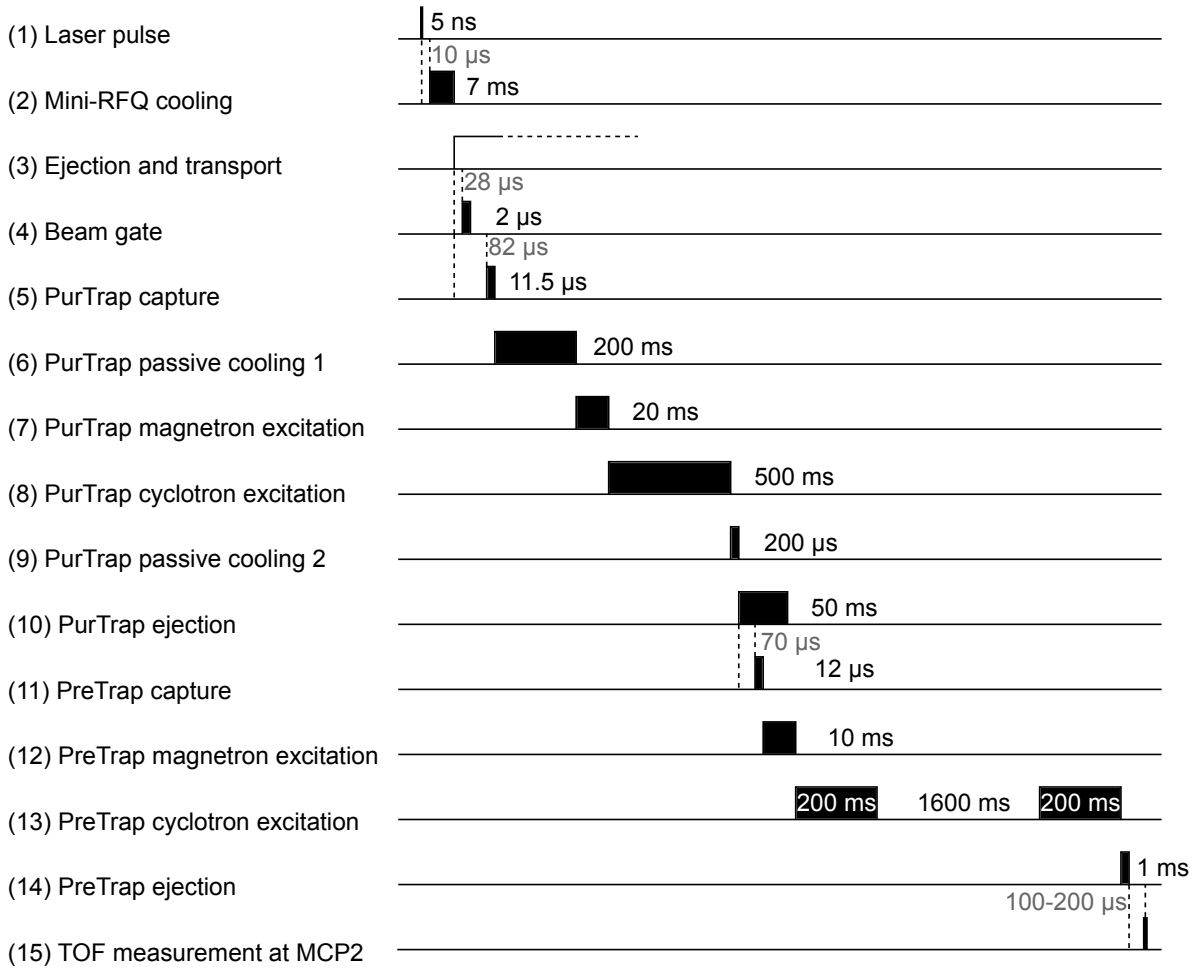


**Figure 3.16:** Sketch of the timing of a complete measurement cycle for ions produced with the laser ablation ion source. The gray written values represents waiting times and are usually mass dependent. The given values are for A = 264 (e.g. $C_{22}^{+}$). The length of the depicted time spans are not to scale.

the mini-RFQ, the ion bunch is ejected by lowering the potential of the front electrode (3) and transported towards the Penning traps. The ions pass the beam gate after about 28 $\mu$s (for A = 264), which is opened for 2 $\mu$s (4). The time of flight to the first trap depends on the mass of the ions and is about 82 $\mu$s for A = 264. When the ion bunch arrives at the purification trap, it is opened for 11.5 $\mu$s by lowering the potential of one of the end caps and the corresponding correction electrode (5). The ions are stored in the purification trap for 200 ms (passive cooling 1), at which the axial and the initial cyclotron motion are cooled by interaction with the He buffer gas (6). Afterward, the buffer gas cooling as described in sec. 2.4.2 is applied, starting with a 20 ms dipolar excitation to establish a certain magnetron radius for all trapped ion species (7), followed by a 500 ms quadrupolar excitation at the cyclotron frequency of the ion species of interest (8). After an additional waiting time of 200 $\mu$s (passive cooling 2), used to cool any residual cyclotron motion (9), the cooled and centered ions are ejected from the purification trap (10) and captured after a time of flight of about 70 $\mu$s (for A = 264) in the precision trap, which is opened for 12 $\mu$s (11). In the precision trap, the actual cyclotron frequency measurement is performed as described in sec. 2.4.3, starting with a 10 ms dipolar excitation to increase the initial magnetron motion (12) and the subsequent conversion of the magnetron to the reduced cyclotron motion by a 2 s quadrupolar excitation (13). For all measurements presented in this thesis a Ramsey-excitation scheme was applied, splitting the total excitation time of 2 s into two pulses of 200 ms, separated by a waiting time of 1.6 s. After the conversion, the ions are ejected from the trap (14) and transported through the time-of-flight section towards the detector, which records the time of flight (15).

After each cycle, the excitation frequency for the conversion (12) is changed slightly around the expected free cyclotron frequency $\omega_c$, so that finally a time-of-flight spectrum is obtained. For the presented measurements the frequency was altered in steps of 0.05 Hz. One complete scan of the considered frequency frame included 41 steps. To gain a proper time-of-flight spectrum with sufficient statistics, several hundred ions in sum have to be recorded. Usually 20-30 scans, corresponding to a measurement time of 1-1.5 h, are necessary to get this number of ions, depending on the actual count rate. The count rate can be mainly influenced by adjusting the laser attenuator or the amplitude of the radio-frequency potential of the mini-RFQ. Either a too low or a too high count rate extend the necessary number of scans, because a too high count rate means that multiple ions are trapped simultaneously in the precision trap. The electrostatic repulsion of multiple positive charges can result in a frequency shift [117,

118], so that for the evaluation a maximum of 5 ions per step is considered.

The measurement procedure was controlled by the software "MM6" and the fits for the cyclotron frequency determination were done with the software "EVA 6.1.4.0".

Fig. 3.17 shows a typical time-of-flight resonance for $C_{22}^{+}$, obtained after 20 scans (788 ions in total). The individual data points represents the mean time of flight for all ions recorded at the same frequency. The theoretical line shape (red line) [88] is fitted to the data using a least-squares determination. The cyclotron frequency extracted from the fit is 407120.010(1) Hz. The pronouncement of the side bands by applying the Ramsey method makes it impossible to determine which minimum corresponds to the actual free cyclotron frequency. Therefore, scans with continuous excitation were performed for every new ion species and routinely if some maintenance at the magnet was necessary (like refilling the liquid nitrogen or helium tanks), to ensure that the correct minimum was fitted by the evaluation of the Ramsey spectra.

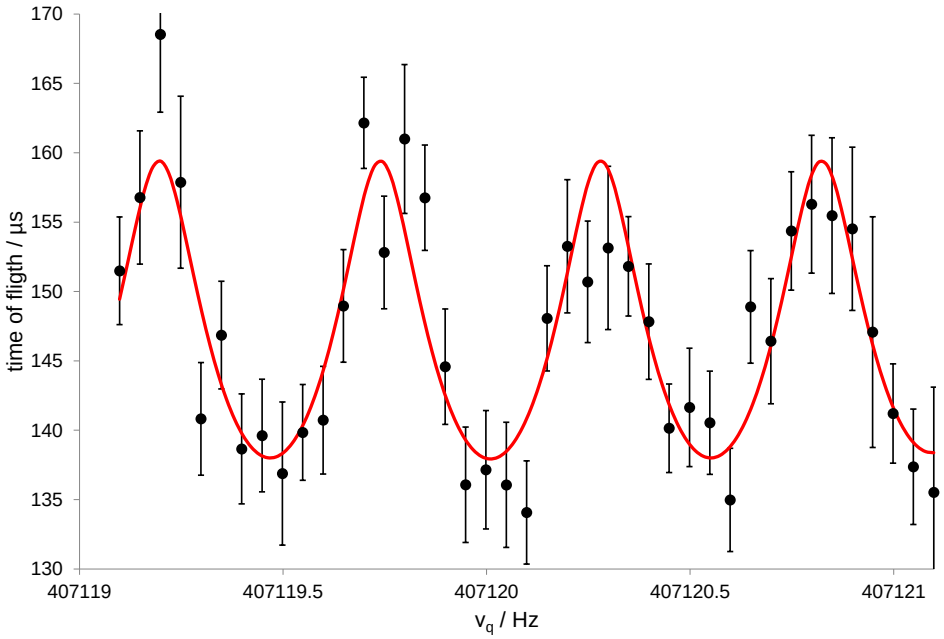


**Figure 3.17:** Time-of-flight ion cyclotron resonance of $C_{22}^{+}$. A Ramsey scheme with a total time of 2 s was used for the excitation of the ions. The time of flight of the ions is shown as a function of the excitation frequency $\nu_q$. The theoretical line shape is fitted to the data points with a least-squares method (red line).

For the evaluation the frequency ratio $r_i = \omega_{c,ref}/\omega_c$ between the reference cluster and the ion of interest is needed. The two frequencies cannot be measured at the same time, so the reference frequency is measured before and after the ion of interest and then linearly interpolated to the center time of the measurement of $\omega_c$. The mean frequency

ratio $r$ is then calculated as the error weighted mean

$$r = \frac{\sum_i \frac{r_i}{\sigma_i^2}}{\sum_i \sigma_i^{-2}} \tag{3.7}$$

with the statistical uncertainty $\sigma_i$, including non-linear fluctuations of the magnetic field [86, 100]. Beside the statistical fluctuations, the uncertainty $\delta r$ of $r$ includes also the uncertainty based on the frequency shift which may arise from the mass difference between the ion of interest and the reference (see eq. 2.24). The magnitude of this effect will be discussed in sec. 5.1.

Additional sources for systematic uncertainty are fluctuations of the trap tube temperature or of the pressure inside the liquid helium Dewar of the superconducting magnet. The effect of these fluctuations has been studied in the past [17, 86] and appropriate stabilization systems have been installed. At least for the accuracy aimed at in the measurements presented in sec. 5, the influence of these fluctuations is negligible in the evaluation.

To exclude frequency shifts caused by ion-ion interactions, single ion events are preferred during a measurement cycle. Because of fluctuations of the ion production rate, it is unavoidable to get also several multiple ion events during a cyclotron frequency measurement. It would be possible to exclude all of these events in the evaluation procedure, but this is not favored, because this way the number of detected ions during a certain measurement time would be very limited, leading to an increased statistical uncertainty, according to eq. 2.22. On the other hand, a longer measurement time would increase the uncertainty caused by the magnetic field drift. So, in practice, all events with 1 to 5 detected ions per laser pulse are used for the evaluation.

# 4 Status of the online coupling of TRIGA-SPEC

## 4.1 Gas-jet transport

Although the influence of the oven temperature and gas flow rate on a gas-jet based transport system are described in the literature, it was necessary to identify the optimal conditions for the specific setup used at TRIGA-SPEC. The gas flow rate and the temperature used for the aerosol formation were varied during some reactor beamtimes, so that the relative transport efficiency of the fission products could be recorded. The gas-jet was guided to the direct catch (DC) station and after a certain collection and waiting time a $\gamma$-measurement of the filter was carried out. $\gamma$-lines of Tc-101 and Y-94 were primarily used for the investigations. These two nuclides have been chosen because of their high production rates, intense $\gamma$-lines and appropriate half-lives. Mother-daughter-relations, which can complicate the comparability of different catches, especially in the case of Tc-101, can be neglected, if the collection, waiting and measuring time is kept constant for all compared measurements. The early investigations on the optimal conditions for KCl and $CdI_2$ were done using a Cf-249 instead of the usual U-235 target in the TRIGA reactor. The maximum production rate of the light branch of fission products is thereby shifted to heavier masses, so that for those measurements also Tc-104 was taken into account, because it provided one of the most intense $\gamma$-lines in the spectra. The error bars in the following figures are calculated from the statistical errors of the $\gamma$-measurements.

### 4.1.1 Influence of oven temperature

To find the optimal oven temperature for the production of KCl particles, suited for fission product transport, the temperature was varied from 580-680°C at a constant $N_2$ gas flow rate of 1500 ml/min. Figure 4.1 shows the relative transport efficiency of Tc-101, Tc-104 and Y-94. Within the individual deviations of the observed nuclides, all three distributions show a maximum in the range of 630±10°C.

The investigation was repeated later in the range from 620-660°C for a lower gas flow rate of only 400 ml/min. This reduced gas flow was necessary with respect to the later installed aerodynamic lens. The temperature dependence of the transport efficiency changes for higher temperatures, as fig. 4.2 shows. Although there is still a maximum around 630°C, the efficiency does not turn downward as strongly as at higher flow rate. Nevertheless, the operating temperature was kept at 630-640°C, because it was observed

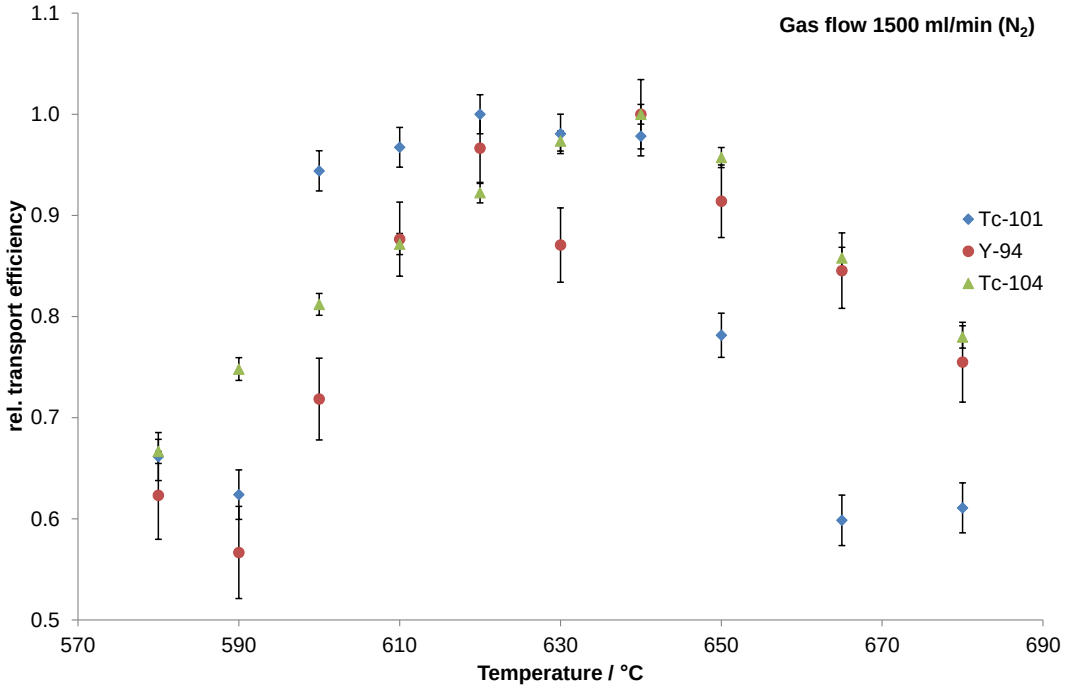


**Figure 4.1:** Relative transport efficiency of Tc-101, Tc-104 and Y-94 as a function of the furnace temperature, using KCl as aerosol material at a constant $N_2$ gas flow rate of 1500 ml/min.

that the capillary inlets get stuck with deposited aerosol material more quickly when higher temperatures are used.

For $CdI_2$ as aerosol material, the same investigations were performed as for KCl. The first temperature dependence was recorded in the range from 250-340°C at a constant $N_2$ gas flow rate of 1500 ml/min (see fig. 4.3). Apart from the abrupt efficiency decrease for Y-94 at temperatures above 310°C, the trend of the Tc isotopes shows a maximum around 310°C. Like for KCl, a fast deposition of macroscopic amounts of aerosol material in the capillary system was observed at high temperature. Therefore, the usual operating temperature for $CdI_2$ was 290-300°C.

The measurement was also repeated in the range from 270-310°C at a lower gas flow rate of 400 ml/min (see fig. 4.4). The maximum of the transport efficiency shifted slightly to lower temperatures and is located at 290°C.

### 4.1.2 Influence of gas flow rate

The influence of the $N_2$ gas flow rate on the transport efficiency with KCl and $CdI_2$ as aerosol material was measured. For KCl, the flow rate was varied from 200-1500 ml/min at a constant oven temperature of 630°C (see fig. 4.5). The transport efficiency rises

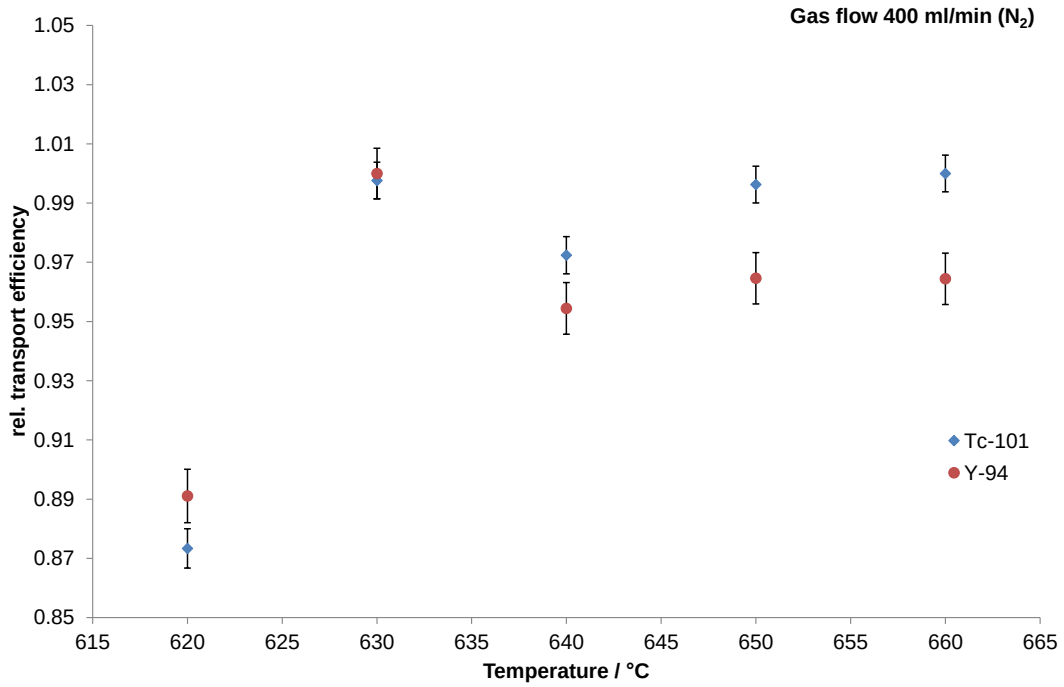


**Figure 4.2:** Relative transport efficiency of Tc-101 and Y-94 as a function of the furnace temperature, using KCl as aerosol material at a constant $N_2$ gas flow rate of 400 ml/min.

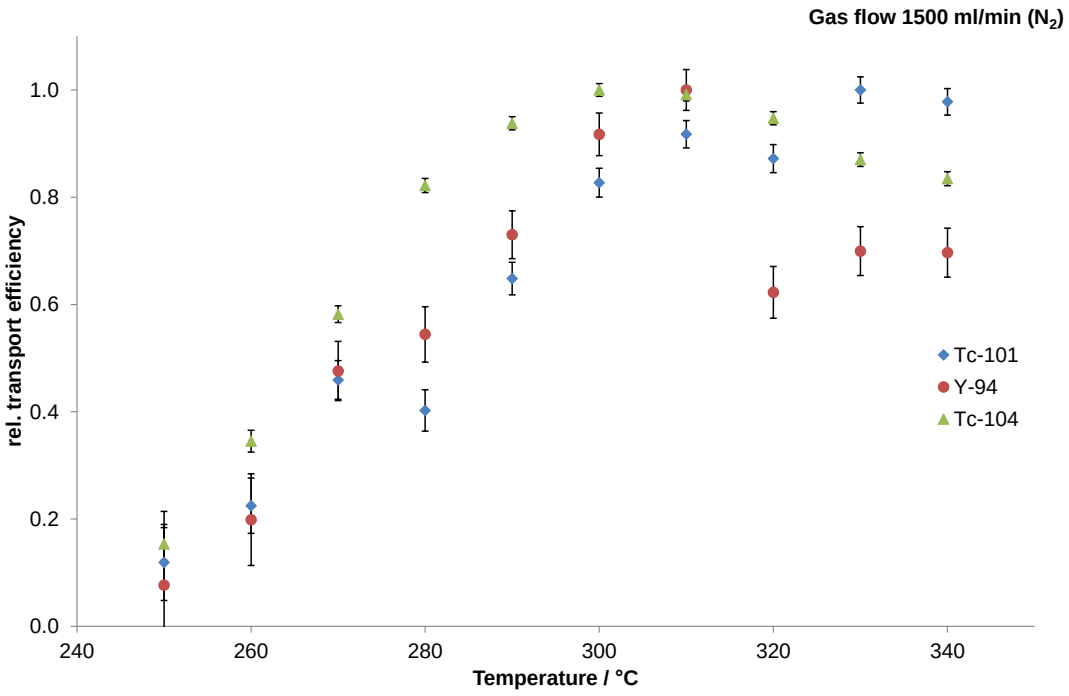


**Figure 4.3:** Relative transport efficiency of Tc-101, Tc-104 and Y-94 as a function of the furnace temperature, using $CdI_2$ as aerosol material at a constant $N_2$ gas flow rate of 1500 ml/min.

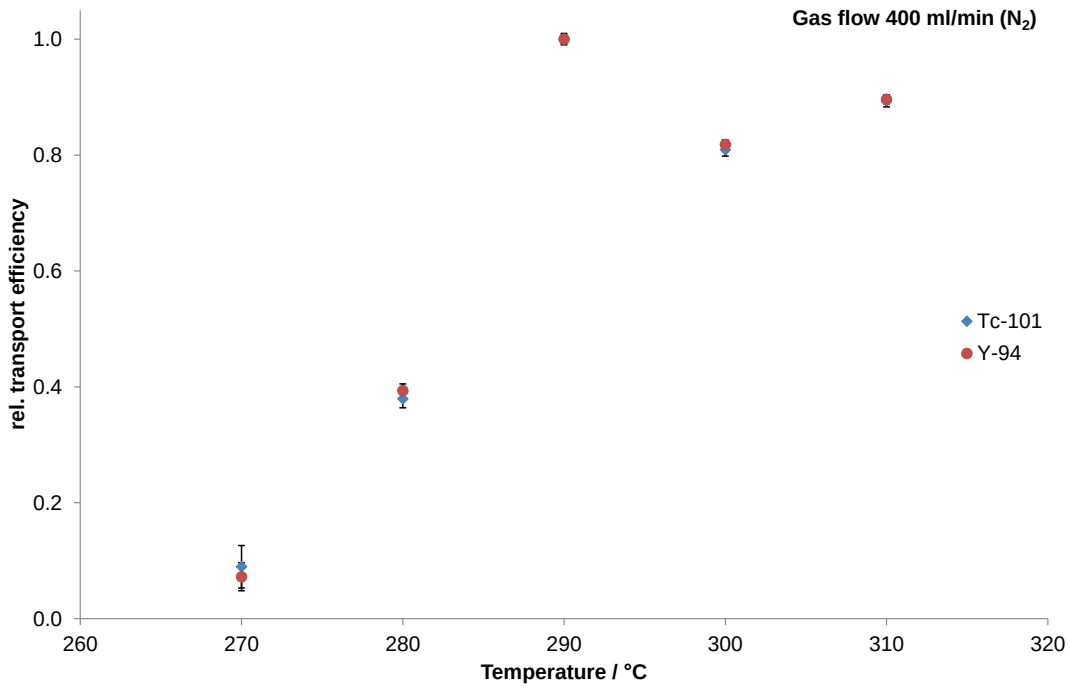


**Figure 4.4:** Relative transport efficiency of Tc-101 and Y-94 as a function of the furnace temperature, using $CdI_2$ as aerosol material at a constant $N_2$ gas flow rate of 400 ml/min.

with higher gas flow rate, so that the best value was reached at the highest flow rate of 1500 ml/min. The limiting factor was the pressure inside the target chamber which reached more than 3.5 bar. A higher pressure is not recommended to avoid the risk of a leakage which releases volatile fission products into the air.

This behavior was problematic for the design of the aerodynamic lens, because the total length of the lens scales with the gas flow rate. To keep the lens short enough to fit into the available space inside the vacuum chamber, it was necessary to reduce the gas flow rate to a value of about 400 ml/min. But this would result in a low transport efficiency of only about 20% compared to the transport with 1500 ml/min. To achieve also adequate transport rates at lower gas flow rates, the capillary system was rebuilt with respect to short transport distances. The total length of the necessary capillaries was reduces by a factor of two and the diameter of the capillary to the ion source and to the DC was changed from 1 mm to 1.2 mm.

The effect of different gas flow rates (200-800 ml/min) on the transport efficiency with KCl at a constant temperature of 630°C was investigated a second time with the improved capillary system (see fig. 4.6). Below a flow rate of 300 ml/min the transport efficiency still drops to only about 10% of the maximum yield, but the behavior for

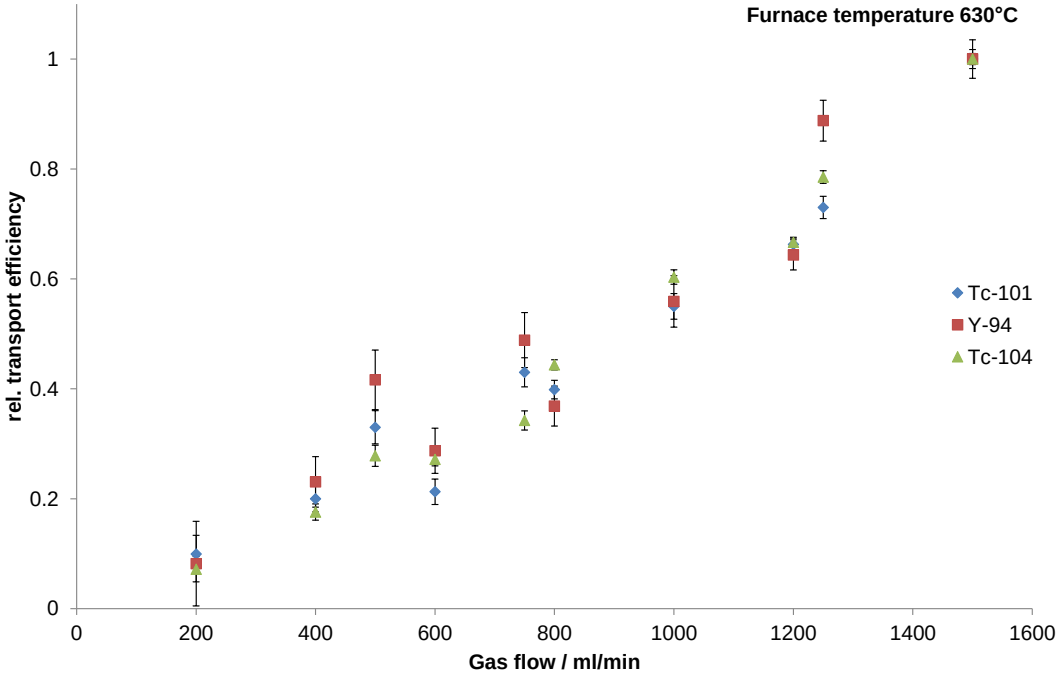


**Figure 4.5:** Relative transport efficiency of Tc-101, Tc-104 and Y-94 as a function of the gas flow rate, using KCl as aerosol material at a constant furnace temperature of 630°C.

higher flow rates changed. The amount of transported fission products is now relatively constant from 400-800 ml/min within the corresponding error bars. So it was no longer necessary to operate the gas-jet at an as high flow rate as possible, because the required 400 ml/min for the aerodynamic lens provided a sufficiently high transport efficiency.

For $CdI_2$ the dependence of the transport efficiency on the $N_2$ gas flow rate behaved different from the situation with KCl. With the old capillary system, the gas flow rate was investigated in the range from 600 to 1200 ml/min at a constant oven temperature of 290°C. Figure 4.7 shows a maximum for the transport efficiency at 800 ml/min. Higher flow rates reduce the amount of transported fission products.

For $CdI_2$ the gas flow rate dependence was also investigated a second time after the improvement of the capillary system. The flow rate was changed from 200 to 800 ml/min at a constant temperature of 290°C (see fig. 4.8). Similar to the investigations with KCl, the optimal gas flow rate could be shifted to a lower value. But for $CdI_2$ the situation is even more advantageous as for KCl, because the maximum of the transport efficiency fits perfectly to the demanded gas flow rate of 400 ml/min for the aerodynamic lens design.

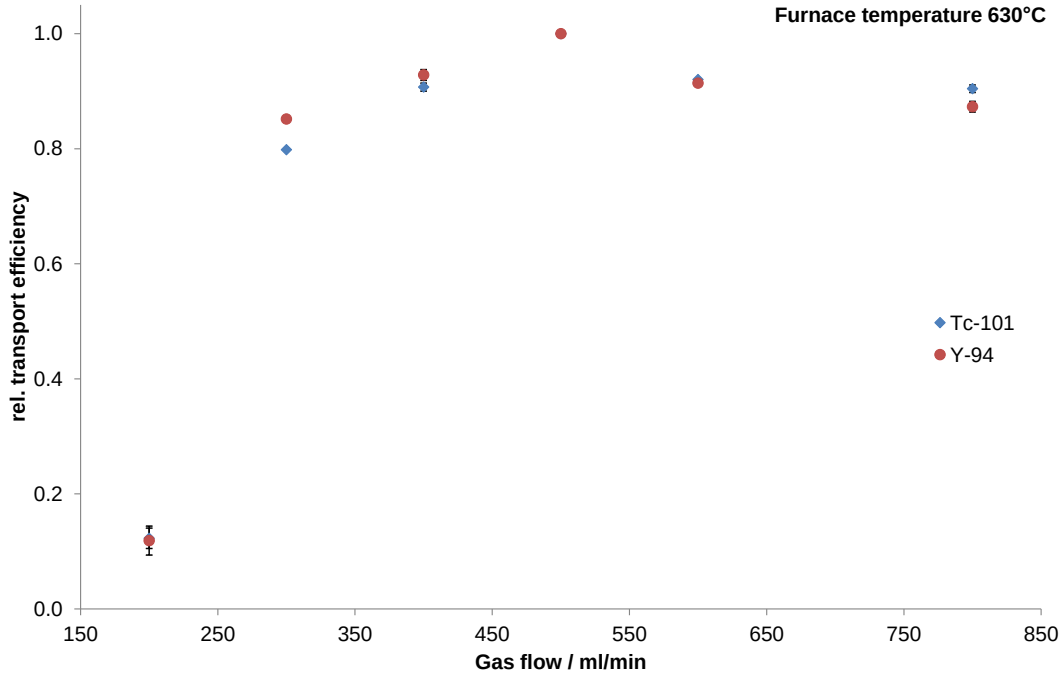


**Figure 4.6:** Relative transport efficiency of Tc-101 and Y-94 as a function of the gas flow rate after the improvement of the capillary system, using KCl as aerosol material at a constant furnace temperature of 630°C.

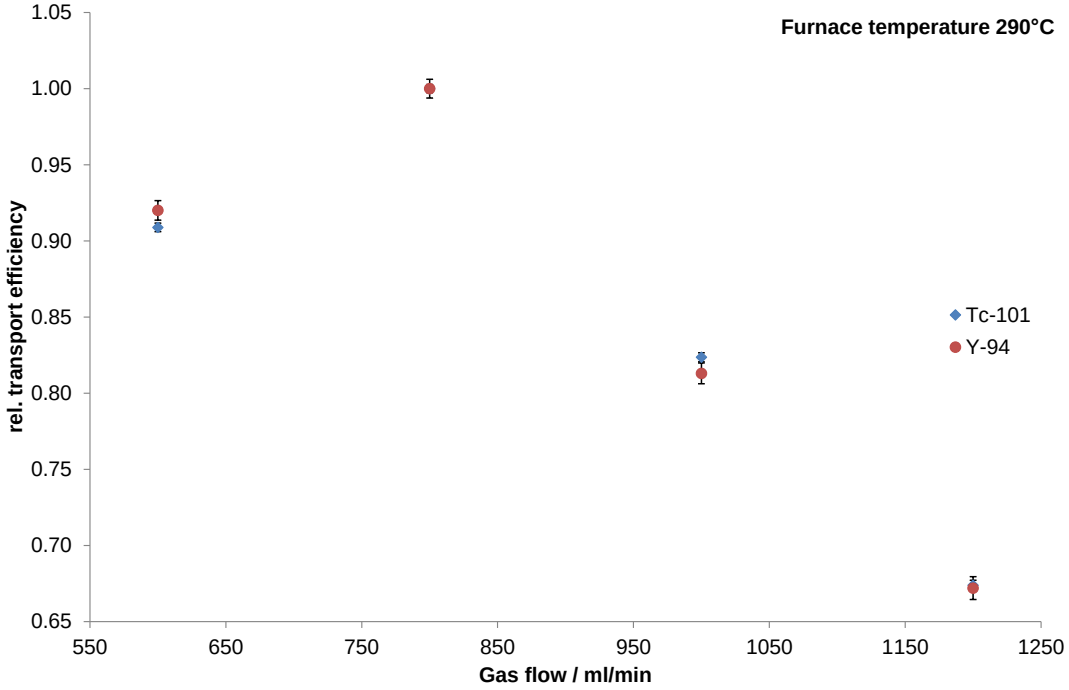


**Figure 4.7:** Relative transport efficiency of Tc-101 and Y-94 as a function of the gas flow rate, using $CdI_2$ as aerosol material at a constant furnace temperature of 290°C.

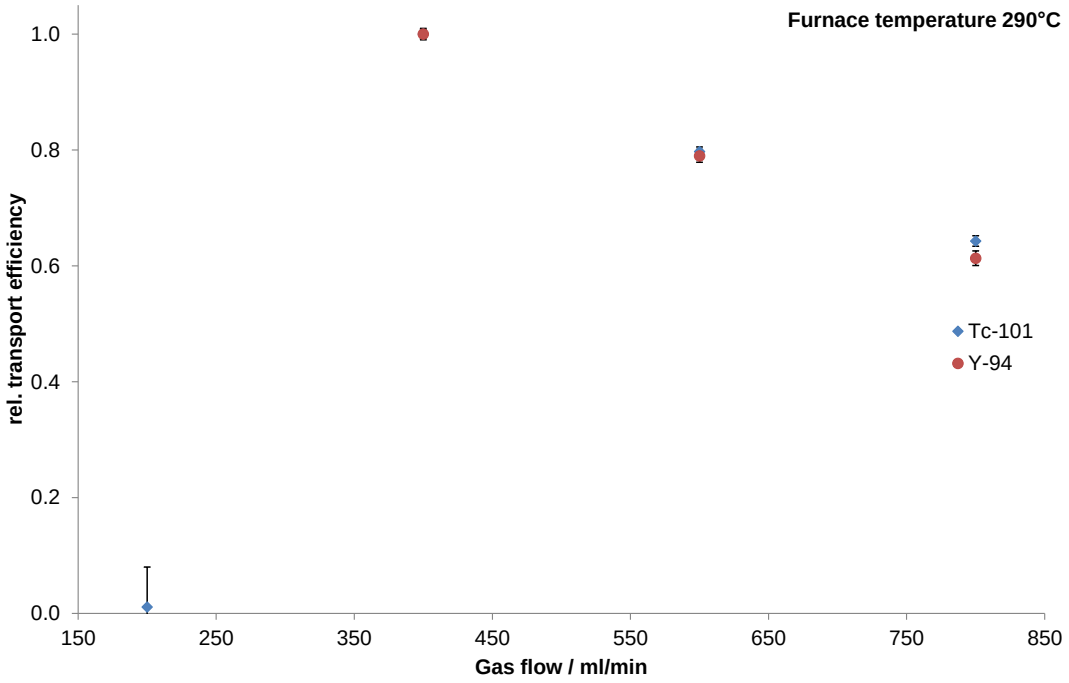


**Figure 4.8:** Relative transport efficiency of Tc-101 and Y-94 as a function of the gas flow rate after the improvement of the capillary system, using $CdI_2$ as aerosol material at a constant furnace temperature of 290°C.

### 4.1.3 Comparison of KCl and $CdI_2$

The absolute values of the maxima of the temperature plots for KCl and $CdI_2$ were used to compare the two aerosol materials. The absolute transport rate was higher for KCl, so these values were defined as 100%. Figure 4.9 shows a bar chart of the transport efficiency of $CdI_2$ under optimal conditions relative to the efficiency of KCl. After taking the average from both measurement series, the relative transport efficiency of $Cd_2$ was found to be 71.6±7.3% (average of the values in fig. 4.9). This value is in good agreement with data from Sato et al. [55], who compared the transport efficiency of KCl and $CdI_2$ using a He-based gas-jet system.

## 4.2 Temperature measurements

Figure 4.10 shows temperature measurements performed with both pyrometers at different heating powers. The absolute temperature appears to be lower when measured with the newer IR radiation pyrometer. This is likely primarily a problem of the adjustment of the pyrometer's optics onto the hottest spot of the source. The pyrometer averages over an area of 4 mm in diameter, which corresponds to the size of the ion source. Al-

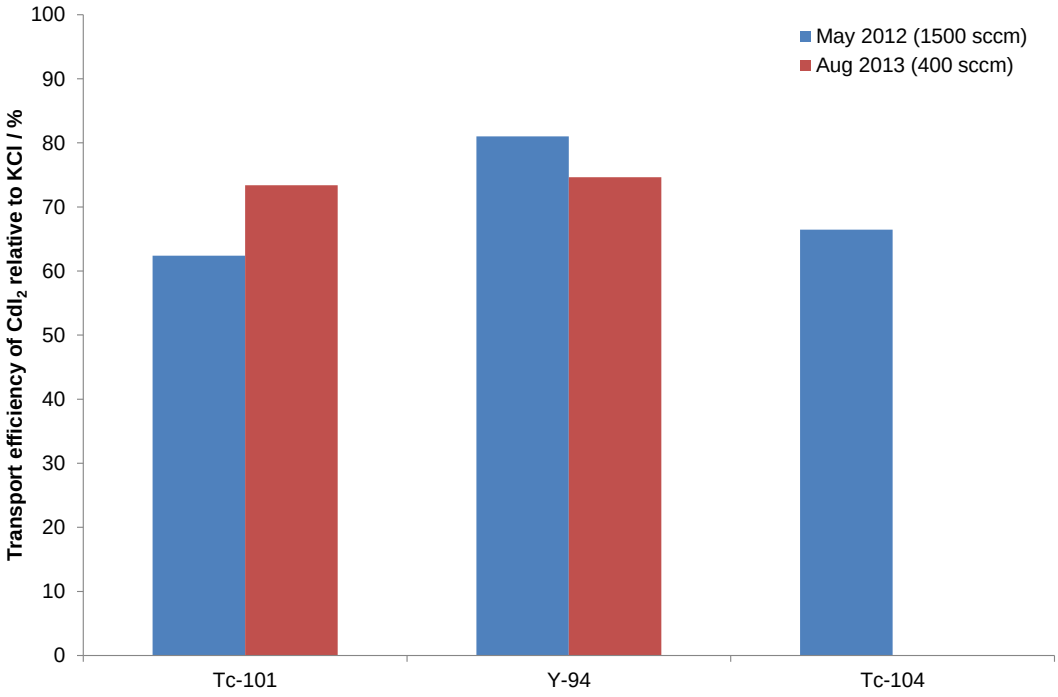


**Figure 4.9:** Transport efficiency of $CdI_2$ relative to KCl. The optimal production conditions were chosen for both aerosol materials. A value for Tc-104 from the beam time "Aug 2013" is not available, because the target material was changed from Cf-249 to U-235, so that the production rate of Tc-104 was too low for a meaningful evaluation.

ready a small misalignment of the optics by less than 1 mm can influence the measured temperature by more than 100°C.

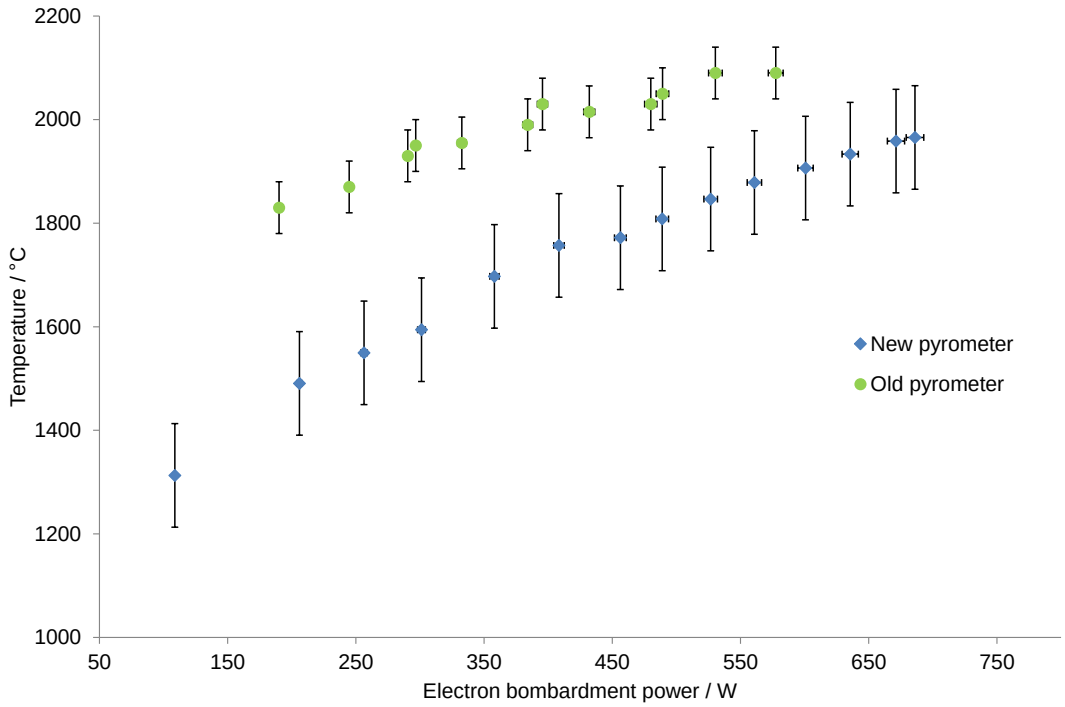


**Figure 4.10:** Measurements of the surface ion source temperature as a function of the electron bombardment power, using two different pyrometers. The "old" pyrometer was a disappearing-filament pyrometer, the "new" pyrometer is an IR radiation pyrometer. The new measurement results in a lower absolute temperature, because the IR pyrometer averages over a certain area. But the general slope is identical in both cases and only with the new device an online temperature control of the ion source is possible. The error bars for the new pyrometer include the uncertainty caused by the manual alignment and the unknown emissivity $\varepsilon$.

Another crucial parameter of the pyrometer calibration is the emissivity $\varepsilon$ of the source, which is not known. The literature value for pure tungsten is $\varepsilon = 0.288$ at 2300 K [74]. But the emissivity is not only a function of the temperature, it is also a function of the surface roughness [119]. The structural properties of the used tungsten, especially after being heated up and cooled down for several times, are unknown. The influence of the selected emissivity on the measured temperature is shown in fig. 4.11. The ion source was operated at a constant EB power of 613 W, while the selected emissivity of the pyrometer was changed from 0.1 to 1.0. Especially for bodies with a low emissivity the error of the absolute temperature measurement can be relative large, if the wrong emissivity is selected. For the temperature measurements shown in fig. 4.10 an emissivity of $\varepsilon = 0.3$ has been assumed.

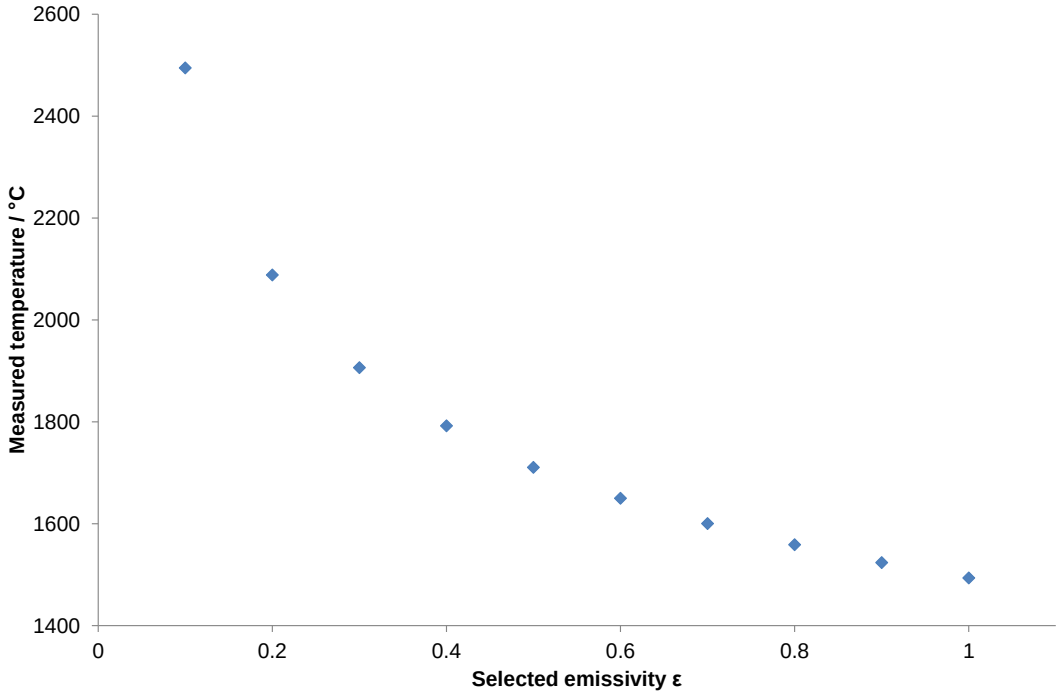


**Figure 4.11:** Influence of the selected emissivity $\varepsilon$ of the IR radiation pyrometer on the read out temperature.

The most important parameters for the surface ionization process are the temperature at the hottest point of the ion source and the temperature distribution along the tungsten tube. Both parameters cannot be observed with the pyrometers looking on the exit orifice of the source. A detailed estimation on the temperature flux along the tube is difficult, because multiple effects with unknown quantity and weighting have to be taken into account. Figure 4.12 presents an illustration of the complex temperature distribution which has to be regarded. The EB heats the center of the tube to a maximum temperature $T_{max}$. This establishes a temperature gradient $\Delta T$ along the tube, which depends on the thermal conductivity of the material. One problem is that only the total EB power is known, but not all of this energy is used to heat the ionizer. A certain fraction of the power is lost by heating the surrounding parts and the vacuum chamber. Additional losses are caused by thermal contact to the BN insulator and the front plate and by thermal radiation. In the end, only a rough estimation can be given that $T_{max}$ is likely about 100-200°C higher than the observable temperature $T_{end}$.

Although the absolute temperature recorded by the IR pyrometer has a significant uncertainty, the monitoring of the temperature stability is a valuable feature to follow a possible temperature drift on a long-time scale. Figure 4.13 shows the temperature

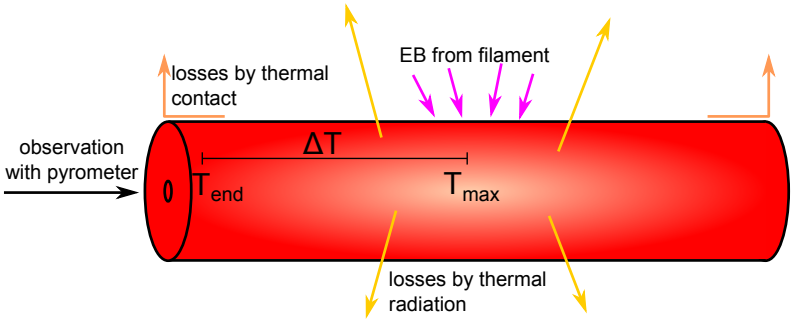


**Figure 4.12:** Illustration of the temperature distribution along the tungsten ionizer of the surface ion source. Only a relatively small area is heated directly by electron bombardment to a maximum temperature $T_{max}$. The only temperature which can be measured is $T_{end}$ at the end of the ionizer. See text for details.

stability of the surface ion source at a constant EB power of 524 W over a period of 3 hours.

The temperature drop after around 20 minutes occurs from an adjustment of the EB power, because this was slowly increasing. After this adjustment the EB remained at a relative constantly power (less than 10 W fluctuation during the regarded period). The temperature remains around an average value of about 1506°C. The most noticeable discrepancies from this mean value are the three temperature drops between 2 and 3 h, where the measured temperature dropped by more than 3°C for less than a minute. A possible reason are minor discharges at the electron bombardment. But after each breakdown, the source gets quickly back to the former temperature. With the exception of the mentioned drops, the difference between $T_{max}$ and $T_{min}$ is 5.5°C. A temperature fluctuation of this size is not expected to affect the ionization efficiency on an observable level.

## 4.3 Transport to the surface ion source and ionization of fission products

### 4.3.1 Catching procedures for characterization of the online coupling

To characterize the transport efficiency from the reactor towards the ions source as well as the ionization efficiency of the source, catches of fission products were performed at different positions of the setup. The positions are marked and labeled in fig. 4.14, showing a sketch of the TRIGA-SPEC common beamline.

The 100% catch in front of the U-235 target serves as reference point to compare the other catches with. In general, fission products were collected for 10 min and measured

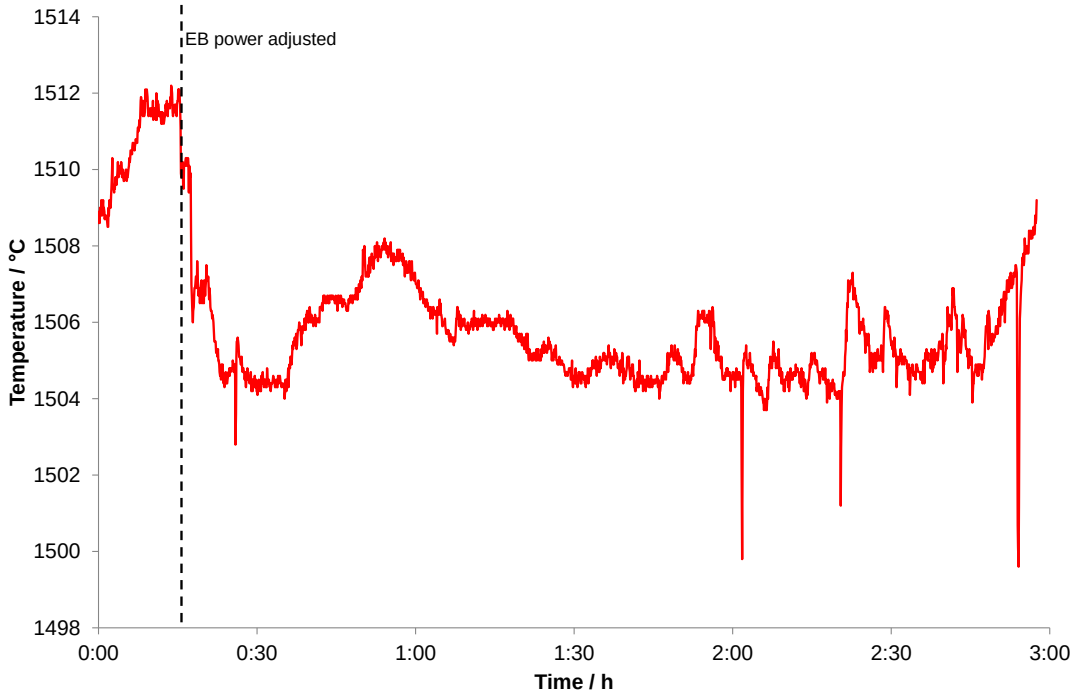


**Figure 4.13:** Temperature stability of the ion source over 3 h. The electron bombardment power was adjusted once, to avoid a constant drift of the heating power. See text for details.

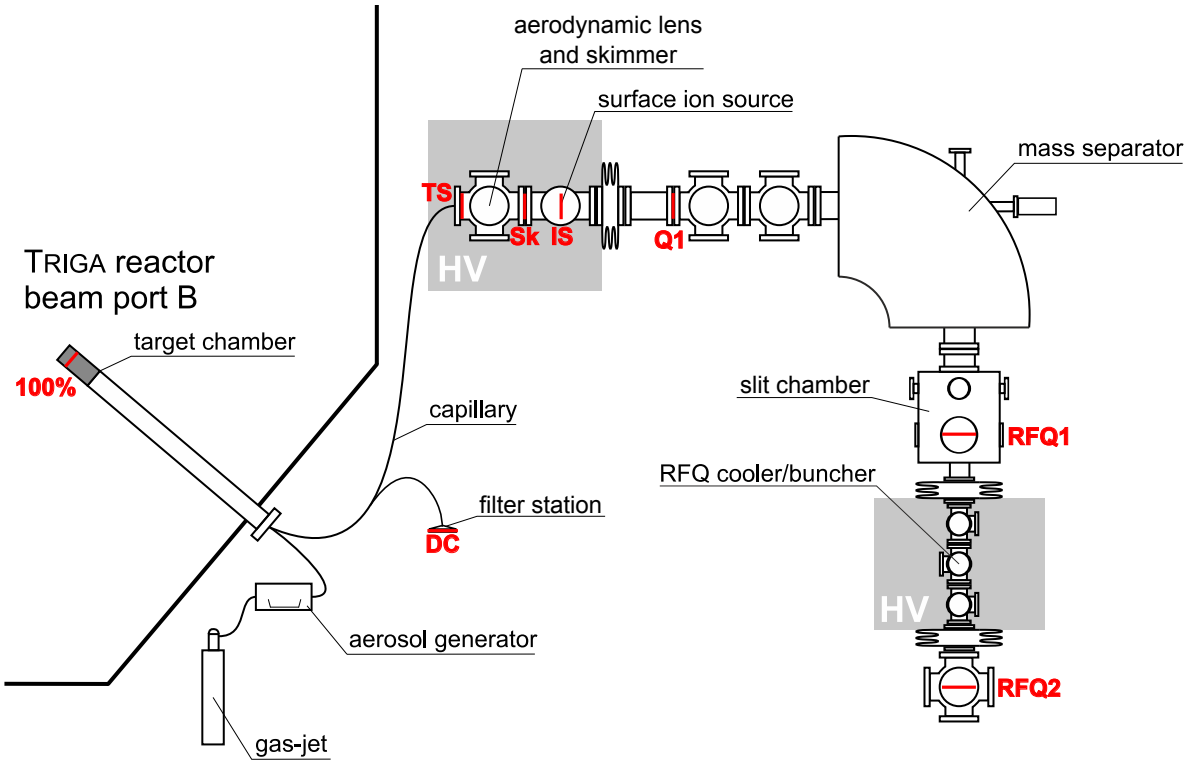


**Figure 4.14:** Sketch of the gas-jet system and the common beamline of TRIGA-SPEC. All positions used for catches of fission products are marked and labeled in red.

for 30 min after a waiting time of 30 min. For some long-lived nuclides, especially Sr-91 and Sr-92, an additional measurement time of 10 h after a waiting time of 1 h was performed to gain sufficient statistics.

Figure 4.15 shows a representative $\gamma$-spectrum obtained by a DC after the mentioned measurement procedure. Most $\gamma$-measurements were done with a detector located close to the TRIGA reactor, which causes some background from annihilation (511 keV), caused by pair production of high-energy photons, Ar-41 (1294 keV) and K-40 (1461 keV). A typical background spectrum from the reactor hall is also shown in fig. 4.15 in green.

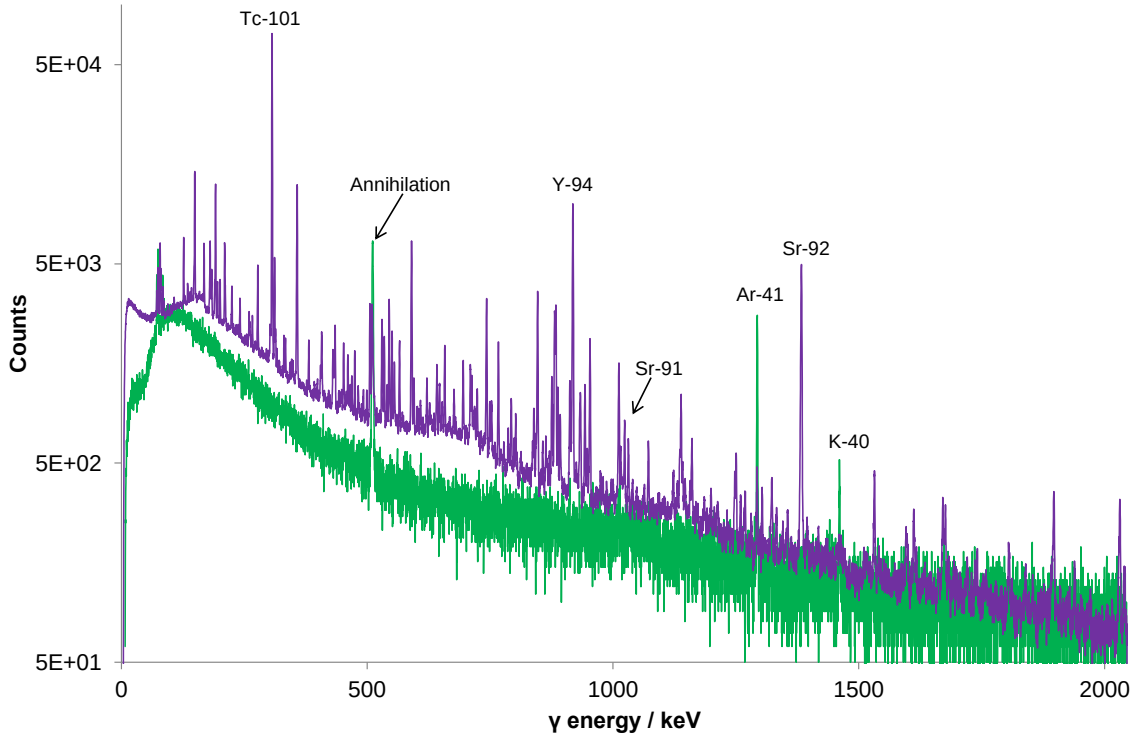


**Figure 4.15:** $\gamma$ spectrum of a direct catch (violet), recorded with a detector inside the reactor hall. A background spectrum recorded with the same detector while the reactor was running at 100 kW is shown in green (background data multiplied with 10 for better visibility). The labeled Tc, Sr and Y isotopes were used for the ion source and beamline characterization.

The strongest $\gamma$-lines of $^{101}$Tc, $^{91,92}$Sr and $^{94}$Y, which are labeled in the spectrum are considered for the evaluation. The 307 keV $\gamma$-line of $^{101}$Tc is usually the most intense peak in the spectrum and provides accordingly a low statistical error. But the ionization potential of Tc is far too high to get any detectable amounts of ionized Tc from the surface ion source, so that it cannot be used for a comparison of ions collected behind the SIS. Rb and Sr have a sufficiently low ionization potential to get intense ion beams, so these are the primary elements of interest during the commissioning phase of the common

beamline. Unfortunately, all Rb isotopes with a sufficiently high production rate have half-lives of only a few minutes or less. Because of this situation, the Sr and Y nuclides which follow the decay of the Rb isotopes have to be regarded. Figure 4.16 shows the decay series of mass numbers A = 91, 92, 94 and tab. 4 summarizes important data of the nuclides which are relevant for the later evaluations. All nuclides with half-lives of only a few minutes or less cannot be used for the catches behind the ion source, because of the time needed for the dismounting of the catcher foil. The series with mass number 93 would be also interesting, because of the high production rate of the involved nuclides and the long half-life of Y-93 (10.2 h), but it's most intense $\gamma$-line has an intensity of only 7.3%, so that it is hard to get a satisfactory count rate.

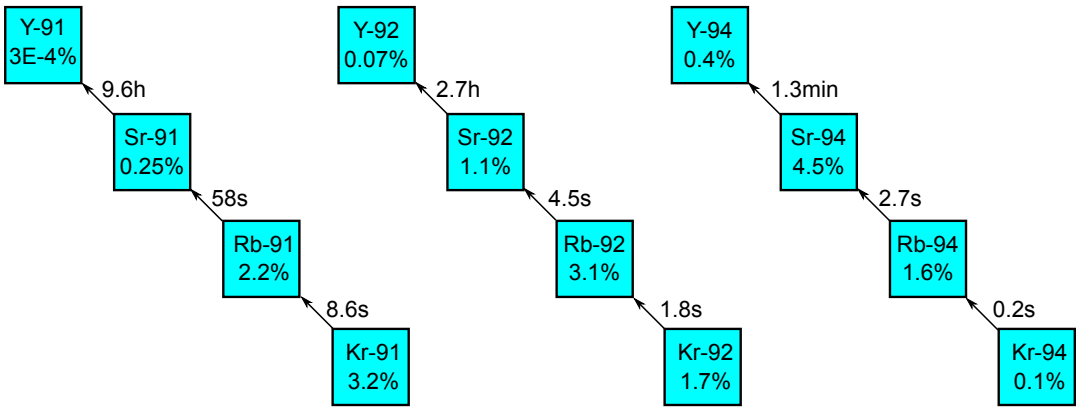


**Figure 4.16:** Decay series of mass numbers A = 91, 92, 94 from Rb to Y. The percentages give the independent fission yield (for U-235) of the particular nuclide.

**Table 4:** $\gamma$-energy and -intensity, half-life $T_{1/2}$ and detector efficiency for different fission products that are relevant for later evaluations.

| Nuclide | $\gamma$-energy / keV | $\gamma$-intensity / % | $T_{1/2}$ / min | Det.eff. / % |
|---|---|---|---|---|
| Tc-101 | 307 | 88.7 | 14.2 | 1.88 |
| Sr-91 | 1024 | 33.5 | 577.8 | 0.84 |
| Sr-92 | 1384 | 100 | 162.6 | 0.68 |
| Y-94 | 919 | 56 | 18.7 | 0.90 |

An unknown source for uncertainty for this kind of evaluations are possible precursor effects caused by the respective Kr isotopes, decaying into the regarded Rb isotopes. The effect can be neglected for the ionization process in the ion source, because Kr as a noble gas should be pumped away together with the carrier gas by the roots pump.

Small amounts of Kr which enter the ion source anyway should not be ionized due to the very high first ionization potential of 14.0 eV. But different transport times, caused by the 2 m longer capillary to the ion source than to the direct catch, or unknown retention times of gaseous species compared to aerosol particles, e.g., in the glass fiber filters, can cause influences by the Kr precursors. This will be also discussed in sec. 4.3.4.

### 4.3.2 Absolute yield of fission products of U-235 targets

100% catches of the old (2012) and the new (2015) U-235 targets have been performed as described in sec. 3.1.1. Table 5 shows a comparison of the absolute number of fission products per second for different nuclides. The numbers are corrected for the $\gamma$-intensity, the detector efficiency and the decay during catching, waiting and measuring time. On average, the new target delivers a factor of 13.3±1.0 more fission products than the old target. This value is in good agreement with the estimation of a factor of 14 in sec. 3.1.1.

**Table 5:** Comparison of the 100%-catches of the $^{235}$U targets from 2012 and 2015 with respect to the nuclides that are most interesting for the later transport and ionization analysis. The absolute numbers of fission products per second are corrected for the $\gamma$-intensity, the detector efficiency and the timings of the catches.

| Nuclide | 100%-catch 2012 / 1/s | 100%-catch 2015 / 1/s | Ratio "2015"/"2012" |
|---|---|---|---|
| Tc-101 | 2.91E+04 | 3.64E+05 | 12.5 |
| Sr-91 | 1.40E+04 | 1.75E+05 | 12.5 |
| Sr-92 | 1.37E+04 | 1.93E+05 | 14.1 |
| Y-94 | 1.40E+04 | 2.00E+05 | 14.2 |

### 4.3.3 Transport efficiency to the ion source

The transport efficiencies for a direct catch (DC), to the TRIGA-SPEC beamline (TS) and through the combined aerodynamic lens and skimmer system into the surface ion source (IS) are presented in tab. 6. The percentaged values are relative to the 100% catch of the U-235 target. All numbers are mean values based on the latest beamtime (February to April 2015), using a $N_2/CdI_2$ gas-jet with a gas flow rate of 400 ml/min at an oven temperature of 290°C.

**Table 6:** Averaged relative transport efficiencies, compared to the 100%-catch 2015, of different fission products to a direct catch (DC), to the TRIGA-SPEC beamline (TS) and through the combined aerodynamic lens and skimmer system into the ion source (IS).

| Nuclide | DC / % | TS / % | IS / % |
|---|---|---|---|
| Tc-101 | 49.9 | 41.6 | 28.4 |
| Sr-91 | 28.5 | 25.8 | 16.7 |
| Sr-92 | 45.5 | 39.1 | 26.7 |
| Y-94 | 49.7 | 41.9 | 28.8 |
| Average | 43.4(10.1) | 37.1(7.6) | 25.1(5.7) |

Although the average transport efficiency out of the target chamber reaches only roughly 43% in the DC, the transport to TRIGA-SPEC through a capillary which is approximately 2 m longer works with a comparable average efficiency of roughly 37%. The average transport efficiency through the skimmer into the SIS, 67.5±1.9%, could be boosted significantly by the installation of the aerodynamic lens in front of the skimmer. The earlier efficiencies without the lens were only 15.3±2.5% for KCl and 20.6±8.4% for $CdI_2$. The current lens works only with $CdI_2$, which is the preferred aerosol material, but a new design of a lens which should handle both species is under development. The transport efficiency into the SIS relative to the 100%-Catch is roughly 25% ($= 37\% \cdot 67.5\%$).

With the known detector efficiency, the intensity of the particular $\gamma$-lines and the timings of the measurement procedure, the absolute number of the collected radionuclides or rather the rate of transported nuclides per second could be calculated. Tab. 7 summarizes the transport rates to the different stages of the setup.

**Table 7:** Averaged yields of fission products per second at the 100%-catch 2015, at a direct catch (DC), at the TRIGA-SPEC beamline (TS) and inside the ion source (IS) at 100 kW TRIGA power.

| Nuclide | 100%-catch 2015 / 1/s | DC / 1/s | TS / 1/s | IS / 1/s |
|---|---|---|---|---|
| Tc-101 | 3.64(6)E+05 | 1.81(3)E+05 | 1.51(3)E+05 | 1.03(2)E+05 |
| Sr-91 | 1.75(4)E+05 | 5.00(93)E+04 | 4.52(89)E+04 | 2.93(71)E+04 |
| Sr-92 | 1.93(4)E+05 | 8.83(45)E+04 | 7.58(42)E+04 | 5.17(35)E+04 |
| Y-94 | 2.00(4)E+05 | 9.92(39)E+04 | 8.37(35)E+04 | 5.74(29)E+04 |

These absolute rates, given in the last column, are the initial point for the characterization of the ionization efficiency of the SIS, discussed in the next section.

### 4.3.4 Ionization efficiencies and absolute ion rates

The most important catching position is located on the first detector unit behind the separator magnet and in front of the RFQ, labeled as RFQ1 in fig. 4.14. Most catches of radioactive ions from the SIS were done at this position. Catches behind the RFQ, position RFQ2, were used to verify the transmission efficiency of the RFQ in the continuous mode. One special catching position is in front of the first deflector, Q1. This is the closest possible position to the ion source were catches can be done. The extraction electrode is the only ion-optical element between the catcher foil and the source. Attempts to place a foil directly on the extraction electrode were not successful, because the Al foil does not survive the temperatures so close to the hot source. It was also tried to place a W foil at this position, but for unknown reason no fission products were detected after irradiation.

**Table 8:** Catches of ionized fission products at different positions behind the ion source. EB gives the electron bombardment power of the ion source during the collection. The IS/DC ratio gives the ion rate determined behind the ion source relative to a comparable DC during the same beamtime.

| Beamtime | Position | Nuclide | EB / W | Ions / s | IS/DC / % |
|---|---|---|---|---|---|
| Nov2012 | RFQ1 | Sr-91 | 592 | 79 | 0.5 |
| Nov2012 | RFQ2 | Sr-91 | 593 | 25 | 0.2 |
| Nov2013 | Q1 | Sr-91 | 415 | 50 | 0.5 |
| Nov2013 | Q1 | Sr-92 | 415 | 23 | 0.3 |
| Nov2013 | Q1 | Sr-91 | 540 | 61 | 0.9 |
| Nov2013 | Q1 | Sr-92 | 540 | 37 | 0.5 |
| Aug2014 | RFQ1 | Sr-91 | 592 | 104 | 3.6 |
| Aug2014 | RFQ1 | Sr-91 | 623 | 130 | 4.6 |
| Feb2015 | RFQ1 | Sr-91 | 416 | 9289 | 4.0 |
| Feb2015 | RFQ1 | Sr-92 | 423 | 6055 | 4.7 |
| Feb2015 | RFQ1 | Sr-92 | 488 | 8543 | 6.6 |
| Feb2015 | RFQ1 | Y-94 | 498 | 4150 | 3.8 |
| Feb2015 | RFQ1 | Y-94 | 569 | 2592 | 2.3 |

Table 8 presents all important catches on these positions, with the corresponding electron bombardment power of the ion source, the collected ions/s (corrected for the

decaying time, detector efficiencies and $\gamma$-intensities) and the relative efficiency compared to direct catches measured within the same beamtime.

The comparison of the RFQ1/RFQ2 catches results in a RFQ transmission efficiency of about 32%. During offline measurements with the Faraday Cups in front of and behind the RFQ a similar transmission of about 25% was found for K [82]. The transmission through the RFQ was not remeasured for quite some time now and should be verified again before the next attempt to go with an online ion beam towards one of the experimental branches. But no fundamental changes were done on the RFQ since these measurements and it can be assumed that this efficiency will be reproducible in the future.

The catches on the Q1 position offer an interesting possibility to gain some information about the relative ionization efficiencies of Rb and Sr, because without any mass separation all possible radionuclides leaving the source are collected and measured simultaneously. The major drawback is that a waiting time of at least 2 h is necessary, to give the ion source time to cool down, so that the vacuum can be breached without risk. After such a long waiting time, only long-lived fission products as Sr-91 and Sr-92 can be detected.

A change in the detected Sr-91/Sr-92 ratio before and after the ionization can give a hint on the relative ionization efficiencies. The Sr ratio which is measured in the direct catches is about 0.64, so after the decay of all collected precursors more Sr-92 than Sr-91 is present (see tab. 9). In all catches which were done behind the ion source, this relation turned over completely, because the Sr-91/Sr-92 ratio is always >1, so more Sr-91 than Sr-92 is detected. The ratio usually comes up at about 1.5. This change of the ratio likely originates from the different ionization efficiency of Sr and its precursor Rb.

Documented fission yields [15] can be used to calculate the expected Sr-91/92 ratios. By assuming a quantitative collection of Rb and Sr in the direct catches, an Sr-91/Sr-92 ratio of 0.78 can be expected from the independent fission yields of the involved Rb and Sr isotopes after the usual waiting and measuring time. This ratio is close to the measured ratio from the direct catches. If it is assumed that the ionization efficiency for Rb is much larger than for Sr, one expects that the measured Sr ratio behind the ion source shifts closer to the Rb ratio produced during the fission process, because the Rb precursors are the main source for the measured Sr isotopes. We assume an ionization efficiency of 100% for Rb and only 10% for Sr. But the expected Sr ratio, based on the independent fission yields, only ends up at about 0.9, so it is not so much different from the ratio measured in the DCs. Only if the cumulative fission yields for Rb, including the

decay of further precursor nuclides like Kr, is used for the calculation, a ratio of about 1.5 is obtained. An even lower ionization efficiency for Sr does not affect the calculated ratio significantly.

**Table 9:** Theoretically and experimentally determined Sr-91/Sr-92 ratios. The theoretical values are based on the fission yield data of England [15]. For the theoretical values at the direct catch (DC) position a quantitative collection of Rb and Sr is assumed. At the Q1 position (behind the ion source) ionization efficiencies of 100% for Rb and 10% for Sr were assumed. The experimental values in the DC fit quite well to the calculated ones, if the independent fission yields are regarded. In the case of the Q1 catches, the experimental values fit much better to the calculated value obtained with the cumulative fission yields, including further precursors like Kr.

| Catch | $\text{Theo}_{\text{ind}}$ | $\text{Theo}_{\text{cum}}$ | Exp |
|---|---|---|---|
| DC | 0.78 | 1.40 | 0.64(3) |
| Q1 | 0.92 | 1.51 | 1.53(5) |

So, the observed Sr ratio behind the ion source can be explained, if the Rb ionization is at least a factor of 10 more efficient than the Sr ionization and if precursor effects are taken into account.

A possible reason for the precursor effect is the decay of Kr into Rb, during the time of flight to the surface ion source. The capillary to the SIS is about 2 m longer than the capillary to the DC, resulting in a longer time of flight. The time of flight of the aerosol from the target chamber to TRIGA-SPEC was measured in the past to be 390±90 ms [57], using helium as carrier gas with a flow rate of 1.4 l/min. The time of flight of the current setup is not known, but it can be assumed that it is longer, because of the reduced gas flow rate of only 400 ml/min (for $N_2$).

Another unknown factor influencing the catches at the Q1 position is the amount of neutral particles passing straight through the ion source. During the Q1 catches KCl was used as aerosol material. The ionizer is therefore loaded with large amounts of potassium, which is also easily ionized. This can lead to a hindrance of the ionization process of the radionuclides, if most of the surface positions are blocked by the aerosol material. Finally, the $\gamma$ count rates were relative low, so that a large statistical error results. All these uncertainties make it hard to determine an absolute ionization efficiency.

Between the beamtime Nov2013 and Aug2014 the capillary system was improved (see sec. 4.1.2) and the aerodynamic lens was installed, boosting the skimmer efficiency by more than a factor of 3. In addition, the latest design of the extraction electrode was installed, providing a more confined and better controllable ion beam than in former

beamtimes. During the installation of the new extraction, the alignment of the whole ion source beamline was optimized, so that the overall beam profile and the transfer efficiency could be improved. All these enhancements result in the higher IS/DC ratio (see tab. 8).

The RFQ1 catches from 2014 and 2015 show a relative amount of ions compared to direct catches in the range of 4%. The value depends on the temperature of the ion source, because a higher temperature should lead to an increased ionization efficiency. This trend is in principle visible by comparison of the Sr-91 (Aug2014) and Sr-92 (Feb2015) data, taken at different electron bombardment power. On the other hand, the second Y-94 measurement during the Feb2015 beamtime shows a significantly lower ion rate than the first catch, although the ion source was heated with about 15% more power. After the beamtime it was discovered that this loss of the ion rate originated from problems at the gas-jet transport and injection into the ion source. The long-time stability of all devices and systems involved at the common beamline is not guaranteed yet, making it difficult to give reproducible efficiencies for an individual device. The numbers presented in tab. 8 should be seen as possible optimal values for the actual setup, which can be achieved if all components work without interruption.

The large boost of the absolute ion number between the beamtime Aug2014 and Feb2015 is a result of the new U-235 target, described already in sec. 4.3.2. The absolute ion rates detected in front of the RFQ are now more than one order of magnitude higher than during earlier beamtimes. With such a strong ion beam it should be possible to get at least a small amount of radionuclides, Rb or Sr isotopes, towards the Penning traps. Further optimization attempts of the PDT and the subsequent transfer section would be also more promising with a stronger ion beam.

## 4.4 Ion source characterization with stable ion species

Apart from the characterization of the ion beam by catching radioactive ions at different positions of the beamline, also extensive studies using beams of stable nuclides have been performed. Important detection stages are the FC/MCP units behind the separator magnet and the RFQ. The ultimate test of the performance of the complete beamline are measurements in the experimental branches, so either performing collinear laser spectroscopy with TRIGA-LASER or trapping experiments with TRIGA-TRAP, using ions generated in the surface ion source of the common beamline.

### 4.4.1 Mass spectra and beam profile characterization

Figure 4.17 shows typical mass spectra recorded at the FC behind the separator magnet. The upper spectrum shows a scan over a wide mass range from 35 to 95 amu (assuming singly charged ions). The surface ion source was fed with a $N_2$/KCl gas-jet, which explains the strong K-39 peak. The characteristic peak pattern of the different natural Ca isotopes is also visible with high intensities, because the source was operated as an off-line source and filled with Ca for measurements at TRIGA-LASER prior to these measurements.

A more detailed scan of the K and Ca mass region (38 to 50 amu) is shown in the middle spectrum. It was recorded at the time where the ion source was filled up with Ca and operated without gas-jet. Residual traces of K are visible, but the spectrum is dominated by peaks which can be assigned to Ca ions. The peak intensities reflect the natural abundance of the different Ca isotopes[6]. The Ca beam was used for some preparatory laser spectroscopy measurements at TRIGA-LASER and for the final commissioning and characterization of the RFQ cooler and buncher [82, 113].

At the far end of the full spectrum, the two natural Rb isotopes, Rb-85 (72.2%) and Rb-87 (27.8%), are visible (lower panel). The origin of this natural Rb is most likely some trace amounts in the KCl aerosol material. However, the appearance of some stable isotopes close to the mass region which is interesting regarding fission products is advantageous, because they can be used as references for the mass calibration of the dipole magnet and for testing the operation conditions of the RFQ with ions of an appropriate m/q ratio. The lower spectrum in fig. 4.17 shows a detailed scan of the mass region from 82 to 90 amu. At 88 amu a small peak from Sr-88, the most abundant natural Sr isotope, is visible, although the signal-to-noise ratio is very small.

Unfortunately, the spectrum in the mass region >90 amu is not completely free of background. At some masses peaks of several pA are obtained. The origin of these ions is not absolutely clear. Molecular species of contamination inside the ion source or the carrier gas are a suspected source. The appearance of these background species makes it impossible to detect fission products by methods which do not distinguish between radioactive and stable species. Recall that the typical currents which can be expected from the ion rates of fission products, determined in sec. 4.3.4, are too low to get a significant signal on the FC. Assuming an ion rate of 10000 ions/s, this would result in a current of about 1.6 fA, whereas the average background of the FC is in the order of a few hundred fA.

[6] $^{40}$Ca: 96.941%, $^{42}$Ca: 0.647%, $^{43}$Ca: 0.135%, $^{44}$Ca: 2.086%, $^{46}$Ca: 0.004%, $^{48}$Ca: 0.187%

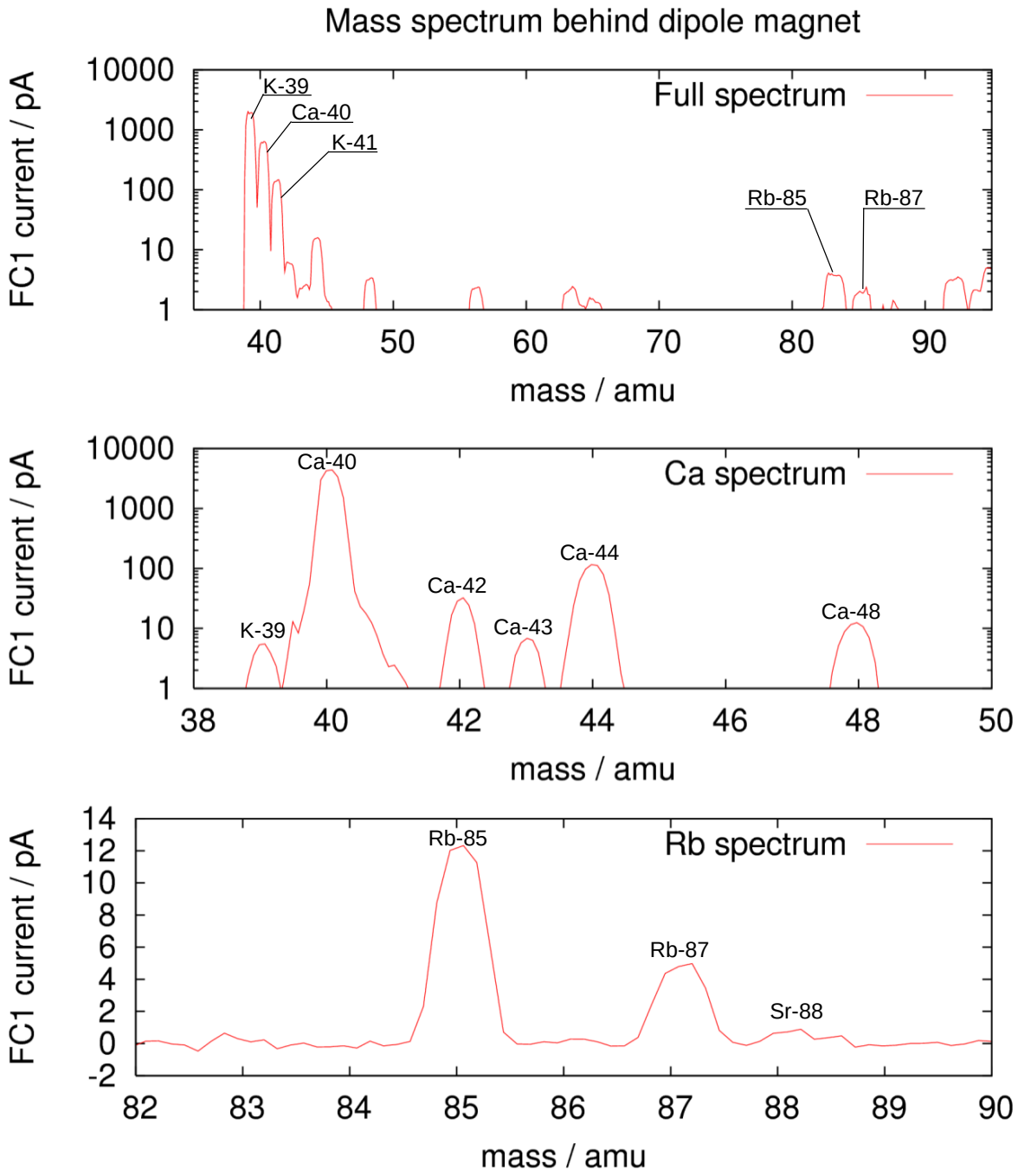


**Figure 4.17:** Mass spectra recorded at the FC behind the separator magnet. Top: Wide range scan from 35 to 95 amu. The strongest signals belong to K and Ca isotopes. Middle: Detailed scan of the K and Ca mass region. The ion source was filled with natural Ca for laser spectroscopy measurements at TRIGA-LASER. Bottom: Detailed scan of mass region around 85 amu. The two natural Rb isotopes are clearly visible and were used for mass calibration of the dipole magnet. Traces of natural Sr-88 are also detectable.

Figure 4.18 shows two pictures of the ion beams of Rb-85 and Rb-87, mass separated by the dipole magnet, monitored with the combined MCP/phosphor screen device. This detector is a valuable tool for monitoring of the beam profile and especially useful during the beam tuning procedure, because the effects of beam deflection and focusing are immediately visible. On the left picture the ion beam is not optimally focused, and the spots do not appear point-shaped, but a little bit blurred with a surrounding halo. On the right picture the focus is tuned better, so that the ion beams appear as bright, still a little bit elliptic, spots.

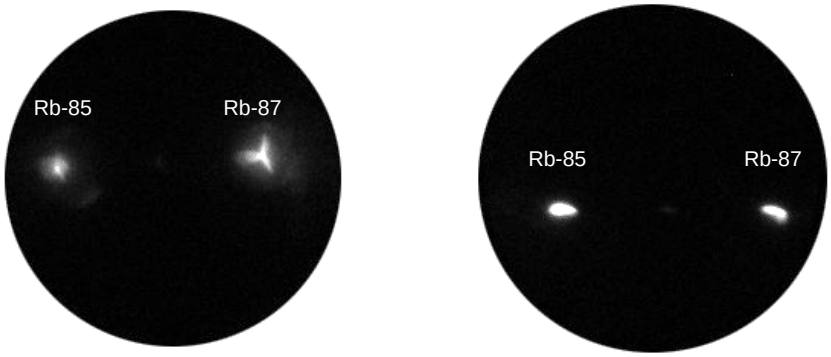


**Figure 4.18:** Pictures of $^{85,87}$Rb ion beams monitored with the combined MCP/phosphor screen behind the separator magnet. It is a useful tool for the beam tuning procedure, because the size and the shape of the ion beam can be directly visualized. The focus settings used to record the left picture are worse than the settings used for the right picture, thus the spots appear more confined on the right picture.

### 4.4.2 Trapped ions from surface ion source

An important milestone for the commissioning of the surface ion source in particular and the common beamline as a whole was the trapping of stable Rb and Sr isotopes in the Penning traps. This was achieved for the first time during the beamtime Nov2012. It was also tried to capture some radioactive isotopes, but the transport efficiency of the transfer section from the RFQ to the Penning traps, including the PDT, was far too low to get any detectable amount into the traps. The amount of about 25 ions/s, measured at this time behind the RFQ in continuous operation, should be in principle enough for the Penning trap operation, because this corresponds to some hundred ions per bunch, depending on the collection time, if the RFQ is operated in bunching mode. But this would need an overall transfer efficiency of at least a few percent. The optimization on this transfer efficiency is difficult, because no detection units are available between the exit of the RFQ and MCP1, directly in front of the superconducting magnet. An

additional FC/MCP unit will be installed in the future behind the PDT, which should help to find good conditions to slow down the ion bunches, without too large losses and without blowing up the size of the ion cloud too much.

Figure 4.19 shows cooling resonances of stable Rb-85 and Sr-88 ions, captured in the purification trap. A cooling resonance is a plot of the count rate versus the cyclotron frequency using solely the purification trap. This can be used to identify clearly what kind of ions reach the trap, because the resolving power of the buffer gas cooling technique is significantly higher than the resolution of the dipole separator magnet. The full width at half maximum (FWHM) of the cooling resonances is 17.9 Hz for Rb-85 and 14.7 Hz for Sr-88. The narrower the resonance, the better is the separation of the selected species from possible contamination. Usually, a FWHM of less than 20 Hz is a good value. In addition, the time-of-flight distribution of the detected ions can give a hint on possible contamination, but in both spectra no ions with significantly longer or shorter time of flight were detected and no substructure is visible in the peaks. So, it can be confirmed that the peaks detected on the FCs at masses 85 and 88 belong to the natural isotopes of Rb and Sr, which can be successfully captured by TRIGA-TRAP.

A few time-of-flight resonances of Rb-85 were recorded also with the precision trap. A continuous excitation scheme was used, where the excitation time was varied. Figure 4.20 shows four recorded resonances, with excitation times from 100 to 700 ms. Table 10 summarizes some data of the resonances. The width of the resonances and accordingly the error of the determined center frequency shrinks with increasing excitation time as expected from eq. 2.22. During these first measurements with ions from the online ion source it was not possible to switch without interruption from the online beam to carbon cluster ions from the laser ablation ion source. Therefore, it was not possible to record any frequency ratio and only absolute frequencies were determined.

**Table 10:** Resonances of Rb-85 ions from the online surface ion source, recorded with the TOF-ICR technique in the precision trap of TRIGA-TRAP.

| excitation time / ms | number of ions | center frequency / Hz | TOF effect / % |
|---|---|---|---|
| 100 | 433 | 1265780.729(464) | 16.7 |
| 200 | 997 | 1265781.366(216) | 8.0 |
| 400 | 945 | 1265781.084(167) | 9.9 |
| 700 | 2499 | 1265780.823(70) | 6.1 |

During the measurements it was observed that the count rate, and the number of

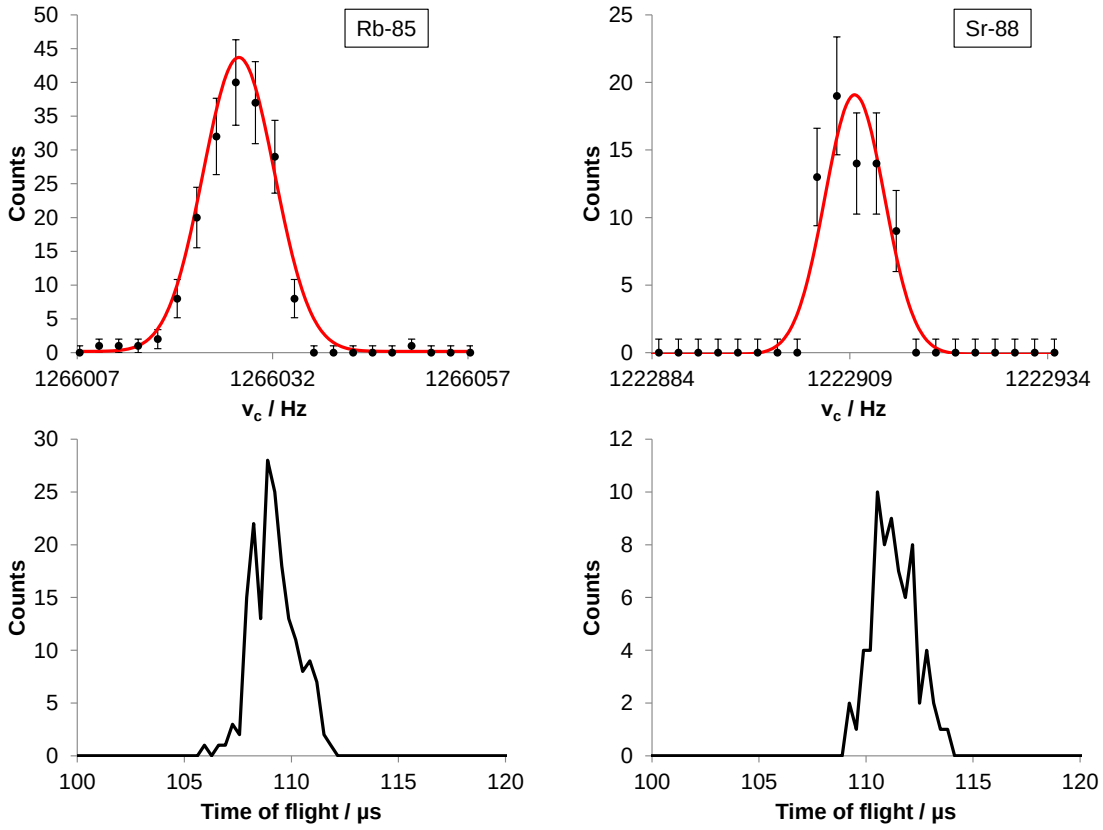


**Figure 4.19:** Cooling resonances of Rb-85 and Sr-88 ions, produced in the online surface ion source. The upper plots show the $\nu_c$ scan in the purification trap. The red line represents a Gauss fit to the data points. The lower plots show the time-of-flight distribution of the detected ions. The cooling resonances have a FWHM of 17.9 Hz and 14.7 Hz and no contamination is visible in the TOF spectra.

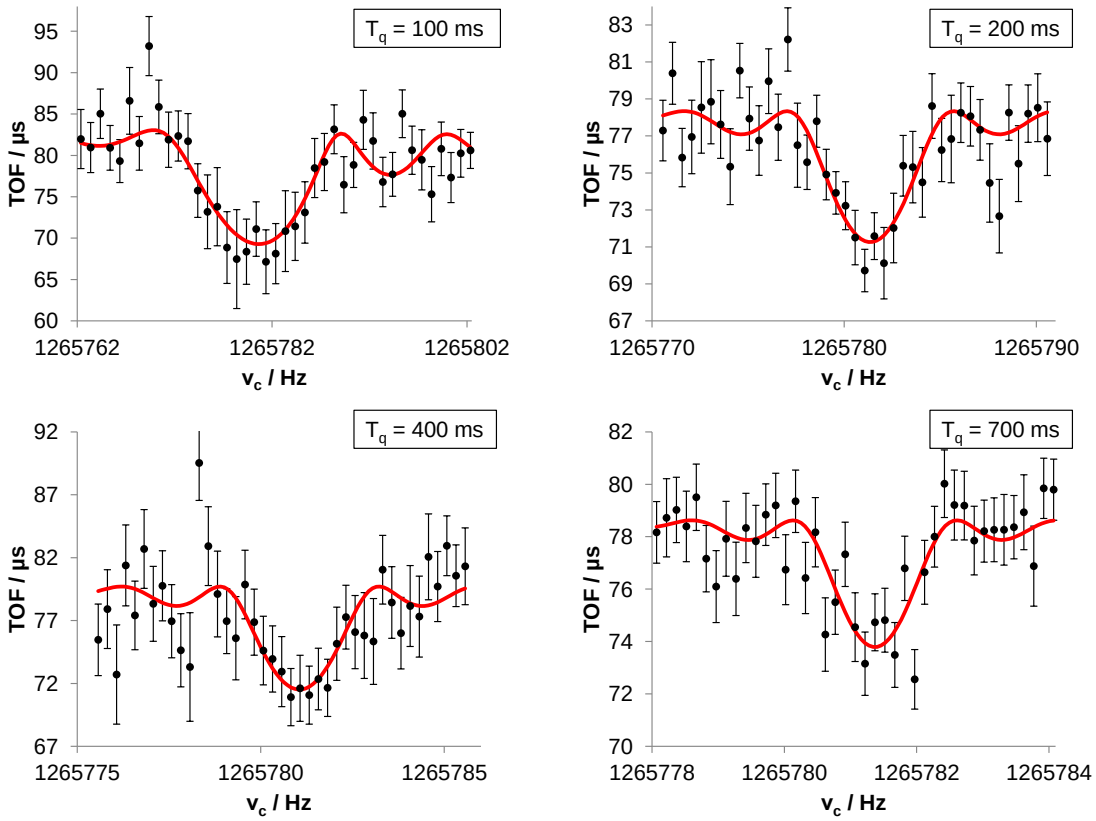


**Figure 4.20:** TOF resonances of Rb-85 from the online ion source, recorded with the precision trap of TRIGA-TRAP. The excitation time $T_q$ was varied from 100 to 700 ms.

ions reaching the traps, drops during the trap operation. Another observation is the fact, that the TOF effect (the percentaged difference between the point with the lowest TOF (excited ions) and the point with the highest TOF (non-excited ions) of the fit) gets significantly smaller with longer excitation times. So, it was not possible to record any resonance with more than 700 ms excitation time. A possible explanation for this behavior was a too high pressure in the transfer and trap section, leading to losses during the ion transport and to a damping force inside the precision trap, decreasing the TOF effect. The reason for the high pressure was the He gas load introduced by the RFQ operation, rendering it even possible to perform the buffer gas cooling technique in the purification trap without flushing buffer gas into the trap. After the beamtime a pumping barrier and an additional turbo pump was installed behind the RFQ structure, to achieve lower pressure in future online operations.

In the beamtime Nov2013 another attempt was undertaken to get some radionuclides to TRIGA-TRAP, but after the negative attempt it was discovered that at least one electrode of the PDT system was not connected properly on the vacuum side. A floating electrode deflected especially the decelerated ions and prevented them from passing the rest of the beamline.

No further attempt to get into the Penning traps with an ion beam coming from the surface ion source has been realized since this beamtime, because most of the time the Penning-trap section was used for offline measurements of transuranium nuclides. But with respect to the improved efficiency and higher absolute ion rates realized during the latest beamtimes, a future attempt looks promising.

# 5 Mass measurements of transuranium nuclides at TRIGA-TRAP

Prior to the current mass measurement campaign, carbon cluster cross-checks were performed to check the operational status of the setup and to evaluate a possible mass-dependent shift of the cyclotron frequency ratio (sec. 5.1). In subsection 5.2 an overview of the status of the mass measurements of all nuclides included in the current measurement campaign is given. The preliminary results will be compared with the data from the AME2012 and from TRIGA-TRAP 2013, if available. The obtained results cannot be finalized, because some inconsistencies were noticed during the evaluation procedure. Subsection 5.3 deals with a systematic analysis of the collected raw data with respect to identifying the source of the observed inconsistencies.

## 5.1 Carbon cluster cross-checks

Frequency ratios between the carbon clusters $^{12}C^{+}_{22,23,24}$ have been measured and compared analog to the procedure of Eibach [17]. The results are listed in tab. 11. The mean frequency ratio $r$ and the deviation $\Delta r$ from the theoretical value are given. In addition, the mass excess $ME$ was calculated, which should yield zero for carbon clusters per definition.

**Table 11:** Carbon cluster measurements for the determination of the systematic shift of the frequency ratio $r$. $\Delta r$ gives the deviation of $r$ from the theoretical value. In addition, the mass excess without ($ME$) and with ($ME_{corr}$) the correction for the systematic shift is given.

| Cluster ion | Reference ion | r | $\Delta r$ / $10^{-9}$ | $ME$ / keV | $ME_{corr}$ / keV |
|---|---|---|---|---|---|
| $^{12}C^{+}_{22}$ | $^{12}C^{+}_{23}$ | 0.9565216498(64) | 3.0(6.4) | 0.8(1.6) | 0.0(1.7) |
| $^{12}C^{+}_{22}$ | $^{12}C^{+}_{24}$ | 0.9166665018(57) | 6.1(5.7) | 1.7(1.5) | 0.1(1.9) |
| $^{12}C^{+}_{23}$ | $^{12}C^{+}_{24}$ | 0.9583332506(37) | 3.4(3.7) | 0.9(1.0) | 0.1(1.1) |

A calculation (weighted mean of $\Delta r$) of the shift of the frequency ratio per mass unit yields

$$r_{shift} = -2.6(1.8) \cdot 10^{-10}/u. \tag{5.1}$$

Applying eq. 5.1 on the measured frequency ratios results in the $ME_{corr}$ values, given in tab. 11. Although the absolute error of the mass excess increases slightly, the shift

brings the values close to zero. Most of the investigated transuranium nuclides were measured alternately against two different carbon clusters, so that the effect of the shift could be also monitored during the individual measurements. This correction is routinely applied in the following evaluations, unless a different approach is mentioned explicitly.

## 5.2 Results of the transuranium mass measurement campaign

All presented mass measurements were measured and evaluated as described in sec. 3.4.4. Table 12 presents an overview of all available nuclides for the current measurement campaign.

**Table 12:** Overview of all available nuclides for the actual mass measurement campaign. The available amount is given as absolute number of atoms. In general, an amount of about $1 \cdot 10^{15}$ is necessary for the target production. Details on the performed or planned mass measurements are given in the corresponding subsections.

| Nuclide | Origin[7] | Amount | Purity | Subsection |
|---|---|---|---|---|
| Am-241 | NCM | $> 10^{17}$ | pure sample | 5.2.1 |
| Cf-249 | LBNL/NCM | $> 10^{17}$ | pure sample | 5.2.2 |
| Cf-250 | ORNL | $1.5 \cdot 10^{16}$ | mixed Cf sample | 5.2.3 |
| Cf-251 | ORNL | $3.9 \cdot 10^{16}$ | mixed Cf sample | 5.2.3 |
| Bk-249 | ORNL | $\approx 2 \cdot 10^{17}$ | mixed with Cf-249 | 5.2.4 |
| Cm-245 | ORNL | $1.7 \cdot ^{16}$ | pure sample | 5.2.5 |
| Cm-246 | ORNL | $1.1 \cdot ^{16}$ | mixed Cm sample | 5.2.6 |
| Cm-248 | ORNL | $7.5 \cdot ^{16}$ | mixed Cm sample | 5.2.7 |
| Cm-248 | NCM | $> 10^{17}$ | pure sample | 5.2.7 |
| Pu-242 | NCM | $> 10^{17}$ | pure sample | 5.2.8 |
| Pu-244 | GSI | $> 10^{17}$ | pure sample | 5.2.9 |

### 5.2.1 Am-241

The two most investigated nuclides in the frame of this work are Am-241 and Cf-249. Both are available in relatively large amounts at the department of nuclear chemistry in Mainz, so that intense studies are possible. In addition to the literature values of

[7]NCM: Department of nuclear chemistry of the Johannes Gutenberg University Mainz. GSI: GSI Helmholtzzentrum für Schwerionenforschung, Darmstadt. ORNL: Oak Ridge National Laboratory, TN, USA.

the AME2012 [16], both nuclides were measured at TRIGA-TRAP in 2013 [24], making them ideal candidates to test the current performance of the Penning-trap setup.

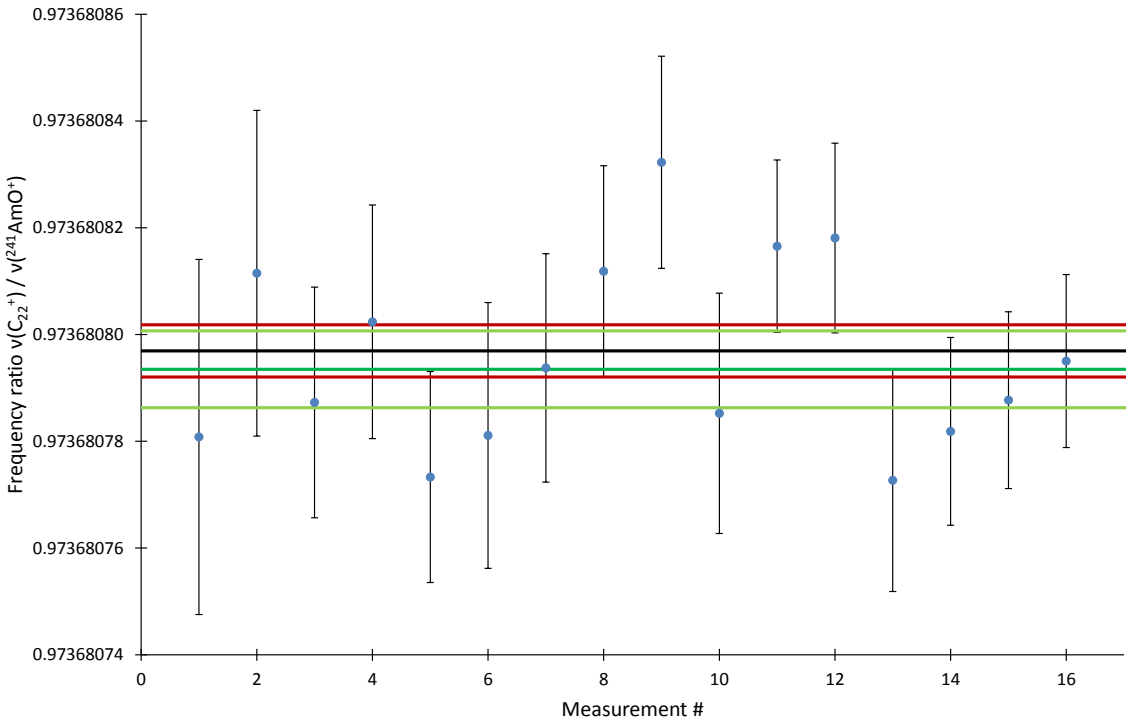


**Figure 5.1:** Recorded frequency ratios of $^{241}AmO^+$ vs. $C_{22}^+$ in June 2015. The error weighted mean ratio is given by the black line, the corresponding $1\sigma$ errors are given in red. The mean AME ratio with the corresponding errors are drawn as green lines in the graph.

The measurement campaign started in June 2015 with a frequency-ratio measurement of $^{241}AmO^+$ vs. $^{12}C_{22}^+$ as reference ion, similar to the TT2013 measurements. In total, 16 frequency ratios, including 11470 detected $^{241}AmO^+$ ion events, were recorded (see fig. 5.1). Another measurement series was performed in November 2015, including 30 frequency ratios with 23344 $^{241}AmO^+$ ion events, to check the reproducibility of the data, after some inconsistency was discovered during the rest of the first measurement campaign.

Table 13 presents a comparison of the measurements of TRIGA-TRAP done in 2015, 2013 and the AME2012 values. While the first value obtained in 2015 is in very good agreement with the TT2013 value as well as with the AME2012, the measurement performed in November shows a significant deviation of more than $2\sigma$ from the former value. After the first measurement, no doubt about the performance of the trap setup existed. But an investigation on possible sources that may disturb the measurements was started, after other investigated nuclides were also not in agreement with the reference values.

In the frame of these investigations, which are discussed in detail in section 5.3, the Am-241 measurement was repeated, which revealed that the former value could not be reproduced.

**Table 13:** Results of the mass measurements for Am-241. For each data set, the measured ion species and the reference ion are given. The resulting mass excess ($ME$) refers to the Am-241 atom. The $\Delta ME$ value is calculated by the difference between the $ME$ value of the AME2012, given in the last line, and the measured $ME$ value by TRIGA-TRAP.

| Data | measured ion | reference ion | $ME$ / keV | $\Delta ME$ / keV |
|---|---|---|---|---|
| TT2015 (Jun) | $^{241}Am^{16}O^{+}$ | $^{12}C_{22}^{+}$ | 52937.4 (1.2) | -1.2 (2.2) |
| TT2015 (Nov) | $^{241}Am^{16}O^{+}$ | $^{12}C_{22}^{+}$ | 52930.4 (0.8) | 5.8 (2.0) |
| TT2015 (Nov) | $^{241}Am^{16}O^{+}$ | $^{12}C_{23}^{+}$ | 52930.1 (1.3) | 6.1 (2.2) |
| TT2013 [24] | $^{241}Am^{16}O^{+}$ | $^{12}C_{22}^{+}$ | 52936.9 (1.8) | -0.7 (2.5) |
| AME2012 | | | 52936.2 (1.8) | |

### 5.2.2 Cf-249

Cf-249 was the second nuclide which was investigated after the first measurement of Am-241. Cf-249 was also measured by TRIGA-TRAP in 2013, so it can also serve as a test species to verify the former data. The frequency-ratio measurement of $^{249}CfO^{+}$ vs. $^{12}C_{22}^{+}$ included 32 frequency ratios with in total 24990 detected $^{249}CfO^{+}$ ions. Table 14 presents the data taken by TRIGA-TRAP in 2015, 2013 and the AME2012 value.

**Table 14:** Results of the mass measurements for Cf-249. For each data set, the measured ion species and the reference ion are given. The resulting mass excess ($ME$) refers to the Cf-249 atom. The $\Delta ME$ value is calculated by the difference between the $ME$ value of the AME2012, given in the last line, and the measured $ME$ value by TRIGA-TRAP.

| Data | measured ion | reference ion | $ME$ / keV | $\Delta ME$ / keV |
|---|---|---|---|---|
| TT2015 (Jun) | $^{249}Cf^{16}O^{+}$ | $^{12}C_{22}^{+}$ | 69724.7 (0.9) | 1.3 (2.4) |
| TT2015 (Jun) | $^{249}Cf^{16}O^{+}$ | $^{12}C_{23}^{+}$ | 69726.3 (1.9) | -0.3 (2.9) |
| TT2015 (Nov) | $^{249}Cf^{16}O^{+}$ | $^{12}C_{22}^{+}$ | 69719.4 (1.0) | 6.7 (2.4) |
| TT2015 (Nov) | $^{249}Cf^{16}O^{+}$ | $^{12}C_{23}^{+}$ | 69718.7 (1.2) | 7.3 (2.5) |
| TT2013 [24] | $^{249}Cf^{16}O^{+}$ | $^{12}C_{22}^{+}$ | 69718.1 (1.3) | 7.9 (2.5) |
| AME2012 | | | 69726.0 (2.2) | |

In the measurement campaign in 2013, the result for Cf-249 was most interesting,

because a significant deviation from the AME literature value was found [24]. The TT2015 (Jun) measurement could not reproduce this mass-excess value, but was in good agreement with the AME2012. $^{12}C_{23}^{+}$ was added as a second reference ion to the measurement cycle, so that another set of 9 frequency ratios, including 6817 ions, has been recorded, which supported the TT2015 measurement. The raw data from 2015 as well as from 2013 were reevaluated a few times with varying conditions like the number of regarded ions or the size of the window for the time-of-flight selection. None of these evaluations disagreed with the first results [24].

As for Am-241, the measurement of Cf-249 was also repeated in November 2015. This time the mass excess showed a deviation from the value obtained in June 2015 and the AME2012, but was close to the TT2013 value. The Cf-249 data revealed this way the same inconsistency as the Am-241 data. But the fact that the shift of the mass excess for the two actinides drove in both cases in the same direction is a hint that a systematic effect is responsible for the inconsistency of the data.

### 5.2.3 Cf-250/Cf-251

A very limited amount of these Cf isotopes is available for TRIGA-TRAP as a mixed sample of Cf-249/250/251[8], so that Cf-250 and Cf-251 cannot be measured independently. Tests with a Cf-249 sample showed that beside the wanted $CfO^{+}$ ions also $CfOH^{+}$ ions are created during the laser ablation process. The production ratio $CfO^{+}$:$CfOH^{+}$ is about 10:1. This will cause problems, because the isobaric species $^{249}CfOH^{+}/^{250}CfO^{+}$ and $^{250}CfOH^{+}/^{251}CfO^{+}$ will be produced simultaneously. The cyclotron frequency difference of these two pairs is 9.5 Hz and 7.0 Hz respectively. The usual width of a cooling resonance in the purification trap is in the range of 15-20 Hz (see fig. 4.19), which is not sufficient to separate the two species. In particular for Cf-250 there is no way to avoid an isobaric contamination during the cyclotron frequency measurement. An alternative to the oxide ion would be a measurement of pure $Cf^{+}$ ions, which are only produced at higher laser intensities than needed for oxide ions, leading to a higher consumption-rate of the available target material. Only a very limited amount of Cf-250 and Cf-251 is available, so the increased consumption of the material is not the preferred way. It was also tried to produce some $CfO_2^{+}$ ions, but no applicable amount was found yet.

Another alternative would be a continuous excitation scheme over a sufficiently broad frequency range, so that the cyclotron frequencies of both isobars can be measured simultaneously. This would lead to a reduced precision, but would still result in the first

[8]Cf-249: 50.55%, Cf-250: 13.44%, Cf-251: 35.98%, Cf-252: 0.025%

direct mass measurement of these two isotopes.

A third possible solution would be the implementation of the PI-ICR detection technique, which would theoretically offer a sufficiently high resolving power to distinguish the two ion species.

Because of the low availability and the problems caused by the mixed sample, no attempt was started yet to measure these nuclides. They will stay in the queue until the systematic error analysis is finished and all other available nuclides have reliably been measured.

### 5.2.4 Bk-249

The available Bk-249 sample is a leftover from experiments at GSI in 2012. Due to the relatively short half-life (compared to the other investigated actinides) of 320 d, a large amount of the daughter Cf-249 was produced meanwhile. The Bk-249 has to be separated from its daughter nuclide prior to the mass measurement, because the cyclotron frequency difference is only about 200 mHz between Bk-249 and Cf-249. Therefore, any present Cf-249 species would also pass the purification trap and would cause an isobaric contamination during the Bk-249 measurement.

The chemical separation of Bk/Cf was done with an ion-exchange resin using $\alpha$-HIB[9] as separating agent. The separation itself took only about one day. The time consuming step, which took a few additional days in the lab, was the removal of the $\alpha$-HIB and the transfer into a dilute nitric acid system. It was expected that the $\alpha$-HIB, an organic compound, would be fragmented under the conditions of the laser ablation ion source of TRIGA-TRAP. These organic fragments could form unexpected compounds with Bk, which would lower the yield of the wanted $BkO^+$ ions. Finally, the purified Bk-249 solution was used for the target production six days after the separation and the first measurements started one day later. Based on the half-life of Bk-249, it was calculated that about 10% of the material should be already decayed again into Cf-249. Although a significant influence on the mass measurement of Bk-249 was expected, 6 frequency ratios, including 6262 $^{249}BkO^+$ ions, were measured vs. $^{12}C_{22}^+$ as reference. The evaluation of these first data points revealed an enormous deviation from the AME2012 value of $\Delta ME$ = 69.4 (31) keV. If the raw data is evaluated under the assumption that Cf-249 was measured, a similar deviation, but with a negative sign is obtained $\Delta ME$ = -55.2 (28) keV. If the measured data is compared with the mean literature value of Bk-249 and Cf-249, only a slight deviation of $\Delta ME$ = -7.0 (37) keV is obtained. This indicates

[9] $\alpha$-hydroxyisobutyric acid

that actually Bk and Cf enters the precision trap in comparable amounts.

The purity of the Bk solution has been monitored during and after the separation process by $\alpha$ spectroscopy. This ensures that the separation worked as expected. The reason for the unexpectedly large amount of Cf-249 in the traps is therefore unknown. A possible explanation is that the evaporation and ionization behavior of Bk and Cf is not absolute identical, so that more Cf than Bk ions are produced in the ion source.

For a future attempt of a Bk-249 measurement it should be tested if a target produced from an $\alpha$-HIB based solution does really cause problems during the laser ablation process. This could be tested for example with a pure Cf-249 sample. If the yield of $CfO^+$ ions is not significantly reduced and also no other compounds create problems, like an isobaric contamination, the time consuming purification step after the Bk separation could be skipped next time. In this case a measurement two or three days after the separation should be possible.

### 5.2.5 Cm-245

A mass measurement of Cm-245 has been performed by recording 25 frequency ratios of $^{245}CmO^+$ vs. $^{12}C_{22}^+$ and 19 frequency ratios of $^{245}CmO^+$ vs. $^{12}C_{21}^+$. Table 15 summarizes the evaluated data. The mass-excess value is in good agreement with the AME2012 data. But with respect to the later identified inconsistent data of Am-241 and Cf-249 the value for Cm-245 should be checked again in the future.

**Table 15:** Results of the mass measurements for Cm-245. For each data set, the measured ion species and the reference ion are given. The resulting mass excess ($ME$) refers to the Cm-245 atom. The $\Delta ME$ value is calculated by the difference between the $ME$ value of the AME2012, given in the last line, and the measured $ME$ value by TRIGA-TRAP.

| Data | measured ion | reference ion | $ME$ / keV | $\Delta ME$ / keV |
|---|---|---|---|---|
| TT2015 | $^{245}Cm^{16}O^+$ | $^{12}C_{22}^+$ | 61004.1 (1.2) | 0.9 (2.4) |
| TT2015 | $^{245}Cm^{16}O^+$ | $^{12}C_{21}^+$ | 61004.2 (1.2) | 0.7 (2.4) |
| AME2012 | | | 61004.9 (2.1) | |

### 5.2.6 Cm-246

Cm-246 was not yet measured at TRIGA-TRAP. Only a small amount of about 4.5 $\mu$g ($1.1 \cdot 10^{16}$ atoms) in a mixed Cm sample[10] is available from ORNL. Analogous to Cf-250

[10] Cm-244: 0.004%, Cm-245: 0.574%, Cm-246: 12.8%, Cm-248: 86.6%

and Cf-251, this rare nuclide will be stored until the measurements of all other nuclides are clarified.

### 5.2.7 Cm-248

A mass measurement of Cm-248 has been performed by recording 18 frequency ratios of $^{248}CmO^+$ vs. $^{12}C_{22}^+$ and 9 frequency ratios of $^{248}CmO^+$ vs. $^{12}C_{23}^+$. Table 16 summarizes the evaluated data. The mass-excess value shows a $2\sigma$ deviation from the AME2012 data. As for Cm-245, this value has to be checked again in the future.

**Table 16:** Results of the mass measurements for Cm-248. For each data set, the measured ion species and the reference ion are given. The resulting mass excess ($ME$) refers to the Cm-248 atom. The $\Delta ME$ value is calculated by the difference between the $ME$ value of the AME2012, given in the last line, and the measured $ME$ value by TRIGA-TRAP.

| Data | measured ion | reference ion | $ME$ / keV | $\Delta ME$ / keV |
|---|---|---|---|---|
| TT2015 | $^{248}Cm^{16}O^+$ | $^{12}C_{22}^+$ | 67381.9 (1.2) | 11.1 (5.1) |
| TT2015 | $^{248}Cm^{16}O^+$ | $^{12}C_{23}^+$ | 67384.0 (1.6) | 9.0 (5.3) |
| AME2012 | | | 67393 (5) | |

### 5.2.8 Pu-242

A mass measurement of Pu-242 has been performed by recording 21 frequency ratios of $^{242}PuO_2^+$ vs. $^{12}C_{22}^+$ and 20 frequency ratios of $^{242}PuO_2^+$ vs. $^{12}C_{23}^+$. Table 17 summarizes the evaluated data. The mass-excess value shows a deviation of $> 1\sigma$ from the AME2012 data. Due to the earlier discussed problems regarding the reproducibility of the data, the Pu-242 value cannot be finalized.

**Table 17:** Results of the mass measurements for Pu-242. For each data set, the measured ion species and the reference ion are given. The resulting mass excess ($ME$) refers to the Pu-242 atom. The $\Delta ME$ value is calculated by the difference between the $ME$ value of the AME2012, given in the last line, and the measured $ME$ value by TRIGA-TRAP.

| Data | measured ion | reference ion | $ME$ / keV | $\Delta ME$ / keV |
|---|---|---|---|---|
| TT2015 | $^{242}Pu^{16}O_2^+$ | $^{12}C_{22}^+$ | 54715.4 (0.9) | 3.2 (2.0) |
| TT2015 | $^{242}Pu^{16}O_2^+$ | $^{12}C_{23}^+$ | 54715.9 (0.8) | 2.7 (2.0) |
| AME2012 | | | 54718.6 (1.8) | |

### 5.2.9 Pu-244

A mass measurement of Pu-244 was performed by recording 11 frequency ratios of $^{244}PuO_2^+$ vs. $^{12}C_{22}^+$ and 15 frequency ratios of $^{244}PuO_2^+$ vs. $^{12}C_{23}^+$. Table 18 summarizes the evaluated data. A significant deviation of $> 2\sigma$ from the AME2012 value was determined for the mass excess. Pu-244 was also measured in the earlier TRIGA-TRAP campaign in 2013. The TT2013 mass-excess value was in good agreement with the AME2012. Although the actual measurement is questionable because of the mentioned inconsistencies, the dimension and direction of the deviation of Pu-244 fits to the shift of the also measured mother nuclide Cm-248. If a systematic shift of the absolute cyclotron frequencies influences the presented measurements, at least the relative mass difference between the linked nuclides is accurate enough to confirm the $\alpha$ decay energy given in the AME2012.

**Table 18:** Results of the mass measurements for Pu-244. For each data set, the measured ion species and the reference ion are given. The resulting mass excess ($ME$) refers to the Pu-244 atom. The $\Delta ME$ value is calculated by the difference between the $ME$ value of the AME2012, given in the last line, and the measured $ME$ value by TRIGA-TRAP.

| Data | measured ion | reference ion | $ME$ / keV | $\Delta ME$ / keV |
|---|---|---|---|---|
| TT2015 | $^{244}Pu^{16}O_2^+$ | $^{12}C_{22}^+$ | 59792.4 (1.3) | 14.6 (5.2) |
| TT2015 | $^{244}Pu^{16}O_2^+$ | $^{12}C_{23}^+$ | 59793.3 (0.9) | 13.7 (5.1) |
| TT2013 | $^{244}Pu^{16}O^+$ | $^{12}C_{22}^+$ | 59806.2 (1.8) | 0.8 (5.3) |
| AME2012 | | | 59807 (5) | |

### 5.2.10 PuO/$PuO_2$ investigations

The presented mass measurements for the two Pu isotopes are based on $PuO_2^+$ ions, because the count rate for this species could be much better controlled than that of $PuO^+$ or $Pu^+$. Although the evaluation of the mass-excess value should not be affected by the selection of $PuO_2^+$, because the mass of oxygen is known with such high precision, it was attempted to reproduce the value of Pu-244 by a measurement based on $PuO^+$ ions. As the TT2015 mass measurement of Pu-244 shows a significant deviation from the former TRIGA-TRAP value (see tab. 18), it was of special interest to confirm the measurement and to exclude a possible effect caused by the selection of another kind of ion species. After increasing the laser power (usually 8 $\mu$J for $^{244}PuO_2^+$, now about 13 $\mu$J for $^{244}PuO^+$), an appropriate spot was found on the target, where a sufficient count rate

of monoxide ions was obtained. The first attempt to record a resonance failed, although all settings were kept unchanged. To confirm the production of $PuO^+$ ions, a cooling resonance was recorded (see fig. 5.2 left). Although the cooling resonance does not look wrong at all (FWHM 20 Hz), the time-of-flight distribution is quite surprising, because two clearly separated peaks are visible (see fig. 5.2 right). The two peaks are separated by about 4 $\mu$s, which should not be possible, if only one ion species is ejected from the purification trap. Even if an isobaric contamination is not removed by the buffer gas cooling, it should not be possible to resolve this in the time-of-flight spectrum.

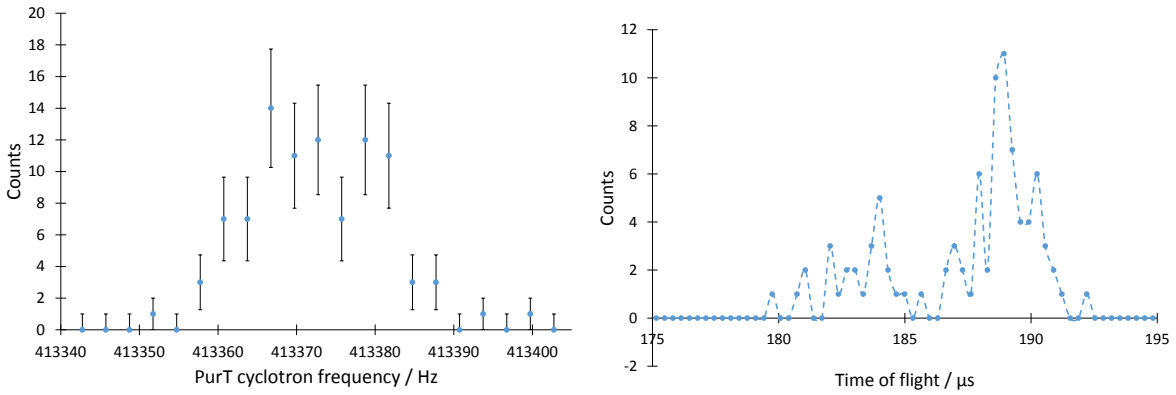


**Figure 5.2:** Left: Cooling resonance of $^{244}PuO^+$. Right: Corresponding time-of-flight distribution. The dashed line is just used for a better visualization.

To exclude a fundamental problem of the purification trap or the TOF section, cooling resonances of the formerly measured species $^{244}PuO_2^+$, $C_{22}^+$ and $C_{23}^+$ were recorded. Figure 5.3 shows the cooling resonance (left) and the TOF distribution (right) of $^{244}PuO_2^+$. Only one single peak at 189.1 $\mu$s is visible in the TOF spectrum, corresponding to the second peak in the TOF spectrum of $PuO^+$ (189.0 $\mu$s; see fig. 5.2 right). The cooling resonances of the carbon clusters looked also fine and only single peaks were detected at a mean TOF of 189.3 $\mu$s for $C_{23}$ and 185.1 $\mu$s for $C_{22}$. So, the first peak in the $PuO^+$ spectrum, at a mean TOF of 183.1 $\mu$s, cannot be explained by any of the other obvious ion species, so it can be assumed that this peak belongs to the demanded $^{244}PuO^+$ ions. In addition, this assumption is strengthened by the calculation of the expected time of flight. For singly charged ions the time of flight $T_{TOF}$ is proportional to the square root of the mass $m$:

$$T_{TOF} \propto \sqrt{m} \tag{5.2}$$

From the identified masses $m = 276$ ($^{244}PuO_2^+$ and $C_{23}^+$) and $m = 264$ ($C_{22}^+$) and their

corresponding time of flight it can be calculated that the time of flight for $m = 260$ ($^{244}PuO^+$) should be about 183.5 $\mu$s.

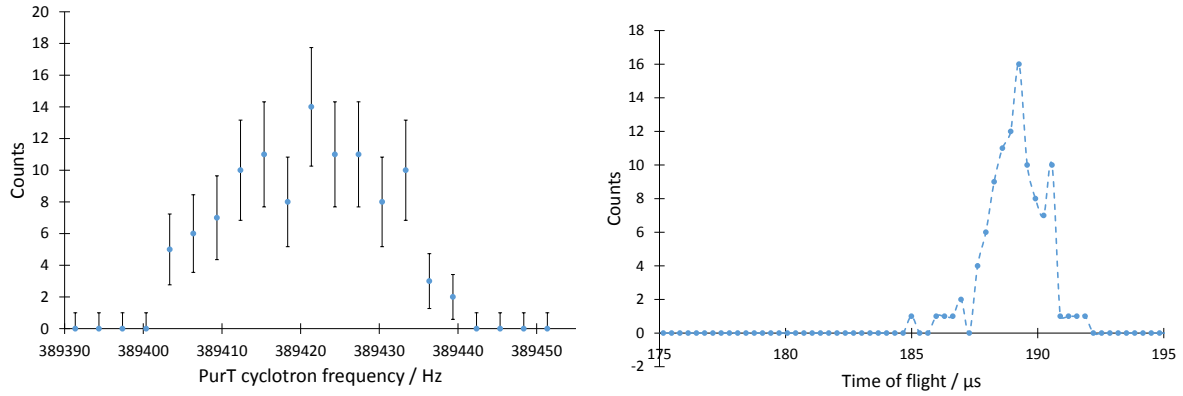


**Figure 5.3:** Left: Cooling resonance of $^{244}PuO_2^+$. Right: Corresponding time-of-flight distribution. The dashed line is just used for a better visualization.

In order to confirm the assumption, that the second peak corresponding to mass 276 in the $^{244}PuO^+$ TOF spectrum belongs to $^{244}PuO_2^+$, it was tried to measure a TOF resonance of $^{244}PuO_2^+$ in the precision trap, while the purification trap was configured for the cooling and centering of $^{244}PuO^+$. The resulting TOF resonance (2 s cont. excitation) is shown in fig. 5.4 and indicates in fact that $^{244}PuO_2^+$ ions enter the precision trap.

Another test to confirm the existence of a contamination inside the precision trap is a dipolar $\nu_+$ cleaning. The modified cyclotron motion of a selected species is increased by a dipolar excitation at the frequency $\nu_+$. By increasing the amplitude of the excitation, at a certain point the radius becomes so large, that the ejected ions cannot reach the detector anymore, so the count rate drops to zero. In contrast to an excitation of the magnetron motion, the $\nu_+$ cleaning is mass dependent, what can be used to clean away the ion of interest, while any possible contamination remains unexcited in the center of the trap. So, in the case that a contaminant is present, the count rate will not drop to zero even at high excitation amplitudes.

Figure 5.5A shows a $\nu_+$ cleaning of $C_{23}^+$. Beyond an amplitude of 0.8 V no ions are detected anymore. Figure 5.5B shows a corresponding excitation of $^{244}PuO^+$, where ions are coming independently of the applied $\nu_+$ amplitude. Figure 5.5C shows the $\nu_+$ amplitude scan for $^{244}PuO_2^+$ ions. The behavior is analog to $C_{23}^+$, as expected. Finally, figure 5.5D shows the $\nu_+$ cleaning for $^{244}PuO_2^+$, while $^{244}PuO^+$ is selected in the purification trap. In this case it is also not possible to get rid of all ions, although the count rate drops to a significant lower level at an amplitude of >0.5 V. This confirms that in the case that $^{244}PuO^+$ is selected in the purification trap, both plutonium oxide species,

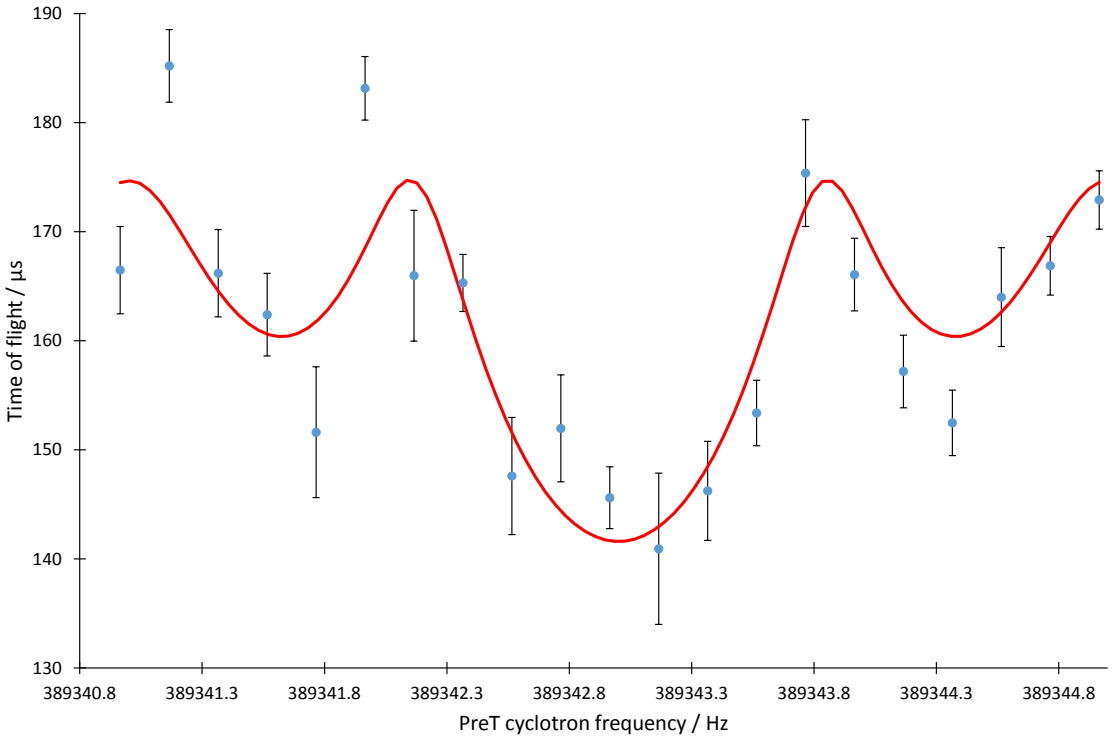


**Figure 5.4:** Time-of-flight resonance of $^{244}PuO_2^+$, recorded with a 2 s continuous excitation scheme in the precision trap, although the purification trap should only eject $^{244}PuO^+$ ions.

the mono- as well as the dioxide, enter the precision trap.

From the count rate ratio in the TOF spectrum (see fig. 5.2 right) it can be seen, that even more dioxide than monoxide is released from the purification trap. A series of investigations was performed to identify the reason for this situation and to find possible parameters that influence the detected ratio of the two species. At first, the cyclotron motion excitation time in the purification trap has been varied from 100 to 1000 ms. The influence on the $PuO/PuO_2$ ratio is plotted in fig. 5.6.

The plot shows that the dioxide becomes the dominant species with longer excitation time. Using a short excitation time of only 100 ms, the monoxide is the primary species that reaches the precision trap. Under these conditions it is at least possible to record a TOF resonance of $^{244}PuO^+$ in the precision trap (see fig. 5.7).

To investigate if this results from the excitation itself or if only the overall storage time inside the trap is important, the second scan focused on a variation of the two waiting times in the purification trap, passive cooling 1 and 2 (see fig. 5.8). The excitation time was kept constant at 200 ms. The waiting time before the excitation, passive cooling 1, does not seem to affect the $PuO/PuO_2$ ratio very strongly, the ratio increases only

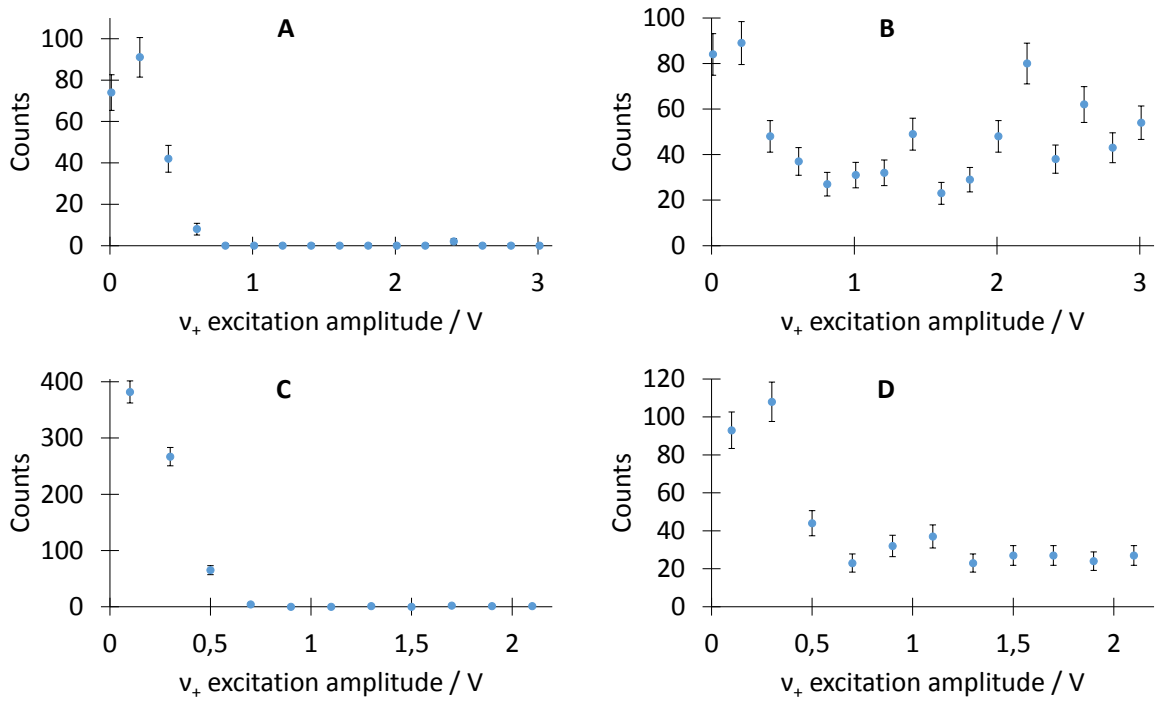


**Figure 5.5:** A: $\nu_+$ cleaning of $C_{23}^+$. B: $\nu_+$ cleaning of $^{244}PuO^+$. C: $\nu_+$ cleaning of $^{244}PuO_2^+$. D: $\nu_+$ cleaning of $^{244}PuO_2^+$, while $^{244}PuO^+$ is selected in the purification trap.

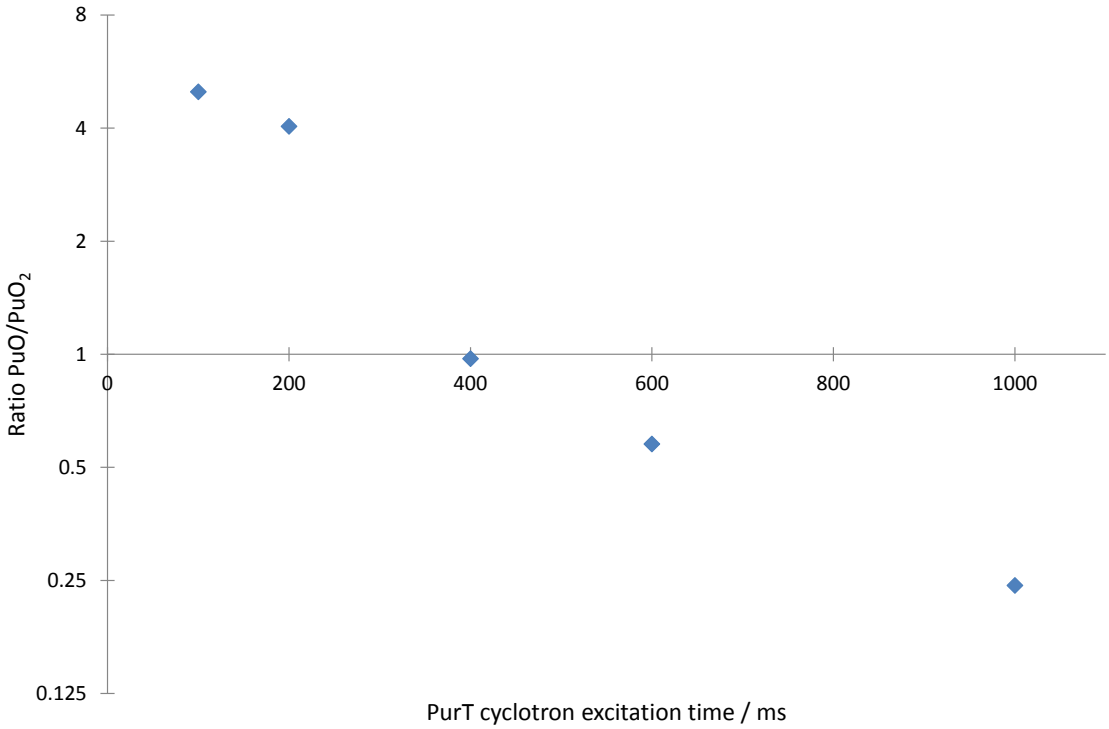


**Figure 5.6:** Variation of the cyclotron excitation time in the purification trap for Pu-244. The $PuO/PuO_2$ ratios were determined from the detected ions in the corresponding TOF spectra.

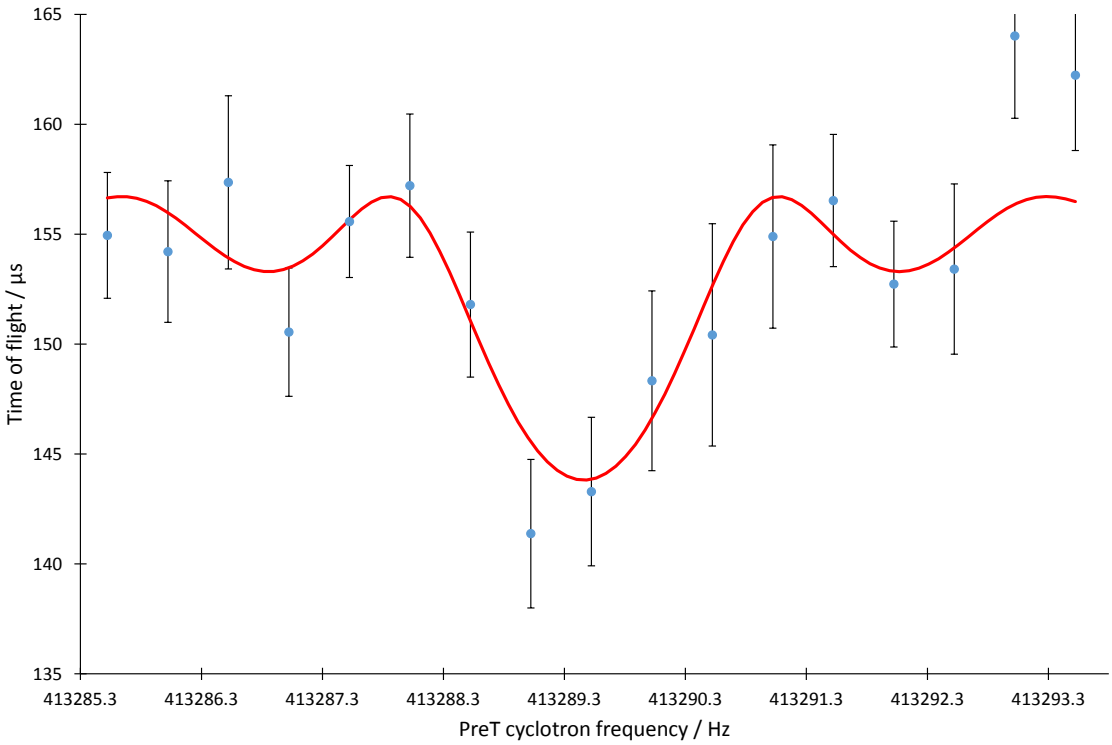


**Figure 5.7:** Time-of-flight resonance of $^{244}PuO^{+}$ (500 ms continuous excitation). The excitation time in the purification trap was reduced to only 100 ms, because under these conditions only a minor amount of $^{244}PuO_2^{+}$ reaches the precision trap.

slightly at longer waiting times. But a longer period for passive cooling 2, the waiting time after the centering of the selected ions, boosts the production of the dioxide species remarkably.

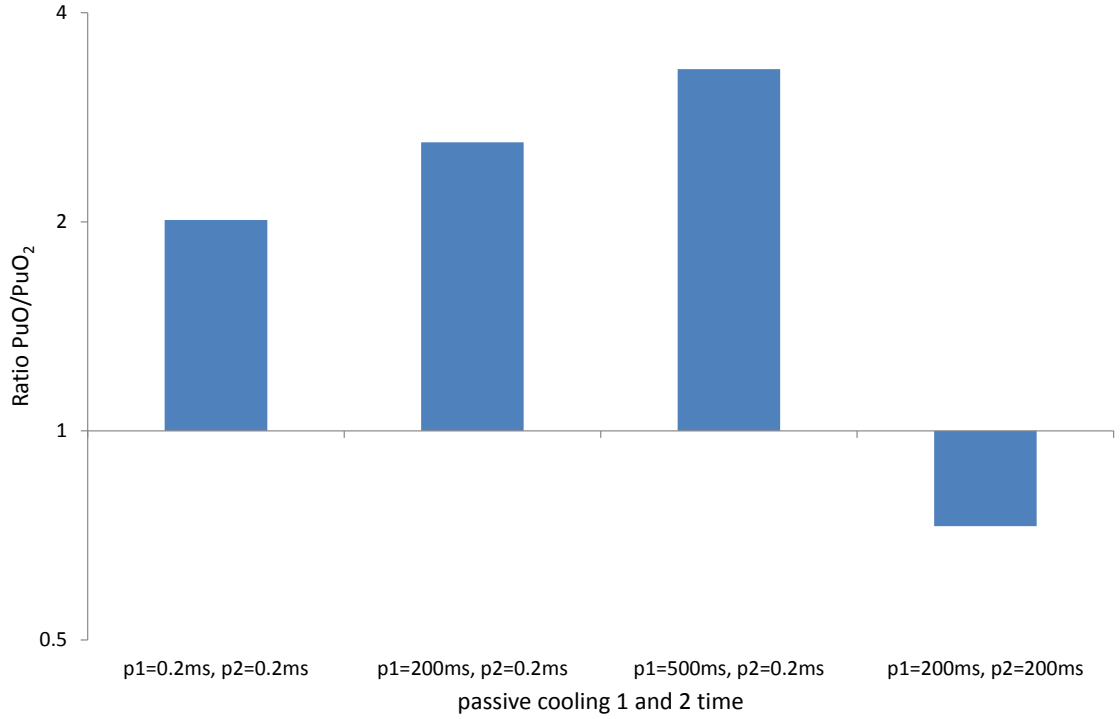


**Figure 5.8:** Variation of passive cooling 1 and 2 in the purification trap for Pu-244. The $PuO/PuO_2$ ratios were determined from the detected ions in the corresponding TOF spectra.

As a last test series the buffer gas flow into the purification trap was changed to investigate the effect on the $PuO/PuO_2$ ratio (see fig. 5.9). The excitation and waiting times in the purification trap were set to maximize the $PuO^+$ signal (excitation time 100 ms, passive cooling 1 200 ms and passive cooling 2 200 $\mu$s). At higher gas flow rates the amount of dioxide ions increases compared to the monoxide.

To sum up the observed effects, it can be noted that conditions that lead to an increased interaction of the captured ions inside the purification trap, either a longer storage time or an increased pressure, lead to the formation of more $^{244}PuO_2^+$. The fact that a change of the initial waiting time, passive cooling 1, does not seem to affect the $PuO/PuO_2$ ratio so strongly is an evidence that the ratio is mainly influenced during or after the cooling and centering procedure.

From a chemical point of view, a disproportion of PuO into Pu and $PuO_2$ would be imaginable, because $PuO_2$ is the most stable oxide species of Pu. After the cooling and centering in the purification trap, the local density of $PuO^+$ ions could be high enough

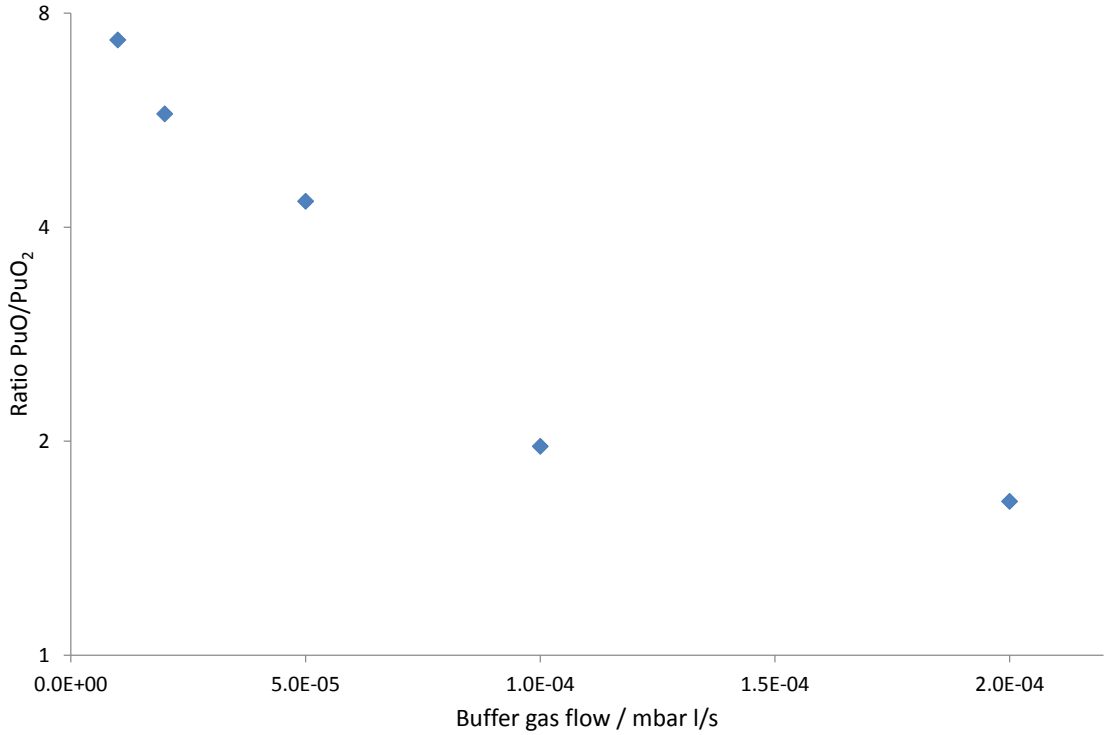


**Figure 5.9:** Variation of the buffer gas flow into the purification trap for Pu-244. The $PuO/PuO_2$ ratios were determined from the detected ions in the corresponding TOF spectra.

to enable such a reaction. In this case the presence of the reduced species, pure $Pu^+$ ions, would be expected, but so far no evidence for another ion species has been found.

## 5.3 Investigations of systematic effects influencing the mass measurements

To identify possible deviations between the evaluated data, a systematic analysis of the fit parameters for the determination of the cyclotron frequency was performed. Figure 5.10 shows a screenshot of the fit window of the evaluation software EVA 6.1.4.0. Beside the center frequency, the magnetron radius "Rho-", the conversion factor "Conv" and an offset value "TofOff" are used as fit parameters for a Ramsey-excitation scheme.

The "TofOff" gives the offset of the fit curve, but does not affect the shape of the curve, so it was not investigated further. But the received values for "Rho-" and "Conv" were plotted for all TOF resonances recorded during the mass measurement campaign. Figure 5.11 and 5.12 show the corresponding plots for "Rho-" and "Conv", sorted by the measured species.

Beside the natural scattering of the fit parameter "Rho-", figure 5.11 reveals also a

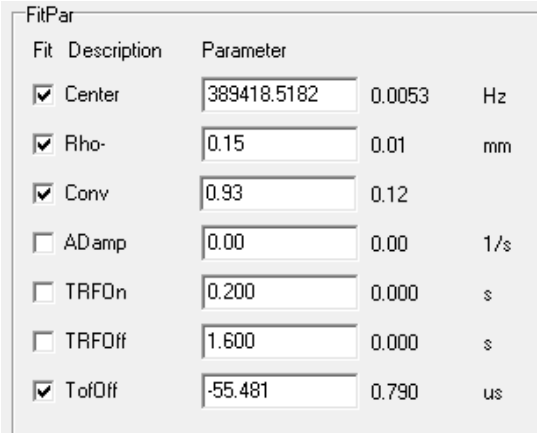


**Figure 5.10:** Fit window of the software EVA 6.1.4.0, used for the evaluations of all time-of-flight resonances.

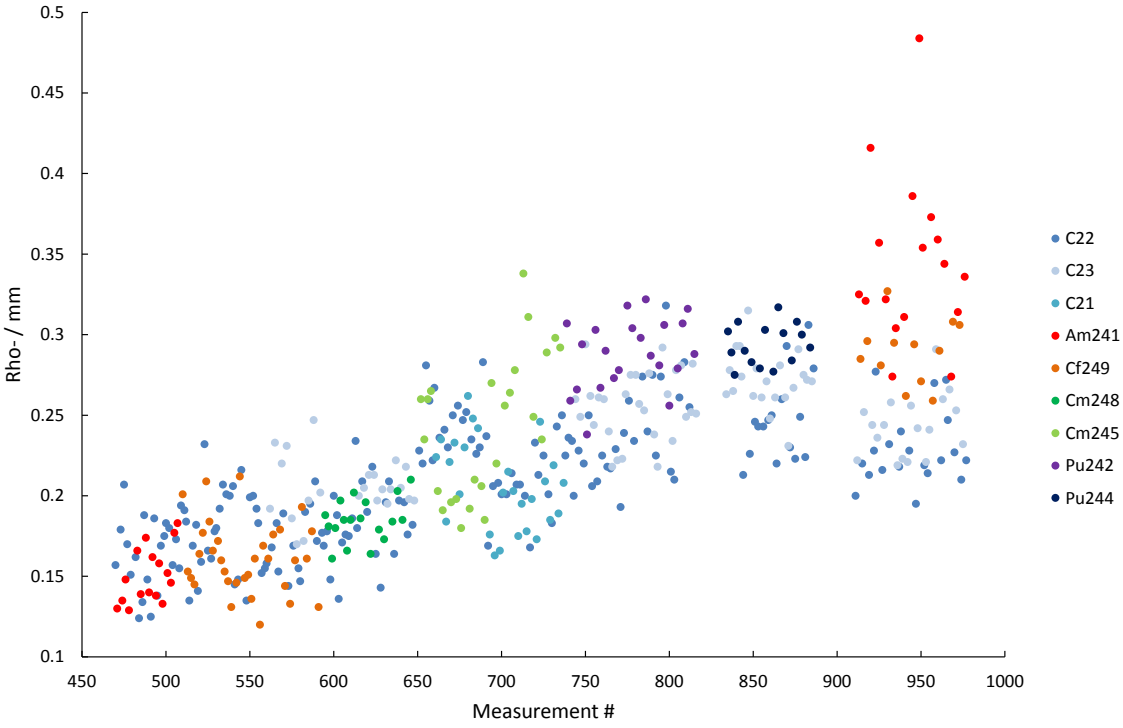


**Figure 5.11:** Plot of the "Rho-" fit parameter received from the evaluation of the TOF resonances of the mass measurement campaign. Error bars are not shown for reasons of clarity.

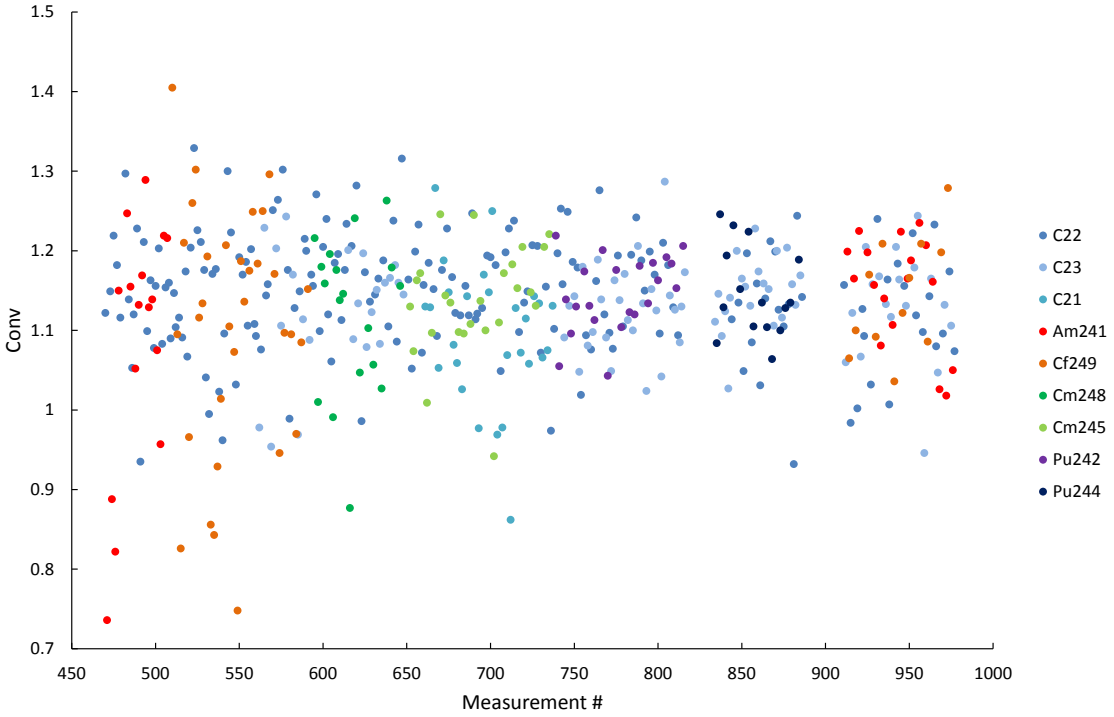


**Figure 5.12:** Plot of the "Conv" fit parameter received from the evaluation of the TOF resonances of the mass measurement campaign. Error bars are not shown for reasons of clarity.

trend to larger radii during the measurement campaign. While the majority of the radii was in the range from 0.12 to 0.20 mm during the first measurements of Am-241 and Cf-249, the radii increased significantly during the later measurements, so that most data points end up in the range between 0.20 to 0.33 mm. Especially the second measurement run on Am-241 in Nov2015 shows extremely large radii of up to 0.48 mm. Although different radii should not cause implicitly a frequency shift, the drift over a long period is at least a hint to a problem, causing non-stable conditions during the measurements. A more detailed investigation of parameters that influence the magnetron radius inside the precision trap will be discussed in the next subsection.

In contrast to the "Rho-" plot, the graph for the "Conv" parameter (fig. 5.12) does not reveal a trend during the observation period. The fit parameter shows a statistical scattering, whereas the majority of the data points are in the range between 1.0 to 1.3. The "Conv" parameter represents the factor for the conversion of the magnetron to the reduced cyclotron motion. A factor of 1 means one total conversion, so that the ions end up with a pure cyclotron motion. The fact that the factor is in average larger than 1 is a hint that the amplitude of the quadrupolar excitation is chosen a bit too high. However, this should not affect the frequency ratio. The excitation amplitude was reduced for the

future measurements from 0.30 V to 0.27 V for a 2 s excitation.

### 5.3.1 Manipulation of magnetron radii inside the precision trap

It should be pointed out that all radii discussed in this section are based on the "Rho-" fit parameter and do not represent directly measured radii.

The first attempt to investigate the reason for the increased magnetron radius was a tuning of the deflectors in front of the traps and an adjustment of the capture timings. This had only minor effects on the radius. In addition it was found that the initial magnetron radius in the precision trap was already large enough to record TOF spectra, even when the magnetron excitation was turned off. This initial magnetron radius in combination with the magnetron excitation resulted in the very large radii during the mass measurements. So, the next step was to investigate the origin of the initial magnetron radius, which would normally be expected to be below the detection limit.

An insufficient cooling in the purification process is a possible cause for a too large initial radius in the second trap. The different cooling parameters, particularly the gas flow, the excitation times and amplitudes and the total storage time in the purification trap were varied and the influence on the initial magnetron radius investigated.

The amplitude of the quadrupolar excitation in the purification trap was varied from 0.2 to 0.6 V, while TOF resonances were recorded in the precision trap, without an additional magnetron excitation. Figure 5.13 shows the influence on the radius (left) in the precision trap and the detected number of ions (right).

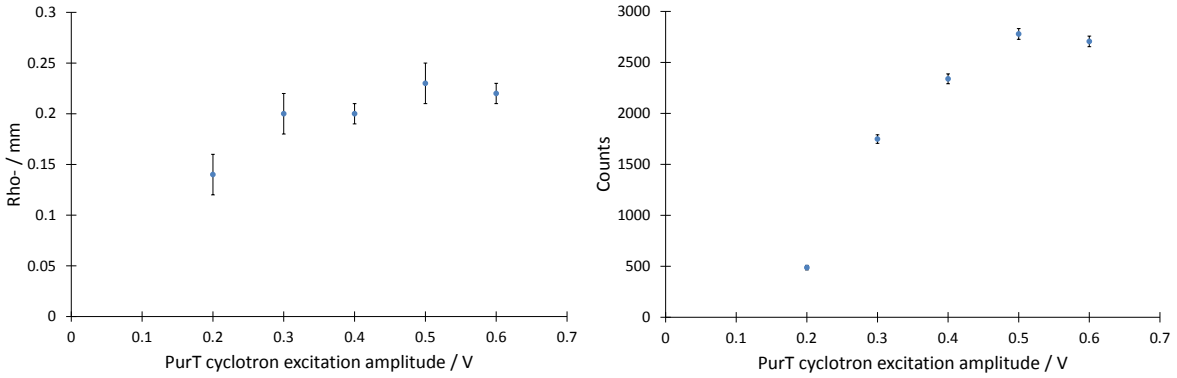


**Figure 5.13:** Influence of the amplitude of the quadrupolar excitation in the purification trap on the magnetron radius of $C_{23}^{+}$ ions inside the precision trap without additional magnetron excitation (left) and on the detected number of ions (right).

The initial radius does not seem to be affected significantly in the range from 0.3 to 0.6 V. Only for the lowest excitation with 0.2 V the radius is a little bit lower,

but more significant is the strong decrease of the detected number of ions at this low excitation amplitude. This can be explained by the insufficient cooling and centering in the purification trap, if the excitation is too weak. This explains also, why it is not possible to record any ions with an even lower excitation amplitude.

The gas flow rate was varied from $1 \cdot 10^{-5}$ to $8 \cdot 10^{-5}$ mbar l/s and the resulting initial magnetron radius was determined (see fig. 5.14 left).

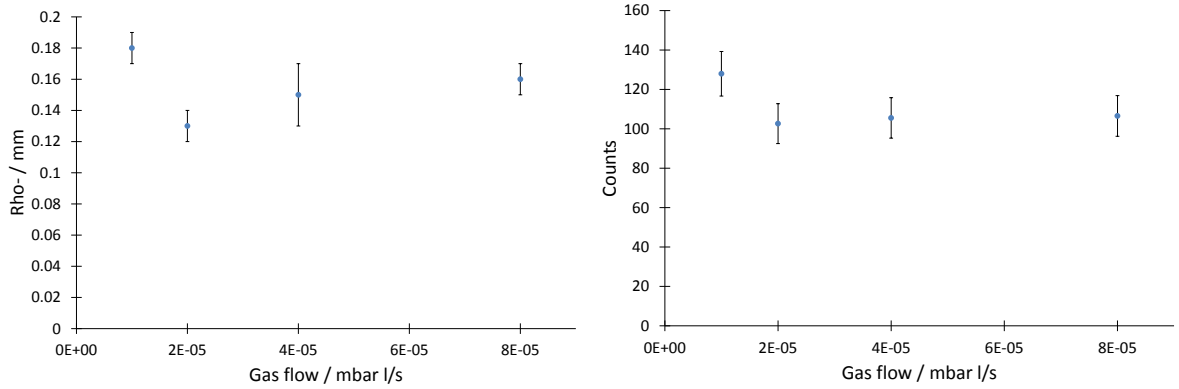


**Figure 5.14:** Influence of the buffer gas flow rate in the purification trap on the magnetron radius of $C_{23}^+$ ions inside the precision trap without additional magnetron excitation (left) and on the detected number of ions (right).

Similar to the former observation of the excitation amplitude, a variation of the buffer gas flow in the purification trap does not lead to a significantly changed magnetron radius in the precision trap. The count rate is also not affected on a remarkable level (see fig. 5.14 right). The fact that neither a stronger excitation nor a higher buffer gas flow influences the initial magnetron radius indicates that not the cooling and centering procedure in the purification trap causes the problem, but that during the transfer to or the capturing in the second trap a certain magnetron motion is induced.

The next settings which were changed are the passive cooling 1 and 2, before and after the active cooling process. During the first tests with these parameters it was found that the count rate as well as the magnetron radius in the precision trap is influenced by these timings. But the effect was only observable, if the magnetron excitation in the precision trap was turned on, while it had no effect on the initial magnetron radius. The periodicity of the effect occurred in the range of a few hundred microseconds. This fits to the period of the magnetron motion, which are given with 854.6 $\mu$s for the purification trap and 315.7 $\mu$s for the precision trap. Some kind of phase dependency of the magnetron excitation from these motions was assumed.

A detailed analysis of the mentioned magnetron phase dependency was undertaken.

The passive cooling 2 timing was used as a delay to vary the phase between the ejection from the purification and all subsequent processes. TOF resonances (2s Ramsey scheme) were recorded with the precision trap, while the delay time was changed, so that the cyclotron frequency $\nu_c$ and the magnetron radius $\rho_-$ could be determined from the fits of the resonances. Figure 5.15 shows the fitted magnetron radius in the precision trap as a function of the delay time.

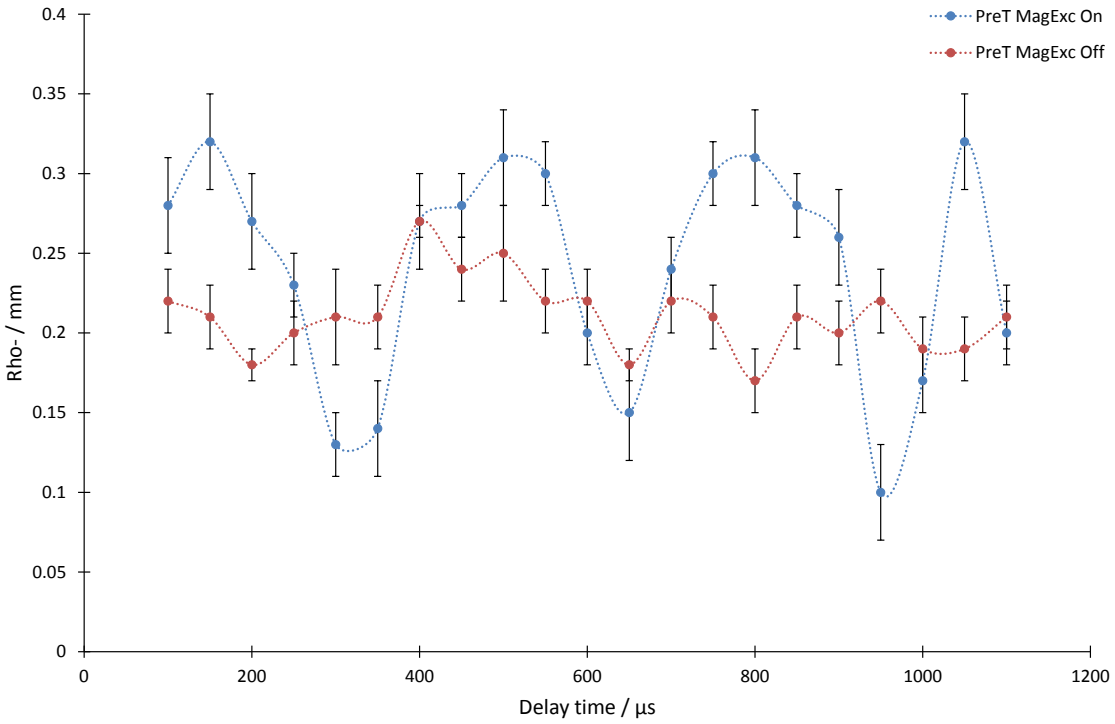


**Figure 5.15:** The magnetron radius of $C_{23}^+$ ions in the precision trap as a function of the delay time in the purification trap. The red data points are recorded without additional magnetron excitation in the PreT, while the blue data points were taken with the usual magnetron excitation (10 ms, 0.5 V). The dashed connection lines are just used for a better visualization of the periodic trend.

Two sets of data points were recorded. The data points presented in red were recorded without an additional magnetron excitation in the precision trap, so the radii correspond to the initial magnetron radii after capturing in the precision trap. The radii show some fluctuation around a mean value of 0.21(2) mm, but no systematic trend is visible in the data. This fact indicates that the phase of the ejection from the purification trap does not influence the initial radius in a measurable dimension.

The blue data points were recorded with the usual magnetron excitation (10 ms, 0.5 V) in the precision trap. This way, the final magnetron radius changes periodically, with three minima at 317.9, 641.2 and 968.2 $\mu$s (determined by Gaussian fits to the data

points). The differences between the minima of about 325 $\mu$s fits well to the period of the magnetron motion in the precision trap. So, the periodic change of the radius is caused by a phase difference of the magnetron excitation.

In order to prove the effect, the radius was recorded as a function of the magnetron excitation amplitude and of the magnetron excitation time (see fig. 5.16). This was done for two different delay times. The usual working point for the mass measurements (10 ms, 0.5 V) is also marked in the graphs.

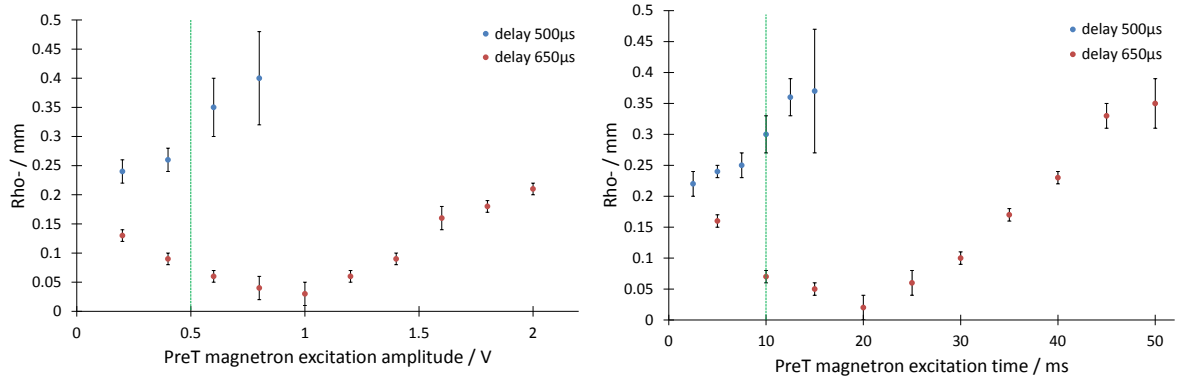


**Figure 5.16:** The magnetron radius of $C_{23}^{+}$ ions as a function of the excitation amplitude (left) and the excitation time (right), recorded for two different delay times. The usual working point (10 ms, 0.5 V) is marked with a green line.

In the case of a delay of 500 $\mu$s, the radius increases with higher excitation amplitude and time. But if the delay is set to 650 $\mu$s, the excitation phase is shifted by half a period and the radius shrinks at the beginning. After it passed zero, the radius increases with higher/longer excitation. The data points in the graph never reaches absolute zero. This is caused by the incapability of the evaluation software to perform a physically meaningful fit to data points with a too small TOF difference, so that no TOF resonance is obtained.

Figure 5.17 shows a plot from the literature [120], which describes the observed behavior of the magnetron excitation. In this case the magnetron radius is plotted versus the excitation time in units of the magnetron period for three phase differences. For a phase difference of $\Delta\phi_{-} = \pi/2$ and $3\pi/2$ the curves show the same trend as the measured data points.

The influence of the different radii on the measured cyclotron frequency can be seen in fig. 5.18 and 5.19. The cyclotron frequency as a function of the delay time fluctuates in both cases, with and without magnetron excitation in the precision trap. But in the case that the excitation is turned on, a certain pattern is observable which fits to the behavior

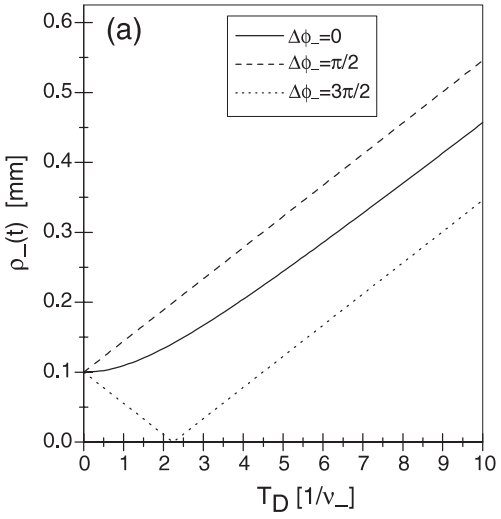


**Figure 5.17:** Dipolar excitation of the magnetron motion in ISOLTRAP's precision trap. The magnetron radius is plotted versus the excitation time (given in units of the magnetron period) for three phase differences [120].

of the measured radii in fig. 5.15. At the delay times where a minimum of the radius is visible, a maximum of the cyclotron frequency is obtained and vice versa. The effect takes place in the range of a few 10 mHz. This can cause shifts in the measured mass excess in the dimension of a few keV, i.e., exactly the order of the deviations encountered during the mass measurement campaign.

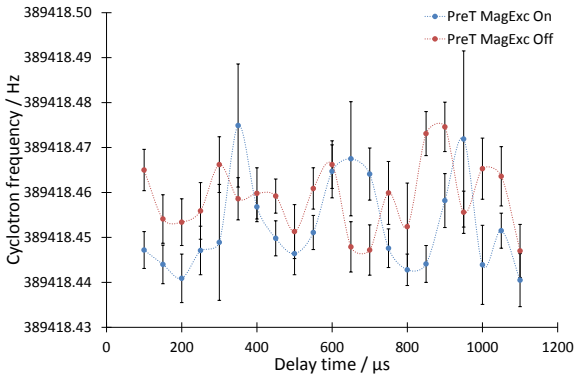


**Figure 5.18:** The cyclotron frequency plotted as a function of the delay time with and without magnetron excitation in the precision trap. The dashed connection lines are just used for a better visualization of the periodic trend.

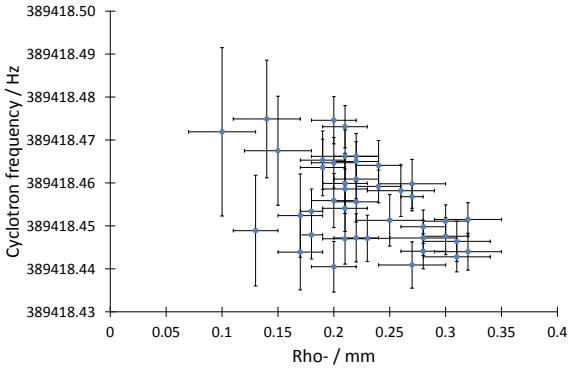


**Figure 5.19:** The cyclotron frequency plotted as a function of the magnetron radius.

In fig. 5.19, the cyclotron frequency is plotted directly as a function of the magnetron radius. In the ideal case, no influence of the radius is expected. But in this representation

one can see that the measured cyclotron frequency tends to smaller values for larger radii.

Another interesting value that has to be discussed is the number of detected ions during the measurements. Figure 5.20 shows the number of ions detected during the delay time measurements. In the case of the deactivated magnetron excitation the count rate is relatively stable, but in the other case the count rate fluctuates very strongly. The periodic pattern of the fluctuation corresponds to the pattern observed for the magnetron radii. At the delay times which lead to the smallest radii, the number of detected ions reaches a maximum.

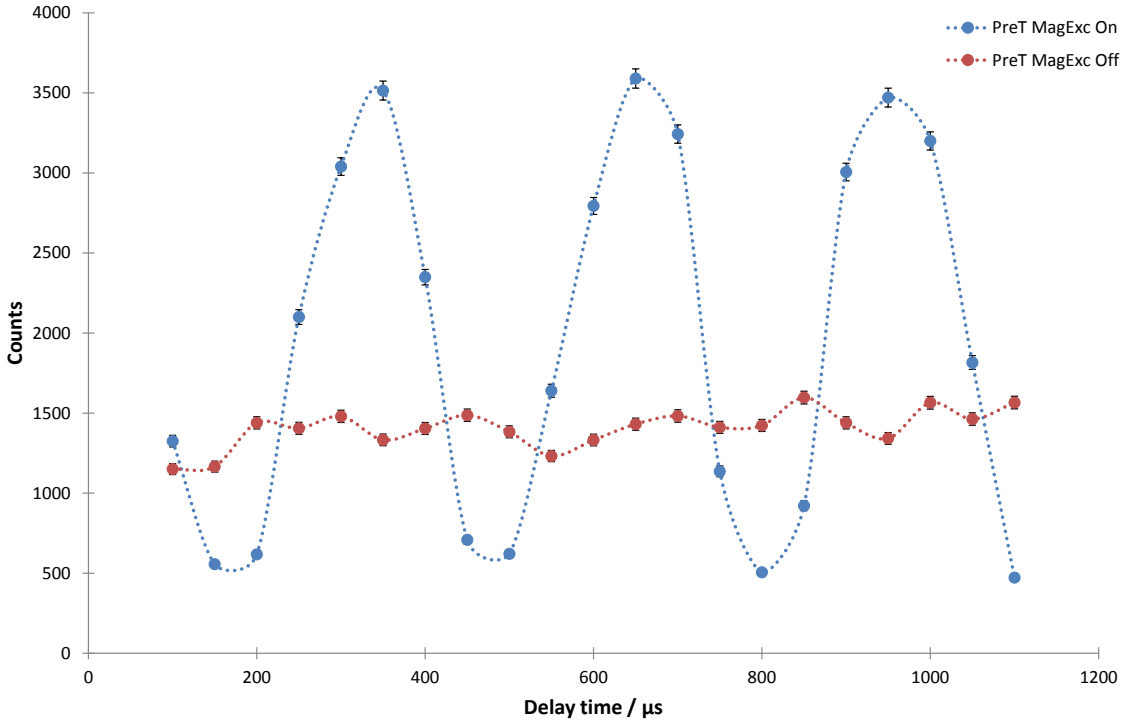


**Figure 5.20:** The number of detected $C_{23}^{+}$ ions as a function of the delay time. The dashed connection lines are just used for a better visualization of the periodic trend.

The settings for the ion production were not changed during the measurement, so it can be assumed that the production rate was relatively stable and the precision trap was loaded all the time with similar amounts of ions. But the number of detected ions is drastically influenced by the radius in the precision trap. The fact that the TOF section does not guarantee a hundred percent transfer efficiency was already known, because of the sometimes observable count rate effect, mentioned in sec. 3.4.3. But the magnitude of this effect was not clear so far. To investigate this further, the count rates yielded during the scans of the magnetron excitation time were plotted versus the magnetron radii (see fig. 5.21).

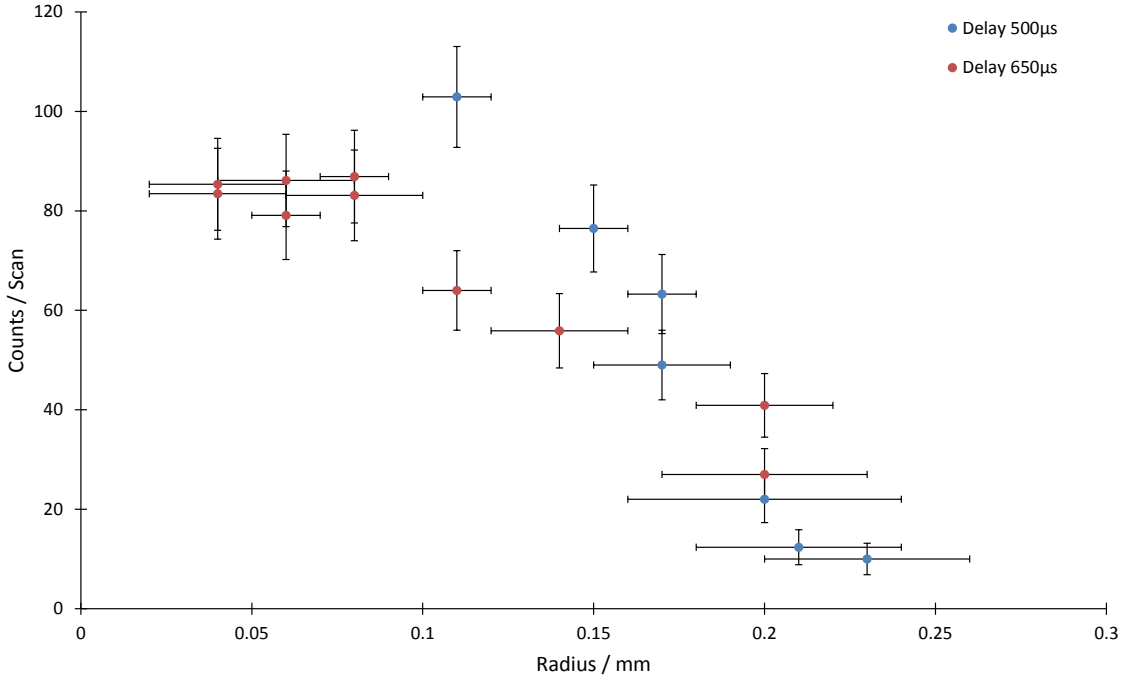


**Figure 5.21:** The number of detected $C_{23}^{+}$ ions as a function of the magnetron radius.

The number of detected ions is only stable up to a radius of about 0.1 mm. With higher radii the count rate drops significantly. At very large radii of >0.25 mm, only a small fraction of about 10-20% is detected compared to the maximum value. So, in the case that large radii are used for cyclotron frequency measurements, as it was the case during some of the actinide mass measurements, a large difference between the detected number of ions and the actual number of ions present in the precision trap has to be assumed. The ions lost in this way will not contribute to the $\nu_c$ determination hence to the mass measurement. An additional problem is that an overload of the precision trap can lead to systematic shifts of the measured cyclotron frequency due to ion-ion interactions [85].

### 5.3.2 z-class analysis

The presented investigations on the effect of the magnetron radius on the cyclotron frequency measurements revealed also a strong dependency from the number of ions present in the precision trap. The usual way to avoid a non-negligible frequency shift caused by ion-ion interactions is to use only events up to ideally one detected ion or extrapolate the frequency corresponding to a single ion in the trap for the evaluation. During the presented mass measurements only events with a maximum of 5 detected

ions per measurement cycle were used. With respect to the large magnetron radii during some of these measurements, it has to be assumed that the real number of ions in the precision trap was several times larger. A possibility to reveal the strength of the effect caused by too many ions at once in the trap is to perform a z-class analysis [85]. This is done by grouping all events in different count rate classes (z-classes), depending on the number of detected ions in the event. A cyclotron frequency determination for each class can reveal a dependency of the frequency from the number of ions. From the slope the cyclotron frequency that fits to a single ion in the trap can be extrapolated (see fig. 5.22)

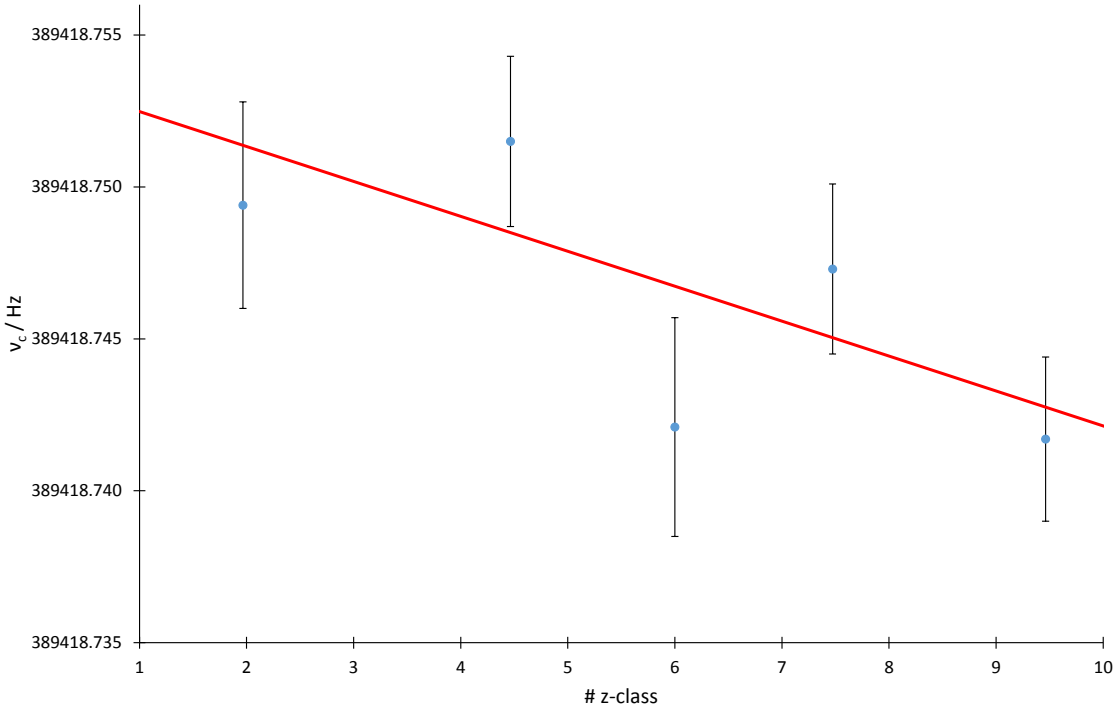


**Figure 5.22:** Cyclotron frequency of $C_{23}^+$ as a function of the z-class. For this graph in total 7586 ions were grouped in 5 different z-classes, containing 1014-1864 ions/z-class. The regarded ion range was set to 1-10 ions. The extrapolation to #Z = 1 (red line) gives the expected cyclotron frequency for a single ion in the trap, if we assume 100% detection efficiency.

A problem of the z-class analysis is the necessity to record large numbers of ion events, to get sufficient statistics for a meaningful evaluation. This is the reason why the z-class analysis is not applied by default during the mass measurements. But four sets of long time measurements of $C_{23}^+$ at two different magnetron radii have been performed to investigate the possible presence of a z-class dependency. Table 19 presents the results of the z-class analysis.

**Table 19:** Results of the z-class analysis for $C_{23}^{+}$ ions at different magnetron radii. For the first and third data set the magnetron excitation was chosen to get $\rho_-$ to about 0.13 mm, for the second and fourth data set it was chosen to achieve $\rho_-$ >0.30 mm. The ion range gives the number of ions per step used for the evaluation. The total number of ions is divided into a certain number of z-classes, which finally yields a corrected value for the cyclotron frequency $\nu_c$(z). The difference between the two cyclotron frequencies is given in the last column.

| $\rho_-$ / mm | $\nu_c$ / Hz | ion range | # ions | z-classes | $\nu_c$(z) / Hz | $\Delta\nu_c$ / Hz |
|---|---|---|---|---|---|---|
| 0.12 (1) | 389418.779 (6) | 1 - 29 (all) | 4885 | 4 | 389418.788 (10) | -0.009 (11) |
| 0.12 (1) | 389418.782 (6) | 1 - 10 | 2425 | 3 | 389418.784 (13) | -0.002 (14) |
| 0.14 (1) | 389418.783 (6) | 1 - 5 | 1160 | 3 | 389418.783 (14) | 0.000 (15) |
| 0.31 (1) | 389418.764 (1) | 1 - 24 (all) | 2524 | 4 | 389418.764 (3) | -0.000 (3) |
| 0.30 (1) | 389418.764 (2) | 1 - 10 | 2137 | 3 | 389418.763 (3) | 0.002 (3) |
| 0.30 (1) | 389418.763 (2) | 1 - 5 | 1448 | 3 | 389418.767 (4) | -0.004 (4) |
| 0.14 (1) | 389418.760 (2) | 1 - 53 (all) | 37227 | 27 | 389418.775 (6) | -0.015 (6) |
| 0.14 (1) | 389418.759 (2) | 1 - 38 | 32510 | 23 | 389418.780 (6) | -0.021 (6) |
| 0.14 (1) | 389418.765 (2) | 1 - 30 | 21694 | 16 | 389418.771 (7) | -0.006 (7) |
| 0.14 (1) | 389418.769 (3) | 1 - 20 | 8245 | 7 | 389418.760 (8) | 0.009 (9) |
| 0.12 (1) | 389418.758 (6) | 1 - 10 | 1929 | 3 | 389418.760 (13) | -0.002 (14) |
| 0.33 (1) | 389418.748 (1) | 1 - 38 (all) | 13677 | 10 | 389418.746 (3) | 0.002 (3) |
| 0.33 (1) | 389418.748 (1) | 1 - 30 | 13610 | 10 | 389418.746 (3) | 0.002 (3) |
| 0.34 (1) | 389418.748 (1) | 1 - 20 | 12610 | 9 | 389418.746 (3) | 0.002 (3) |
| 0.34 (1) | 389418.747 (1) | 1 - 10 | 7586 | 5 | 389418.753 (3) | -0.006 (3) |
| 0.35 (1) | 389418.751 (1) | 1 - 5 | 3020 | 4 | 389418.750 (5) | 0.001 (5) |

For the evaluation different maximum amounts of ions per step were considered and the corresponding number of ions was divided into different numbers of z-classes. The minimum amount of ions per z-class was kept at about 300, because with less ions it is in general not possible to apply a meaningful fit to the data points.

The first two data sets were recorded directly one after another, the last two data sets were recorded a few days later. Due to the magnetic field drift the absolute frequencies of the data sets from different days are not comparable. But also for the data sets that were measured directly in a row, so that the magnetic field drift should not have a significant effect, a cyclotron frequency deviation of about 20-30 mHz is found for the different magnetron radii. This correlates with the former investigations.

More interesting is the difference $\Delta\nu_c$ between the cyclotron frequency obtained directly from the fit of the TOF resonance and the frequency resulting from the z-class analysis. The differences are plotted versus the regarded ion range in fig. 5.23. For most cases, especially for the data points recorded with large magnetron radii, the difference is within the corresponding error ranges. Only in the case of a small magnetron radius and a large selected ion range, a significant deviation of about 20 mHz can be found. This brings the absolute cyclotron frequency from the direct fit close to the value measured for ions on a larger magnetron radius.

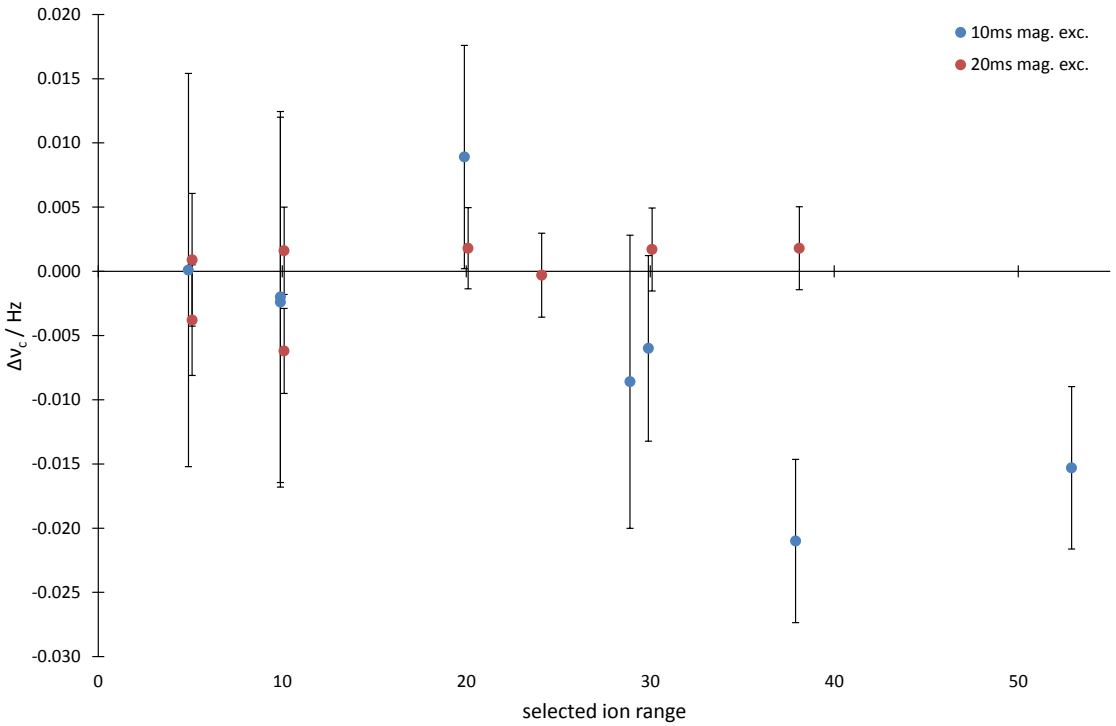


**Figure 5.23:** Cyclotron frequency differences $\Delta\nu_c$ between the direct fit and the z-class analysis as a function of the regarded ion range. The $C_{23}^+$ ions were prepared on two different magnetron radii by different excitation times.

As a conclusion it can be stated that the frequency shift caused by different magnetron radii, and accordingly by different numbers of ions which reach the detector, can also be seen in a z-class analysis, if the ion range is chosen large enough. With count rates of more than 30 detected ions per step, the cyclotron frequency value is similar to the frequency determined with less ions at larger magnetron radii. In the case of large magnetron radii the selected ion range for the evaluation has no significant influence.

### 5.3.3 Two pulse magnetron excitation

The core problem is the presence of the relatively large initial magnetron radius of about 0.2 mm. So far, all attempts to get rid of this by changes of the cooling or capturing settings failed. In the case that the radius is caused by a mechanical offset or a tilt angle between the two traps, an opening of the trap system and a manual realignment is unavoidable in the near future. But with the experiences gained from the magnetron excitation investigations, another idea was tested. According to fig. 5.16 left, a two pulse magnetron excitation scheme was established. The first excitation pulse of 10 ms and 0.8 V brings the magnetron radius to zero. After a waiting time of 300 $\mu$s, about one magnetron period, a second excitation pulse of 0.8 V brings the ions on a defined radius, depending on the length of the second excitation. Figure 5.24 left shows the growth of the magnetron radius as a function of the excitation time of the second pulse. In the range from 5 to 20 ms the growth proceeds linearly. Radii larger than about 0.3 mm were not observed, because of a strongly decreasing count rate, so that not enough ions were detected for a meaningful fit.

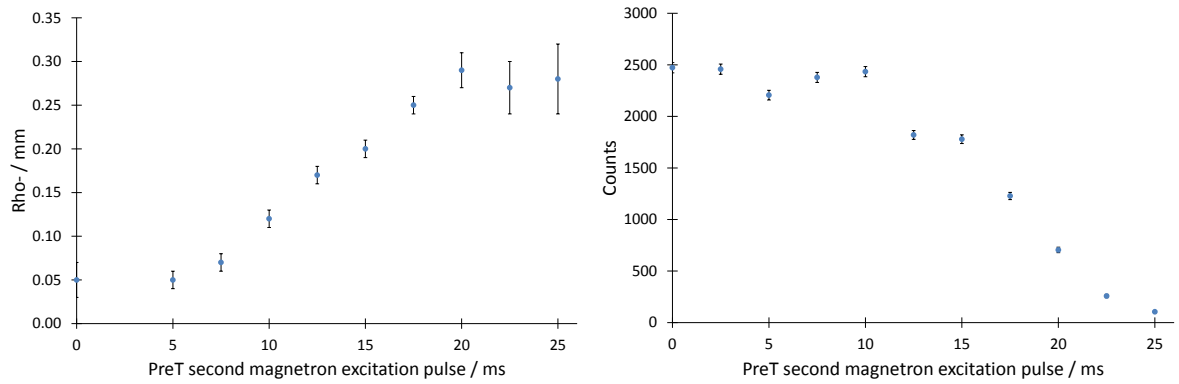


**Figure 5.24:** The magnetron radius (left) and the number of detected $C_{23}^+$ ions (right) as a function of the length of the second magnetron excitation pulse.

The trend of the detected number of ions as a function of the second excitation time is plotted in fig. 5.24 right. With excitation times longer than 10 ms, which corresponds to a radius of $<$0.15 mm, the count rate drops significantly.

The two presented graphs (5.24) were used to determine the optimal duration of the second excitation pulse to be 10 ms. Under these conditions no significant loss of ions is expected. On the other hand, the excitation is strong enough to bring the ions on a radius which is sufficient to generate a noticeable TOF effect. A larger radius leads in general to a larger difference in the time of flight of excited and non-excited ions, creating a larger TOF effect (see fig. 5.25).

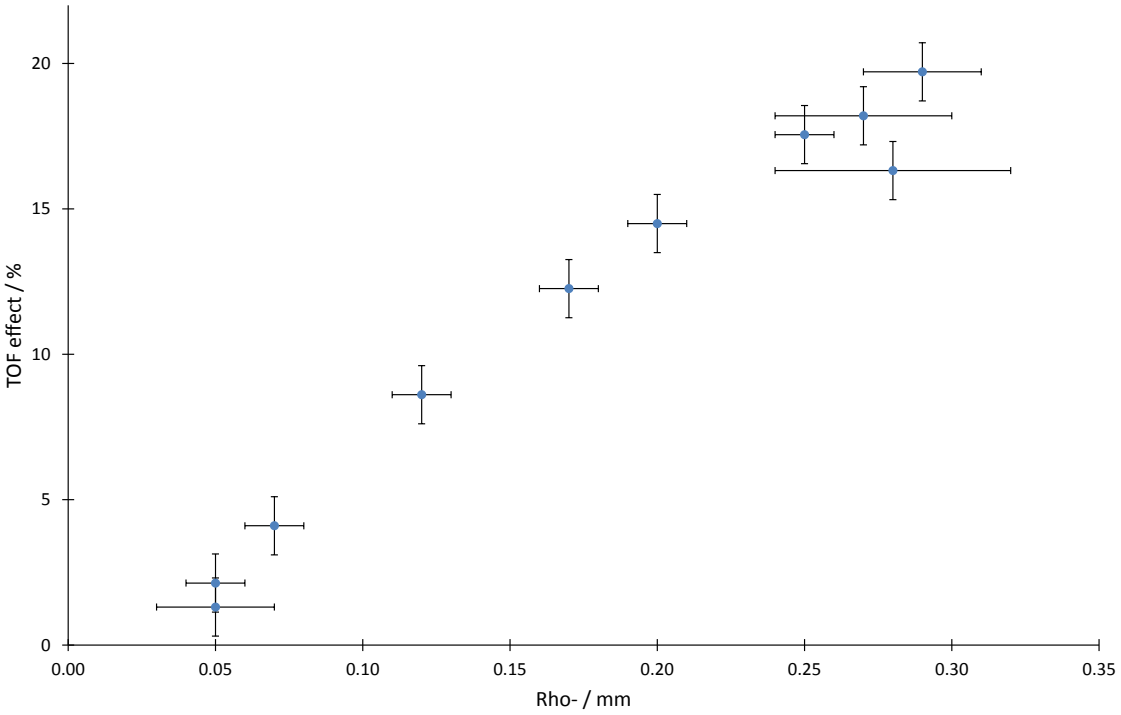


**Figure 5.25:** The TOF effect as a function of the magnetron radius.

Test measurements with the described two-pulse magnetron excitation scheme have been performed with $^{12}C_{22}^{+}$, $^{12}C_{23}^{+}$, $^{241}AmO^{+}$ and $^{249}CfO^{+}$. The mass-excess values for $C_{22}$, Am-241 and Cf-249, presented in tab. 20, show all a certain deviation from the AME2012, with the only exception of $^{249}CfO^{+}$ versus $C_{22}^{+}$ as reference ion. This pair of ions, which has only a mass difference of one amu, results in a $ME$ value for Cf-249 which agrees with the AME2012. For this evaluation the usual mass dependent shift of -2.6(1.8) $\cdot 10^{-10}$ / u has been used (see sec. 5.1). But with respect to the deviation of the carbon cluster cross check ($C_{22}^{+}$ vs. $C_{23}^{+}$), a stronger mass dependent shift of $-1.4(0.2) \cdot 10^{-9}$ / u has been calculated. Applying this shift on the data results in the second data set in tab. 20, whose $ME$ values are all in agreement with the AME2012. The reason for the increased mass dependent shift, which is now about five times larger than before, is not known at the moment. A trap tuning procedure is planned for the near future, using newly developed power supplies for the precision trap, which should offer less noise, a higher accuracy and stability for the trapping voltages than the currently used devices. The dimension of the mass dependent shift will be checked again after this tuning procedure.

**Table 20:** Results of the mass measurements of Am-241 and Cf-249 by applying the two step magnetron excitation scheme. A carbon cluster cross check with $C_{22}^+$ vs. $C_{23}^+$ has been also performed. Applying a stronger mass dependent shift of -1.4(0.2) $\cdot 10^{-9}$ / u on the raw data results in the second data set.

| Data | measured ion | reference ion | $ME$ / keV | $\Delta ME$ / keV |
|---|---|---|---|---|
| $TT_{2step}$ | $^{241}Am^{16}O^+$ | $^{12}C_{23}^+$ | 52929.7 (2.1) | 6.5 (2.8) |
| $TT_{2step}$ | $^{249}Cf^{16}O^+$ | $^{12}C_{22}^+$ | 69723.8 (2.6) | 2.2 (3.4) |
| $TT_{2step}$ | $^{249}Cf^{16}O^+$ | $^{12}C_{23}^+$ | 69720.8 (2.4) | 5.2 (3.2) |
| $TT_{2step}$ | $^{12}C_{22}^+$ | $^{12}C_{23}^+$ | -3.3 (2.3) | |
| $TT_{2step,shift}$ | $^{241}Am^{16}O^+$ | $^{12}C_{23}^+$ | 52934.9 (2.1) | 1.3 (2.8) |
| $TT_{2step,shift}$ | $^{249}Cf^{16}O^+$ | $^{12}C_{22}^+$ | 69723.5 (2.6) | 2.5 (3.4) |
| $TT_{2step,shift}$ | $^{249}Cf^{16}O^+$ | $^{12}C_{23}^+$ | 69723.9 (2.4) | 2.1 (3.2) |
| $TT_{2step,shift}$ | $^{12}C_{22}^+$ | $^{12}C_{23}^+$ | 0.1 (2.3) | |

The control of the magnetron radius in the precision trap is the key to bring the mass measurements back to a reliable level. The presented two-pulse magnetron excitation method could be a solution. But nevertheless the more fundamental problem is that the radius influences the cyclotron frequency, which should not be the case for a harmonic oscillator. In addition, the ions get a certain initial magnetron radius upon capture in the precision trap, maybe due to a mechanical offset or tilt angle between the Penning traps, and either the TOF section or the trap itself cannot handle ions that are ejected from a too large radius.

# 6 Conclusion & Outlook

The first part of this thesis dealt with the coupling of the TRIGA-SPEC setup to the TRIGA Mainz research reactor. Main part of this work was the assembly, commissioning and characterization of the surface ion source. Additional challenges were the coupling to the rest of the existing beamline and the identification of disturbing sources which lead to significant losses of efficiency. Extensive studies of the gas-jet system were also performed to boost the transport efficiency of the fission products from the reactor to the ion source.

The operation of the ion source mainly fulfilled the requirements, so it was possible to supply the TRIGA-SPEC common beamline with ionized fission products for the first time. An overall transfer efficiency from the reactor to the end of the common beamline of at least a few percent was finally achieved for the elements which can be easily ionized by surface ionization processes. Although the design of the source revealed a certain lack in long-time reliability, it was an important device to identify, to test and to optimize multiple crucial elements along the beamline, like the extraction electrode or the best operational conditions for the RFQ cooler/buncher. This resulted finally in the first successful attempt to capture ions, originating in the online ion source, in the Penning-trap setup of TRIGA-TRAP as well as the characterization of the RFQ by using the collinear laser spectroscopy setup of TRIGA-LASER with ionized Ca isotopes. An insufficient transport efficiency for the final stage of TRIGA-TRAP prevented up to now the capture and measurement of radionuclides from the reactor. With the meanwhile boosted output, caused by the larger U-235 target and the new aerodynamic lens system, a future attempt to capture some fission products, most probably Rb or Sr isotopes, in the Penning traps is promising or should at least open the opportunity to identify the last efficiency-reducing elements at the pulsed drift tube and the subsequent beamline.

Future plans regarding the TRIGA-SPEC beamline include a complete redesign of the ion optics. A new cooperation with JAEA[11] introduces also the opportunity to build an advanced online ion source, which is also based on the principle of heating the ionizer by electron bombardment to high temperatures, so that surface ionization processes can occur. Plans to design an ion source based on another ionization principle, like a plasma ion source or a resonant laser ion source, are delayed at the moment. But the possibility to ionize also refractory elements would be a great benefit from such kind of ion source, because it would enlarge the pool of scientifically interesting nuclides which could be

[11] Japan Atomic Energy Agency, Tokai, Japan

investigated at TRIGA-SPEC.

Another crucial point for the future should be the installation of additional beam diagnostic elements along the beamline, especially for the online detection of radionuclides. The actual procedure of catching the radionuclides for $\gamma$-measurements is much too time consuming and has to be improved. In the end, the functionality of all devices along the common beamline has to be ensured without interruption during an online measurement campaign. One possibility would be the installation of a tape station, where radionuclides can be routinely collected and transferred fast to a $\gamma$-detector. A possible position would be the third port of the switchyard, which is currently not in use.

The second part of this thesis focused on the mass measurements of several actinides with the Penning-trap mass spectrometer TRIGA-TRAP. These measurements should continue the measurement campaign of TRIGA-TRAP from 2013. This would provide directly determined mass data of multiple long-lived transuranium nuclides in the vicinity of the deformed shell closure at $N = 152$. During the evaluation of these measurements a fundamental systematic error was found in the measurement procedure of TRIGA-TRAP, leading to non-reliable and inconsistent data. The problem could be located in an insufficient control of the magnetron radius of the ions in the precision trap. The number of detected ions and the measured cyclotron frequency depends on the radius from which the ions are ejected in the precision trap. In addition, a certain initial radius seems to be unavoidable at the moment. Although this can be treated by a new magnetron excitation scheme, using two separate excitation pulses, this solution only fights the symptom of a more fundamental problem, probably caused by a non-harmonic potential or a mechanical offset or tilt angle between the two Penning traps.

A realignment of the traps and a redesign of the TOF section should be considered in the future, especially with respect to the planned PI-ICR upgrade of the detection method. A first step is an intense study of the existing TOF section with the help of ion motion simulations.

For the near future the performance of TRIGA-TRAP will be checked furthermore with reference cross-checks, additional trap tunings and test measurements of well-known nuclides. As soon as the reliability of the setup is ensured again, the measurement campaign of the presented actinides will be repeated and continued.

# 7 References


[1] D. Lunney, J. Pearson, and C. Thibailt, Rev. Mod. Phys. **75**, 1021 (2003).

[2] K. Blaum, Phys. Rep. **425**, 1 (2006).

[3] C. Weizsäcker, Zeitschrift für Physik **96**, 431 (1935).

[4] E. Anders and M. Ebihara, Geochimica et Cosmochimica Acta **46**, 2363 (1982).

[5] K. Blaum and H. Schatz, Physik Journal **5** (2006).

[6] E. Burbidge, G. Burbidge, W. Fowler, and F. Hoyle, Reviews of Modern Physics **29** (1957).

[7] P. Seeger, W. Fowler, and D. Clayton, Astrophysical Journal Supplement **11** (1964).

[8] C. Iliadis, *Nuclear Physics of Stars* (WILEY-VCH Verlag GmbH & Co. KGaA, Weinheim, 2007).

[9] F.-K. Thielemann, A. Arcones, R. Käppeli, M. Liebendörfer, T. Rauscher, C. Winteler, C. Fröhlich, I. Dillmann, T. Fischer, G. Martinez-Pinedo, et al., Progress in Particle and Nuclear Physics **66**, 346 (2011).

[10] I. Panov, E. Kolbe, B. Pfeiffer, T. Rauscher, K.-L. Kratz, and F.-K. Thielemann, Nuclear Physics A **747**, 633 (2005).

[11] I. Dillmann and Y. Litvinov, Progress in Particle and Nuclear Physics **66**, 358 (2011).

[12] K. Blaum, J. Dilling, and W. Nörtershäuser, Phys. Scr. **T152**, 014017 (2013).

[13] K. Langanke and H. Schatz, Phys. Scr. **152**, 014011 (2013).

[14] FAIR, Green Paper (2009).

[15] T. England and B. Rider, Los Alamos National Laboratory (1994).

[16] M. Wang, G. Audi, A. Wapstra, F. Kondev, M. MacCormick, X. Xu, and B. Pfeiffer, Chinese Physics C **36**, 1603 (2012).

[17] M. Eibach, Ph.D. thesis, Ruprecht-Karls-Universität Heidelberg (2013).

[18] M. Goeppert-Mayer, Phys. Rev. **74**, 235 (1948).

[19] M. Goeppert-Mayer, Phys. Rev. **75**, 1969 (1949).

[20] M. Block, D. Ackermann, K. Blaum, C. Droese, M. Dworschak, S. Eliseev, T. Fleckenstein, E. Haettner, F. Herfurth, F. P. Heßberger, et al., Nature **463**, 785 (2010).

[21] E. Minaya, D. Ackermann, K. Blaum, M. Block, C. Droese, C. Düllmann, M. Dworschak, M. Eibach, S. Eliseev, E. Haettner, et al., Science **337**, 1207 (2012).

[22] J. Dvorak, W. Brüchle, M. Chelnokov, R. Dressler, C. Düllmann, K. Eberhardt, V. Gorshkov, E. Jäger, R. Krücken, A. Kuznetsov, et al., PRL **97**, 242501 (2006).

[23] M. Block, International Journal of Mass Spectrometry **349-350**, 94 (2013).

[24] M. Eibach, T. Beyer, K. Blaum, M. Block, C. Düllmann, K. Eberhardt, J. Grund, S. Nagy, H. Nitsche, W. Nörtershäuser, et al., Physical Review C **89**, 064318 (2014).

[25] J. Ketelaer, J. Krämer, D. Beck, K. Blaum, M. Block, K. Eberhardt, G. Eitel, R. Ferrer, C. Geppert, S. George, et al., NIM A **594**, 162 (2008).

[26] S. Kaufmann, T. Beyer, K. Blaum, M. Block, C. Düllmann, K. Eberhardt, M. Eibach, C. Geppert, C. Gorges, J. Grund, et al., Journal of Physics: Conference Series **599**, 012033 (2015).

[27] D. Aumann, Angewandte Chemie **87**, 77 (1975).

[28] W. Demtröder, *Experimentalphysik, Band 4: Kern-, Teilchen- und Astrophysik* (Springer, Heidelberg, 1998).

[29] J. de Laeter, J. Böhlke, P. de Bievre, H. Hidaka, H. Peiser, K. Rosman, and P. Taylor, Pure Appl. Chem. **75**, 683 (2003).

[30] V. Viola, K. Kwiatkowski, and M. Walker, Physical Review C **31**, 1550 (1985).

[31] H. Schmitt, J. Neiler, and F. Walter, Physical Review **141**, 1146 (1966).

[32] R. Kirchner, Nuclear Instruments and Methods **186**, 275 (1981).

[33] U. Köster, Eur. Phys. J. A **15**, 255 (2002).

[34] R. Kirchner, NIM B **204**, 179 (2003).

[35] B. Jonson and A. Richter, Hyperfine Interactions **129**, 1 (2000).

[36] P. Dendooven, Nuclear Instruments and Methods in Physics Research B **126**, 182 (1997).

[37] J. Äystoe, Nuclear Physics A **693**, 477 (2001).

[38] P. Hoff, L. Jacobsson, B. Johansson, P. Aagaard, G. Rudstam, and H.-U. Zwicky, Nuclear Instruments and Methods **172**, 413 (1980).

[39] U. Köster, O. Arndt, R. Catherall, J. Correia, B. Crepieux, R. Eichler, P. Fernier, L. Fraile, S. Hennrich, K. Johnston, et al., Eur. Phys. J. Special Topics **150**, 293 (2007).

[40] R. MacFarlane, R. Gough, N. Oakey, and D. Torgerson, Nuclear Instruments and Methods **73**, 285 (1969).

[41] W. Bowman, T. Sugihara, and R. MacFarlane, Nuclear Instruments and Methods **103**, 61 (1972).

[42] W.-D. Schmidt-Ott, R. Mlekodaj, E. Spejewski, and H. Carter, Nuclear Instruments and Methods **124**, 83 (1975).

[43] W. Talbert, M. Bunker, and J. Starner, NIM B **26**, 345 (1987).

[44] K. Wien, Y. Fares, and R. MacFarlane, Nuclear Instruments and Methods **103**, 181 (1972).

[45] A. Mazumdar, H. Wagner, W. Walcher, and T. Lund, Nuclear Instruments and Methods **139**, 319 (1976).

[46] R. Silva, N. Trautmann, M. Zendel, P. Dittner, E. Stender, and H. Ahrens, Nuclear Instruments and Methods **147**, 371 (1977).

[47] J. Zirnheld, L. Schutz, and F. Wohn, Nuclear Instruments and Methods **158**, 409 (1979).

[48] H. Feldstein and S. Amiel, Nuclear Instruments and Methods **113**, 181 (1973).

[49] W. Schmidt-Ott, R. Mlekodaj, and C. Bingham, Nuclear Instruments and Methods **108**, 13 (1973).

[50] R. Anderl, V. Novick, and R. Greenwood, Nuclear Instruments & Methods **186**, 153 (1981).

[51] J. Äystö, V. Rantala, K. Valli, S. Hillebrand, M. Kortelahti, K. Eskola, and T. Raunemaa, Nuclear Instruments and Methods **139**, 325 (1976).

[52] H. Wollnik, Nuclear Instruments and Methods **139**, 311 (1976).

[53] S. Ichikawa, K. Tsukada, M. Asai, H. Haba, M. Sakama, Y. Kojima, M. Shibata, Y. Nagame, Y. Oura, and K. Kawade, NIM B **187**, 548 (2002).

[54] M. Eibach, T. Beyer, K. Blaum, M. Block, K. Eberhardt, F. Herfurth, C. Geppert, J. Ketelaer, J. Ketter, J. Krämer, et al., NIM A **613**, 226 (2010).

[55] T. Sato, M. Asai, N. Sato, K. Tsukada, A. Toyoshima, K. Ooe, S. Miyashita, Y. Kaneya, A. Osa, M. Schädel, et al., J. Radioanal. Nucl. Chem. **303**, 1253 (2014).

[56] F. Zude, Diplomarbeit, Johannes Gutenberg-Universität Mainz (1986).

[57] M. Eibach, Diplomarbeit, Institut für Physik Johannes Gutenberg-Universität Mainz (2009).

[58] P. Kulkarni, P. Baron, and K. Willeke, eds., *Aerosol Measurement* (John Wiley & Sons, 2011), 3rd ed.

[59] J. Grund, Diplomarbeit, Institut für Kernchemie Johannes Gutenberg-Universität Mainz (2014).

[60] M. Brügger, Diplomarbeit, Johannes Gutenberg-Universität Mainz (1979).

[61] A. Mazumdar, H. Wagner, G. Kroemer, W. Walcher, M. Brügger, E. Stender, N. Trautmann, and T. Lund, Nuclear Instruments and Methods **174**, 183 (1980).

[62] A. Mazumdar, H. Wagner, W. Walcher, M. Brügger, and N. Trautmann, Nuclear Instruments and Methods **186**, 131 (1981).

[63] M. Brügger, Ph.D. thesis, Johannes Gutenberg-Universität Mainz (1983).

[64] X. Zhang, K. Smith, D. Worsnop, J. Jimenez, J. Jayne, and C. Kolb, Aerosol Science and Technology **36**, 617 (2002).

[65] X. Zhang, K. Smith, D. Worsnop, J. Jimenez, J. Jayne, C. Kolb, J. Morris, and P. Davidovits, Aerosol Science and Technology **38**, 619 (2004).

[66] P. Liu, P. Ziemann, D. Kittelson, and P. McMurry, Aerosol Science and Technology **22**, 293 (1995).

[67] J. Jayne, D. Leard, X. Zhang, P. Davidovits, K. Smith, C. Kolb, and D. Worsnop, Aerosol Science and Technology **33**, 49 (2000).

[68] B. Wolf, *Handbook of Ion Sources* (CRC Press Inc., 1995).

[69] I. G. Brown, *The Physics and Technology of Ion Sources* (WILEY-VCH, Weinheim, 2004).

[70] I. Langmuir and K. Kingdon, Science **57**, 58 (1923).

[71] I. Langmuir and K. Kingdon, Proc. R. Soc. Lond. A **107**, 61 (1925).

[72] Y. Liu, Y. Kawai, and H. Bilheux, Proceedings of 2005 Particle Accelerator Conference, Knoxville, Tennessee p. 1581 (2005).

[73] S. Datz and E. Taylor, The Journal of Chemical Physics **25**, 389 (1956).

[74] R. C. Weast, ed., *Handbook of Chemistry and Physics* (CRC Press Inc., 1982), 63rd ed.

[75] M. Dresser and D. Hudson, Physical Review **137**, 673 (1965).

[76] A. Latuszynski and V. Raiko, Nuclear Instruments and Methods **125**, 61 (1975).

[77] V. Afanasev, V. Obukhov, and V. Raiko, Nuclear Instruments and Methods **145**, 533 (1977).

[78] R. Kirchner and A. Piotrowski, Nuclear Instruments and Methods **153**, 291 (1978).

[79] R. Kirchner, NIM A **292**, 203 (1990).

[80] T. Sato, M. Asai, A. Borschevsky, T. Stora, N. Sato, Y. Kaneya, K. Tsukada, C. Düllmann, K. Eberhardt, E. Eliav, et al., Nature **520**, 209 (2015).

[81] L. Brown and G. Gabrielse, Rev. Mod. Phys. **58**, 233 (1986).

[82] T. Beyer, Ph.D. thesis, Combined Faculties of the Natural Sciences and Mathematics Ruperto-Carola-University of Heidelberg, Germany (2014).

[83] G. Bollen, R. Moore, G. Savard, and H. Stolzenberg, J. Appl. Phys. **68**, 4355 (1990).

[84] G. Savard, S. Becker, G. Bollen, H.-J. Kluge, R. Moore, T. Otto, L. Schweikhard, H. Stolzenberg, and U. Wiess, Physics Letters A **158**, 247 (1991).

[85] A. Kellerbauer, K. Blaum, G. Bollen, F. Herfurth, H.-J. Kluge, M. Kuckein, E. Sauvan, C. Scheidenberger, and L. Schweikhard, Eur. Phys. J. D **22**, 53 (2003).

[86] J. Vieten, Bachelor's thesis, Technische Universität München (2013).

[87] N. Ramsey, Reviews of Modern Physics **62**, 541 (1990).

[88] M. Kretzschmar, International Journal of Mass Spectrometry **264**, 122 (2007).

[89] S. George, S. Baruah, B. Blank, K. Blaum, M. Breitenfeldt, U. Hager, F. Herfurth, A. Herlert, A. Kellerbauer, H.-J. Kluge, et al., Physicla Review Letters **98**, 162501 (2007).

[90] M. Eibach, T. Beyer, K. Blaum, M. Block, K. Eberhardt, F. Herfurth, J. Ketelaer, S. Nagy, D. Neidherr, W. Nörtershäuser, et al., International Journal of Mass Spectrometry **303**, 27 (2011).

[91] J. Ketelaer, K. Blaum, M. Block, K. Eberhardt, M. Eibach, R. Ferrer, S. George, F. Herfurth, J. Ketter, S. Nagy, et al., Eur. Phys. J. A **42**, 311 (2009).

[92] G. Eitel, M. Block, A. Czasch, M. Dworschak, S. George, O. Jagutzki, J. Ketelaer, J. Ketter, S. Nagy, D. Rodriguez, et al., NIM A **606**, 475 (2009).

[93] S. Eliseev, K. Blaum, M. Block, C. Droese, M. Goncharov, E. Minaya Ramirez, D. Nestrenko, Y. Noviko, and L. Schweikhard, Physical Review Letters **110**, 082501 (2013).

[94] J. J. W. van de Laar, Diplomarbeit, Johannes Gutenberg-Universität Mainz (2015).

[95] P. Anderson, Physical Review Letters **9**, 309 (1962).

[96] G. Bollen, S. Becker, H.-J. Kluge, M. König, R. Moore, T. Otto, H. Raimbault-Hartmann, G. Savard, L. Schweikhard, and H. Stolzenberg, Nuclear Instruments & Methods in Physics Research, Section A: Accelerators, Spectrometers, Detectors, and Associated Equipment **368**, 675 (1996).

[97] K. Blaum, G. Bollen, F. Herfurth, A. Kellerbauer, H.-J. Kluge, M. Kuckein, E. Sauvan, C. Scheidenberger, and L. Schweikhard, Eur. Phys. J. A **15**, 245 (2002).

[98] A. Chaudhuri, M. Block, S. Eliseev, R. Ferrer, F. Herfurth, A. Martin, G. Marx, M. Mukherjee, C. Rauth, L. Schweikhard, et al., Eur. Phys. J. D **45**, 47 (2007).

[99] C. Smorra, K. Blaum, K. Eberhardt, M. Eibach, J. Ketelaer, J. Ketter, K. Knuth, and S. Nagy, Journal of Physics B **42**, 154028 (2009).

[100] J. Ketelaer, T. Beyer, K. Blaum, M. Block, K. Eberhardt, M. Eibach, F. Herfurth, C. Smorra, and S. Nagy, Eur. Phys. J. D **58**, 47 (2010).

[101] C. Smorra, T. Beyer, K. Blaum, M. Block, C. Düllmann, K. Eberhardt, M. Eibach, S. Eliseev, S. Nagy, W. Nörtershäuser, et al., Physical Review C **85**, 027601 (2012).

[102] C. Smorra, T. R. Rodriguez, T. Beyer, K. Blaum, M. Block, C. Düllmann, K. Eberhardt, M. Eibach, S. Eliseev, K. Langanke, et al., Physical Review C **86**, 044604 (2012).

[103] F. Schneider, T. Beyer, K. Blaum, M. Block, S. Chenmarev, H. Dorrer, C. Düllmann, K. Eberhardt, M. Eibach, S. Eliseev, et al., Eur. Phys. J. A **51**, 89 (2015).

[104] K. Eberhardt and A. Kronenberg, Kerntechnik **65**, 269 (2000).

[105] B. Finkle, E. Hoagland, S. Katcoff, and N. Sugarman, Radiochemical Studies: The Fission Products pp. 471 – 477 (1951).

[106] J. Ziegler, J. Biersack, and M. Ziegler, *Stopping and range of ions in matter, 2013.00* (2013).

[107] M. Brügger, N. Hildebrand, T. Karlewski, N. Trautmann, A. Mazumdar, and G. Herrmann, NIM A **234**, 218 (1985).

[108] J. Grund, C. Düllmann, K. Eberhardt, S. Nagy, J. van de Laar, D. Renisch, and F. Schneider, Nucl. Instr. Meth. B **http://dx.doi.org/10.1016/j.nimb.2015.12.017** (2016).

[109] C. Smorra, Ph.D. thesis, Ruprecht-Karls-Universität Heidelberg (2012).

[110] T. Karlewski, Diplomarbeit, Johannes Gutenberg-Universität Mainz (1982).

[111] A. Calverley, Nature **184**, 690 (1959).

[112] D. Manura and D. Dahl, *Simion 8.0.4* (2008).

[113] T. Beyer, K. Blaum, M. Block, C. Düllmann, K. Eberhardt, M. Eibach, N. Frömmgen, C. Geppert, C. Gorges, J. Grund, et al., Appl. Phys. B **114**, 129 (2014).

[114] J. Wiza, Nuclear Instruments and Methods **162**, 587 (1979).

[115] C. Industries, *Genie 2000 v3.2.1* (2009).

[116] D. Renisch, T. Beyer, K. Blaum, M. Block, C. Düllmann, K. Eberhardt, M. Eibach, S. Nagy, D. Neidherr, W. Nörtershäuser, et al., NIM A **676**, 84 (2012).

[117] J. Jeffries, S. Barlow, and G. Dunn, International Journal of Mass Spectrometry and Ion Processes **54**, 169 (1983).

[118] T. Francl, M. Sherman, R. Hunter, M. Locke, W. Bowers, and R. McIver, International Journal of Mass Spectrometry and Ion Processes **54**, 189 (1983).

[119] A. Schäbe, Bachelor's thesis, Mathematisch-Naturwissenschaftliche Fakultät der Rheinischen Friedrich-Wilhelms-Universität Bonn (2012).

[120] K. Blaum, G. Bollen, F. Herfurth, A. Kellerbauer, H.-J. Kluge, M. Kuckein, S. Heinz, P. Schmidt, and L. Schweikhard, J. Phys. B: At. Mol. Opt. Phys. **36**, 921 (2003).